

Tunneling spectroscopy of nanoscale objects: from metallic islands to single atoms and molecules

Thèse présentée par

Benjamin HEINRICH

Pour obtenir le titre de Docteur de l'Université de Strasbourg

21 Juin 2010

Commission d'examen:

Prof. Jean-Pierre Bucher	Directeur de thèse
Prof. Johannes Barth	Rapporteur externe
Prof. José Ignacio Pascual	Rapporteur externe
Prof. Bernard Doudin	Examineur interne
Dr. Laurent Limot	Invité

Institut de Physique et Chimie des Matériaux de Strasbourg



acknowledgment

Finishing this thesis after three and a half years of work and life in Strasbourg brings to my mind the picture of all the people that contributed - directly or indirectly - to the success of this work. Without some of them this work would just not have been possible, others helped to give it additional quality, and some just made Strasbourg a home. I would like to sincerely thank all of them. Thank you very much! Merci beaucoup! Vielen Dank!

Using the opportunity to mention some names in the following, I am fully conscious that this means the omission of many other. I apologize in advance to those not mentioned personally and ask for their charitableness.

During my thesis I was in the comfortable position of having not only one, but a couple of supervisors and my first acknowledgments are for them: First I'd like to sincerely thank Jean-Pierre Bucher, my *directeur de thèse* for giving me the opportunity to work in a fascinating field of research, allowing me great liberty while providing the necessary support at all time. Second I deeply acknowledge the two others: Laurent Limot and Mircea Rastei. While supervising me, they treated me as a colleague, discussing hard, but fair, always trying to understand my *chemistry-poluted* points of view. Thanks Mircea for taking care of my inauguration to the world of STM, for the hours spent together in front of the screen and the calmness you spread. Thanks Laurent for showing how fruitful it can be to challenge the dogmata, to try crazy-looking ideas and, for sure, for carefully reading the manuscript and discussing its weaknesses, not to forget the nights spent together in the lab. And the group would not have been complete without Cristian and Deung-Jang. Thanks to you for the shared work, time and pleasures.

I would like to thank Marc Drillon for accommodating me at the IPCMS and Bernard Doudin for having brought me to Strasbourg. Thanks to Emilie for passing by for the Thursday morning

chat and much more. Merci Nicola for your technical support. Finally I would like to thank all IPCMS members and in particular the people from DMO as well as the PhD students for the nice time I spent in your company, which taught me French day by day.

Après trois années à Strasbourg, j'aimerais remercier de tout cœur mes amies strasbourgeoises, les françaises comme les internationaux: avec vous, Strasbourg est devenu *chez-moi*. Merci les apérologues pour des meilleurs apéros de tous les temps. Un *Merci* chanté pour l'EVUS! Et finalement, *en attendant Godot*, je souhaite une bonne continuation à vous, THE UNPHOTOGRAPHABLES. C'était un merveilleux plaisir de chanter avec vous - Ça va me beaucoup manquer.... kong tse ko kong tse

Schlussendlich danke ich meiner Familie, meinen Eltern, meinen Geschwistern: ohne euch wäre ich nicht, was ich bin und nicht wo ich bin und alles wäre recht sinnfrei. Danke.

Résumé

Quand Richard Feynman tenait en 1959 son fameux discours intitulé "There's plenty of room at the bottom" (français: "Il y a plein d'espace au fond") [1], l'idée d'une électronique des dispositifs nanométriques était née, même si les techniques à cette époque ne permettaient pas la construction, ni l'étude des structures à l'échelle nanométrique. Aujourd'hui, cinquante ans plus tard, l'idée de l'électronique moléculaire, c'est-à-dire des circuits à base des composants moléculaires contrôlés à l'échelle moléculaire est une voie prometteuse pour continuer la miniaturisation des dispositifs électroniques. Par ailleurs, des attentes multiples sont associées à la transition d'une électronique à la base de silicium à une électronique basée sur des matériaux organiques: une fabrication moins coûteuse en énergie et moins toxique, des dispositifs plus durables, plus robustes et des propriétés nouvelles comme la souplesse ou la flexibilité. L'ingénierie moléculaire peut nous offrir des molécules avec des fonctions intrinsèques, tenant le rôle des interrupteurs, des conducteurs ou des amplificateurs. Par contre, dans un grand nombre des cas, les composants organiques doivent être contactés par des conducteurs inorganiques pour permettre la communication et pilotage de l'extérieur. Ce contact organique-inorganique est crucial, parce qu'il peut changer dramatiquement les propriétés de la partie moléculaire. Ainsi, l'étude du contact entre molécules et substrats inorganiques, semi-conducteurs ou métaux, est une des tâches les plus urgentes dans la recherche sur l'électronique moléculaire.

La microscopie et la spectroscopie à effet tunnel (*anglais*: scanning tunneling microscopy and spectroscopy, STM et STS) est un outil unique pour étudier les propriétés physiques en fonction de la structure à l'échelle nanométrique. À cet égard, des études du transport électronique ou du transport du spin à travers une molécule en fonction de sa configuration géométrique sur le substrat sont possibles. Dans ce travail de thèse, l'intérêt a été focalisé sur différents phénomènes clés de la conductance électronique à travers des objets nanométriques. Nous commençons avec une caractérisation approfondie des substrats, qui nous permet de bien distinguer entre des effets proprement liés à l'interaction molécule-surface et celles liés au substrat. Des atomes

individuels ainsi que des molécules de Phthalocyanine de cobalt (CoPc) ou de C_{60} sont étudiés en appliquant des techniques à la pointe de la technologie de STM et STS, comme l'imagerie par manipulation d'atomes ou la cartographie de la conductance différentielle (dI/dV) à une hauteur constante, en comparant toujours les résultats avec des calculs théoriques. Dans ce qui suit, les résumés des chapitres sont donnés.

L'introduction décrit le cadre général dans lequel s'inscrit ce travail. Elle est suivie par un premier chapitre, qui présente quelques techniques particulières du STM, comme la spectroscopie tunnel polarisée en spin (SP-STS), la cartographie de la conductance différentielle à hauteur constante et l'imagerie par manipulation d'atomes. Finalement, la préparation des échantillons et la spécificité des évaporateurs utilisés pour déposer des molécules et des atomes sont brièvement décrits.

Le chapitre 2 est dédié aux surfaces métalliques utilisées comme substrats. Dans la première partie, est discutée l'apparition des états de surface à la surface des monocristaux ainsi que la structure électronique de la surface (111) du cuivre autour du niveau de Fermi (E_F).

En suite sont présentées quelques propriétés des îlots ferromagnétiques de cobalt sur Cu(111). Ces îlots ont une taille d'une dizaine de nanomètres et représentent des surfaces magnétiques suffisamment large pour accueillir des adsorbants comme des atomes ou molécules individuels. Les propriétés électroniques, magnétiques et chimiques d'un nanoîlot sont gouvernées par la taille, la forme et la structure de l'îlot [2]. Ces derniers sont à leur tour profondément influencés par le désaccord de maille avec le substrat métallique. Les îlots ont la tendance à adopter le paramètre de maille de la surface sous-jacente [3]. Ainsi les distances entre les atomes dans un nanoîlot sont gouvernées par des contraintes.

Les nanoîlots de Co sur Cu(111) représentent donc un système de référence [4–8]. En enregistrant des spectres sur des îlots de taille croissante, il est démontré, que les états électroniques occupés présentent un déplacement en énergie en fonction de la taille de l'îlot, plus précisément une bande occupée de type d, se déplace en énergie. Un déplacement est aussi observé aux coins et aux arêtes des îlots par rapport à leur centre. Des simulations et des calculs *ab initio* démontrent que les positions énergétiques des états occupés sont fixées par les contraintes au sein des nanoîlots [9]. Ce travail valide l'hypothèse des relaxations "mésoscopiques" dans des nanoîlots. En outre, l'étude indique que l'état de surface peut être un senseur sensible pour des variations de la structure atomique à l'échelle nano. Pour la suite, ces résultats nous permettent

dans les études des atomes et molécules de comprendre les différentes structures électroniques liés au substrat.

Dans le chapitre 3 est présentée une étude sur des atomes individuels sur des îlots de cobalt. Cette étude est placée dans le contexte de la spintronique, c'est-à-dire l'électronique à l'aide des courants polarisés en spin. Dans la spintronique, un des buts prioritaires est l'amélioration de la qualité structurale des composants, comme par exemple dans des jonctions tunnel magnétiques [10]. Un atome métallique adsorbé sur une surface magnétique est la réalisation expérimentale la plus simple d'une électrode magnétique, facilement accessible par STM et STS. Par ailleurs, ces atomes peuvent simuler la corrugation et les impuretés présentes à l'interface d'une jonction tunnel magnétique, dont l'impact est considérable sur la magnétorésistance. Ces atomes représentent une opportunité pour étudier finement la relation entre la structure et les propriétés du spin.

Une étude récente a révélé, que des atomes de Fe et Cr sur des nanoîlots de cobalt sont polarisés en de spin en dessous de l'énergie de Fermi. En étendant les études de STS à d'autres atomes magnétiques (Ni, Co) et non-magnétiques (Cu) nous montrons ici que les états électroniques occupés de ces atomes présentent une signature spectroscopique commune [11]. Des calculs *ab initio* dévoilent que cette dernière résulte de la localisation des électrons quasi-libres majoritaires sur le site des atomes. Cet état lié, prédit aussi pour les atomes de Fe et Cr, domine la densité d'états des atomes dans cette gamme d'énergie, et il est responsable d'un renversement de la polarisation de spin par rapport à celle du substrat.

Le chapitre 4 est dédié aux molécules individuelles de CoPc sur Cu (111) et sur des îlots de cobalt. Dans la première partie du chapitre c'est décrit la molécule de Cobalt-Phthalocyanine (CoPc) sur Cu(111) en se focalisant sur l'interaction entre l'adsorption et la liaison chimique et le transport électronique à travers de la molécule. La géométrie d'adsorption à l'échelle moléculaire est déterminée par co-adsorption des atomes individuels et l'imagerie par manipulation atomique [12]. L'atome central de CoPc est positionné *bridge* entre deux atomes de la surface, un pair des unités de benzopyrrol en parallèle avec la direction cristalline [110] du Cu(111). Les calculs montrent, que la liaison chimique est déterminée par la compétition entre les différents parties du ligand organique, c'est-à-dire les atomes d'azote et des anneaux benzéniques. Finalement la structure électronique est décelée par la cartographie de la conductance différentielle à la hauteur constante et par des calculs. Au-dessous du E_F le transport est dominé par l'atome

central de Co, par contre au-dessus du E_F le ligand joue un rôle important. La symétrie observée dans les images de dI/dV change dramatiquement avec la tension et indique qu'il n'y a pas de déformation de la molécule.

La deuxième partie du chapitre 4 présente des résultats obtenus sur des molécules de CoPc déposées sur des îlots de cobalt. Le spin du CoPc est couplé d'une manière ferromagnétique et l'état du spin est visualisé par la cartographie de la conductance différentielle polarisée en spin. Ces mesures représentent les premières études du SP-STM sur des molécules. Ils accentuent le rôle important du site d'adsorption pour le couplage magnétique entre la surface et la molécule et mettent en avant la nécessité de sa détermination exacte.

Dans le chapitre 5 est présentée la résistance différentielle négative (NDR) observée dans des monocouches de C_{60} sur Cu(111) et sur des nanoîlots sur Cu(111). La NDR est une caractéristique de certains dispositifs électroniques et a été observée pour la première fois par Leo Esaki en 1958 dans des diodes à effet tunnel de Germanium. Dans des couches moléculaires, ce phénomène a récemment attiré beaucoup d'intérêt [13–17], vu des applications potentielles dans l'électronique moléculaire. Récemment, un mécanisme de NDR pour un composant organométallique absorbé directement sur la surface métallique était démontré. Ce mécanisme est basé sur l'accord des symétries des orbitales moléculaires (MOs) et des orbitales atomiques (AOs) de la pointe [16]. Un effet similaire basé sur l'accord et le désaccord énergétique des MOs et des AOs est prédit pour des couches de C_{60} sur Cu(111) [16].

Dans ce contexte, on a étudié des monocouches de C_{60} sur Cu(111) et sur des nanoîlots de cobalt sur Cu(111). Malgré des paramètres de maille très semblables ($\Delta a < 1\%$) les molécules adsorbent différemment sur les deux surfaces. En même temps les propriétés du transport dans la jonction tunnel changent. Sur cobalt un NDR est observé. Par contre C_{60} sur Cu(111) produit juste une chute de la conductance différentielle à zéro. Cet effet est lié à une combinaison des MOs intense avec l'accord et le désaccord d'énergie des MOs de C_{60} et des AOs de la pointe en fonction de la tension appliquée. La thèse est achevée par un récapitulatif des résultats obtenus en finissant sur une ouverture vers des études en cours et à l'avenir.

Contents

Introduction	1
1 STM and technical basics	3
1.1 Scanning tunneling microscopy	3
1.1.1 Point spectroscopy and mapping	6
1.1.2 Spin-polarized scanning tunneling microscopy and spectroscopy	8
1.2 Sample and tip preparation	10
2 Two model (111) surfaces	13
2.1 The (111) surface of copper	14
2.1.1 Electronic states at the surface	14
2.1.2 Surface states of Cu(111)	14
2.2 Cobalt nanoislands on Cu(111) - a magnetic (111) surface	18
2.2.1 Cobalt growth on Cu(111)	19
2.2.2 Spin-polarized surface states of cobalt nanoislands	21
2.2.3 Changing the band structure - influence of the interatomic distances	25
Summary and conclusions	32
3 Electronic states above an adatom on a magnetic surface	35
3.1 Single atoms in spin-polarized STM experiments	36
3.2 Unveiling SP contributions to the LDOS above adatoms on cobalt islands	39
3.2.1 Differential conductance above adatoms on cobalt nanoislands	39
3.2.2 Localization of dispersive surface states by an adatom	41
3.2.3 Newns-Anderson model for surface impurities	43
3.2.4 Density of states: surface induced states versus atomic resonances	45

Summary and conclusions	49
4 Single CoPc molecules on a magnetic and a nonmagnetic surface	53
4.1 Cobalt-Phthalocyanine - a brief introduction	54
4.2 Cobalt-Phthalocyanine on Cu(111) - how adsorption affects transport properties	55
4.2.1 Unveiling the adsorption site of CoPc on Cu(111)	57
4.2.2 Contributions to the adsorption energy	61
4.2.3 Electronic transport and hybridization of CoPc/Cu(111)	62
4.3 CoPc on cobalt nanoislands	70
4.3.1 Adsorption of CoPc on cobalt islands	72
4.3.2 Spin-polarized spectroscopy and conductance maps of single molecules	73
Summary and conclusions	77
5 Negative differential resistance in a C₆₀ monolayer	79
5.1 C ₆₀ - the buckminsterfullerene	80
5.2 Negative differential resistance in STS	81
5.3 C ₆₀ adsorption on cobalt islands and on Cu(111)	84
5.4 C ₆₀ on cobalt - observing an NDR	86
5.4.1 Differential conductance	86
5.4.2 The role of the tip-sample distance	88
5.4.3 Simple model for the local orbital matching	90
5.4.4 Tunneling conductance by DFT	93
5.5 C ₆₀ on Cu(111) - weakening the NDR	96
5.5.1 dI/dV as function of the molecular orientation	97
5.6 C ₆₀ on the tip apex - tuning the NDR	99
5.6.1 Orientation of C ₆₀ at the tip apex	102
5.6.2 NDR produced by a Shockley surface state	104
Summary and conclusions	105
Conclusion and perspectives	107
Bibliography	113
List of figures	133

Symbols, acronyms and abbreviations 137

Curriculum Vitae 141

List of publications 143

List of presentations 145

Introduction

In 1959, Richard Feynman delivered a now-famous speech entitled "There's plenty of room at the bottom" [1], in which he foresaw a general down-scaling of data storage, computing and mechanics including predictions of a minimally invasive surgery or computer based image recognition systems, which must have sounded futuristic to his audience, but some have become reality today. He also came up with the idea of an electronic based on atomic-scaled devices, even though the techniques of those days allowed neither for the development nor for the study or imaging of structures at this scale. Today, 50 years later, this idea, the idea of *molecular electronics*, represents one of the most promising pathways to render an ongoing miniaturization of electronic devices possible. The term *molecular electronics* can be understood as an electronic circuitry based on molecular devices or, more generally, as electronic circuits on a molecular scale, which includes also devices based on ordered arrays of atoms, atomic chains or individual atoms [18]. A variety of advantages are expected, when replacing the silicon-integrated electronics by an electronic based on organic substances: new functionalities, less energy consumption for production and operation, environment-friendly materials, more robust and persistent or highly flexible devices *etc.*

Nowadays molecular engineering is able to provide functionalized molecules acting as active elements, which are designed to fulfill precisely the different roles in an electronic circuit. However, for the external communication and control, the organic device has to be brought into contact with inorganic leads. This organic-inorganic contact is crucial, as it alters the properties of the molecule and determines the functionality of the device. Therefore one of the most urgent tasks in the field of molecular electronics is to understand and tune the contact between molecules and a metal lead. Scanning tunneling microscopy and spectroscopy (STM and STS) represent a unique tool to correlate electronic and structural properties at the nanoscale, such as the impact of geometry on the spin-transport through a single molecule. In this perspective, the work presented here employs STM/STS as well as spin-polarized STM/STS to focus on

key phenomena of the conductance of nanoscaled objects, *e.g.* metallic islands, single atoms and molecules.

After a brief introduction of the STM/STS techniques employed, **Chapter 1** provides some technical details regarding the sample and tip preparation. **Chapter 2** is dedicated to the characterization of the Cu(111) surface and of cobalt islands grown on this surface. Both are used as substrates for the adsorption of atoms and molecules. Knowledge gathered on the electronic structure of these surfaces allows then distinguishing properties due to the molecule-surface interaction from substrate related effects as shown in **Chapter 4**. **Chapter 3** focuses on individual atoms adsorbed on cobalt islands. The polarization of the local density of states (LDOS) above the atoms is discussed in relation with the polarization of the surface. Surface induced states and atomic resonances are shown to determine the LDOS above the atom, as well as the spin-polarization around the Fermi energy (E_F).

In the last two chapters, results are obtained on two different molecules, namely for Cobalt-Phthalocyanine (CoPc; **Chapter 4**), and C_{60} (**Chapter 5**), both molecules being model systems for future molecular electronic devices. Challenging STM/STS techniques like "manipulated atom imaging", spin-polarized (SP) STS or differential conductance (dI/dV) mapping at a constant height are employed. These techniques reveal molecular conductance channels and the spin-polarization of a single molecule (**Chapter 4**), as well as a negative differential conductance, which originates from an energy-dependent match and mismatch of molecular orbitals and electronic tip states (**Chapter 5**).

CHAPTER 1

STM and technical basics

This chapter gives a brief summary of the physical principles of the scanning tunneling microscope (STM) and introduces the scanning modes employed for the experiments. Constant-current topography mode, differential conductance (dI/dV) spectroscopy and mapping, which yield information about the density of states (DOS), as well as spin-polarized (SP) measurements or "manipulated atom imaging" are presented. In the second part, technical details of the sample preparation are given, such as deposition of individual metal atoms and molecules, or preparation of the substrate.

1.1 Scanning tunneling microscopy

STM is based on the principle of quantum tunneling. When two metal electrodes are approached sufficiently close, low-energy electrons can "tunnel" from one electrode to the other across the vacuum barrier. In an STM configuration the tip and the sample represent these two electrodes. Figure 1.1 presents a scheme of the STM junction with applied negative (Fig. 1.1a) and positive (Fig. 1.1b) sample bias, respectively. In a semiclassical Wentzel-Kramer-Brillouin (WKB) approximation and with $k_B T \ll eV$, the net tunneling current I can be written as:

$$I \propto \int_0^{eV} \rho_t(E - eV) \rho_s(E) T(E, eV, z) dE, \quad (1.1)$$

where $\rho_t(E - eV)$ and $\rho_s(E)$ are the energy dependent DOS of the tip and the sample, respectively; V is the applied bias; z is the tip-sample distance and $T(E, eV, z)$ is the transmission

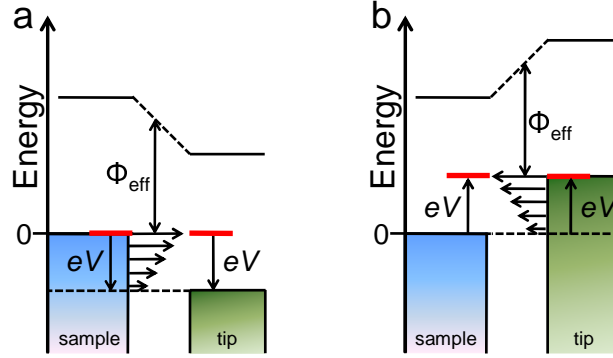


Figure 1.1: Scheme of the STM tunnel junction. a) Negative sample bias: electrons tunnel from occupied sample states into unoccupied tip states. b) Positive sample bias: electrons tunnel from occupied tip states into unoccupied sample states. V is the applied bias, Φ_{eff} the effective tunneling-barrier height. Figure adapted from Ref. [19].

probability. This probability in turn is expressed as:

$$T(E, eV, z) \propto \exp\left(-2z \left(\frac{2m}{\hbar^2} \left(\frac{\Phi_t + \Phi_s}{2} + \frac{eV}{2} - E\right)\right)^{\frac{1}{2}}\right), \quad (1.2)$$

where Φ_t and Φ_s are the work functions of tip and sample, respectively [20, 21]. Combining Equation 1.1 and 1.2, we find that I depends exponentially on the tip-sample distance z :

$$I(z) \propto \exp\left(-A\sqrt{\bar{\Phi}}z\right), \quad (1.3)$$

with an average work function $\bar{\Phi} = (\Phi_t + \Phi_s)/2$ in the order of 4 eV and $A = 2\sqrt{2m/\hbar^2} = 1.025 (eV)^{-1/2} \text{ \AA}^{-1}$. Typical currents collected are between 1 pA and 10 μA . For a sample bias of 100 mV, this corresponds to a change in the tip-sample distance from $z \approx 10 \text{ \AA}$ to a tip-sample contact, where $z \approx 3 \text{ \AA}$. The constant current mode of the STM exploits this exponential dependence. In this mode a feedback loop ensures a constant tunneling current at each pixel of the image by adjusting the height, *i.e.* the tip-sample distance, while scanning the surface. By doing so, a topograph of the surface is recorded. However, as the current does not only depend on the height, but also on the DOS and the transmission probability, the observed heights can vary with bias and are consequently defined as "apparent" heights.

In this thesis, we used the Cu(111) surface and cobalt islands grown on Cu(111) as substrate. Even though atomic resolution of the close-packed Cu(111) surfaces can be achieved in the

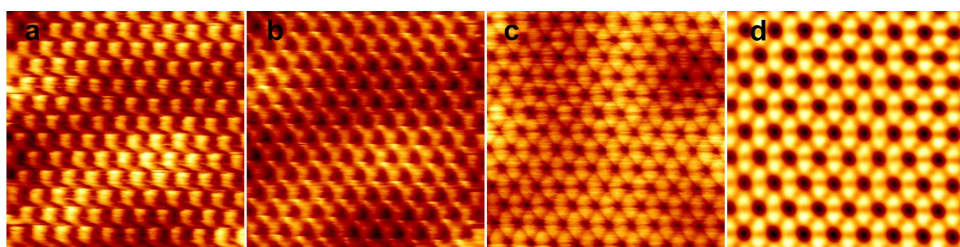


Figure 1.2: Manipulated atom images of Cu(111). a, b and c) raw images corrected for the background slope [size: $27 \times 27 \text{ \AA}^2$, gap conditions: -5 mV and 25 nA (a and b) or 15 nA (c)]. The manipulated atom image can depend on the scanning angle relative to the lattice, the gap voltage and current and on the microscopic tip shape. d) same image as in (c) after an advanced image treatment ($22 \times 22 \text{ \AA}^2$, -5 mV , 15 nA).

"normal" constant-current topography mode (see for example Ref. [22]), due to the weak electronic corrugation of the surface this is not feasible in a routine manner with all kind of tips. To overcome this drawback Stroscio and Celotta proposed in 2004 a new method [12], a similar approach being used for a (110) surface earlier [23]. For their experiment, Cobalt atoms are deposited onto a Cu(111) surface, the tip is positioned above an adsorbed atom (adatom) and the tip-sample distance is decreased by adjusting the gap conditions accordingly. Typical gap voltages are in the range of $\pm 10 \text{ mV}$ and gap currents are in the order of 20 nA . The created localized surface-potential well traps the atom underneath the tip [12, 23, 24]. When moving the tip laterally, the adatom follows the tip motion and "hops" from one hollow site of the surface to the next. Entire images can be acquired under these conditions, which are called "manipulated atom images". They show the hollow sites of the surface as protrusions, while surface atoms are imaged as depressions. Figure 1.2a, b and c show three examples of resulting images with no further treatment other than a correction for the background slope (Figure 1.2d being the same image as in c after a Fourier transform). The appearance of the acquired images depends on the scanning angle, the gap voltage and current, as well as the tip employed, which, depending on its apex geometry, may modify the trapping potential. However, the surface symmetry, the surface atom positions and the distances can be extracted regardless the image appearance. The above-described method allows for an *in situ* calibration of the piezo taking into account thermal drift. We will use this method to resolve the adsorption geometry of Cobalt-Phthalocyanines on Cu(111) in section 4.2.1.

1.1.1 Point spectroscopy and mapping

As briefly described above, the tunneling current depends on the DOS of the sample, which can be accessed by the differential conductance dI/dV . The differentiation of Equation 1.1 with respect to V yields in fact:

$$\frac{dI}{dV}(V) \propto \rho_t(0) \rho_s(eV) T(E, eV, z) + \int_0^{eV} \rho_t(E - eV) \rho_s(E) \frac{T(E, eV, z)}{dV} dE, \quad (1.4)$$

when assuming a constant tip DOS equal to the DOS at the Fermi level (E_F). In a further approximation, we assume T to be constant in energy near the Fermi level. The differential conductance can then be written as:

$$\frac{dI}{dV}(V) \propto \rho_s(eV) T(z), \quad (1.5)$$

As shown by Equation 1.5, recording the dI/dV as a function of the bias, *i.e.* acquiring a dI/dV spectrum, gathers information on the sample DOS. This operation mode is defined as scanning tunneling spectroscopy (STS). The dI/dV can either be calculated numerically by differentiation of the current-voltage curve, or, more conventionally, can be measured directly by means of a lock-in technique. Using a lock-in amplifier the bias voltage V is modulated by a sinusoidal signal of amplitude V_m with a frequency superior to the feedback loop frequency. For the experiments presented in this work, a lock-in detection was employed with modulation frequencies between 500 Hz and 7 kHz.

The spectral resolution in STS depends on two factors, the thermal broadening and the broadening due to the voltage modulation for the lock-in detection, and is expressed as:

$$\Delta E = \sqrt{\Delta E_T^2 + \Delta E_M^2}.$$

The thermal broadening ΔE_T originates from the temperature dependence of the Fermi–Dirac distribution function [25], and can be expressed as: $\Delta E_T = 3.5 k_B T$, which yields a broadening of 1.3 meV at 4.2 K. This is substantially smaller than the natural width of all spectral features studied in this thesis and can therefore be neglected here. The broadening introduced by the bias modulation ΔE_M however depends on the modulation amplitude as follows: $\Delta E_M = \sqrt{3} V_m = \sqrt{6} V_{rms}$ [26], where V_m is the amplitude of the modulation, while V_{rms} is the root mean square of the modulation. A modulation of $V_{rms} = 15$ mV yields a broadening of 36 mV, which is of

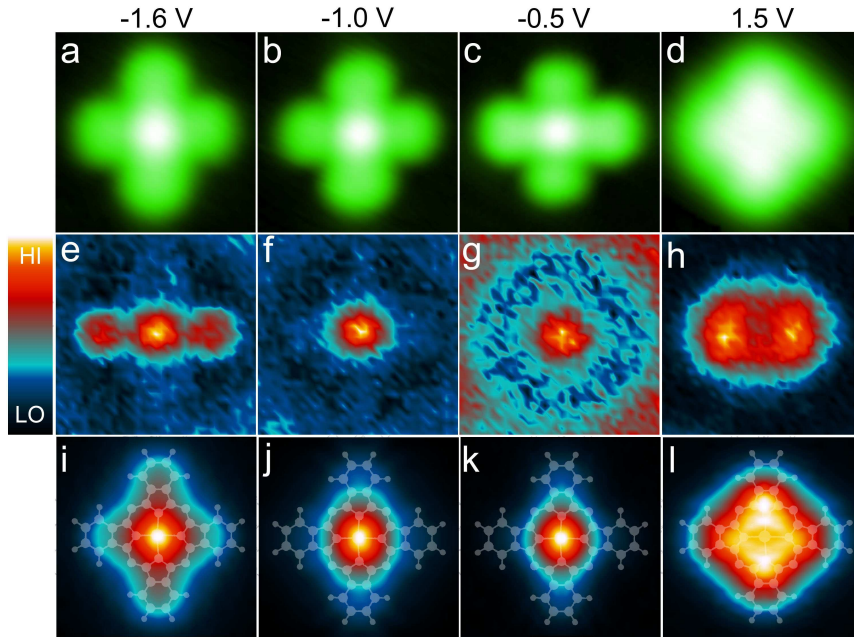


Figure 1.3: Constant-height versus constant-current images. a–d) Constant-current topographic images of a single CoPc molecule at various biases (image size: $23 \times 23 \text{ \AA}^2$, tunneling current: 0.5 nA). e–h) Corresponding constant-current dI/dV maps (image size: $23 \times 23 \text{ \AA}^2$, feedback loop open at 0.1 nA and 0.4 V). i–l) Corresponding constant-height dI/dV maps (image size: $23 \times 23 \text{ \AA}^2$, a scaled molecular scheme is superimposed to each map). The feedback was open above the copper surface at 0.01 nA and at (i) -1.6 V , (j) -1.0 V , (k) -0.5 V , and (l) 1.5 V , and kept open during the image acquisition. The signal-to-noise ratio and the intramolecular resolution improve in these images with respect to the constant-current dI/dV maps. These maps closely reflect the LDOS above the sample in a plane parallel to the surface plane.

the same order of magnitude as the width of spectral features like the Shockley surface state of Cu(111) [*cf.* chapter 2]. Throughout the thesis, V_{rms} was chosen carefully to ensure that ΔE_M was small with respect to the natural line width of the spectroscopic features of interest, typical values lying between 1 and 15 mV depending on the required spectral resolution.

Besides the acquisition of local dI/dV curves in point spectroscopy, the dI/dV can also be acquired at each pixel of a scanned area. These images, or dI/dV maps, allow visualizing the spatial changes of the differential conductance. This can either be done by opening the feedback loop at each point of the map and recording a full spectrum, or by simply recording the dI/dV signal at the working bias simultaneously with the z or I signal, respectively. dI/dV

maps represent, in a first approximation, the spatial distribution of the DOS at a given energy, which can unveil the correlation of specific electronic states, *e.g.* molecular orbitals, with geometric features, *e.g.* a side chain of a molecule. In many cases recording dI/dV maps in the constant-current mode will yield the desired information, even though the tip-sample distance can change in each pixel to match the gap conditions. This occurs, for instance, when imaging a molecule adsorbed on a metal surface with a spatial-dependent DOS. Changes in the DOS and in z are then mingled (see Eqs. 1.1 and 1.2), potentially leading to a loss of information or artifacts [21, 27, 28]. Under certain circumstances, it can therefore be advantageous to record the dI/dV maps in the constant-height mode rather than in the constant-current mode. In the constant-height mode the surface is scanned with an open feedback at a constant tip-surface distance. In this case, the dI/dV is proportional to the sample local density of states (LDOS) in a plane parallel to the surface plane. This implies a careful correction of any background slope. As an example, Figure 1.3 presents topographs, constant-current dI/dV maps and constant-height dI/dV maps of a Cobalt-Phthalocyanine on Cu(111) at different biases. The maps at -1.6 V and 1.5 V show clear differences in the localization of the high conductance regions between constant-current and constant-height maps. In this case, a better signal-to-noise ratio is observed for the constant-height dI/dV maps compared to the constant-current ones, presumably because the feedback loop remains open during acquisition.

1.1.2 Spin-polarized scanning tunneling microscopy and spectroscopy

So far, we considered a nonmagnetic tip and a nonmagnetic sample in the descriptions of the tunneling process. However STM/STS can also be used to explore the spin-polarized (SP) nature of a sample by means of spin-polarized tips, either ferro- or antiferromagnetic. Figure 1.4 provides a schematic view of the spin-polarized tunneling process. Following Wortmann *et al.* we can write the tunneling current as follows, neglecting any changes in the transmission probability and taking the tip DOS as constant ($n_t(E) = n_t = \text{const.}$) [30]:

$$I \propto \int_0^{eV} n_t n_s(E) dE + \int_0^{eV} \vec{m}_t \vec{m}_s(E) dE, \quad (1.6)$$

where n_t is the sum of the tip DOS of spin-up (ρ_t^\uparrow) and spin-down (ρ_t^\downarrow) electrons: $n_t = \rho_t^\uparrow + \rho_t^\downarrow$, and $n_s(E)$ being equal to $\rho_s^\uparrow(E) + \rho_s^\downarrow(E)$. The scalar product in the second integral can be written as $\vec{m}_t \vec{m}_s(E) = m_t m_s(E) \cos \theta$ with θ being the angle between the tip and the sample

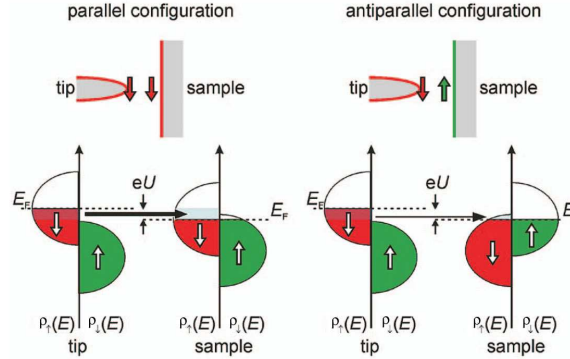


Figure 1.4: Principle of spin-polarized STM: the spin-polarized tunneling current flowing between a magnetic tip and a magnetic sample depends on the relative alignment of the local magnetization of tip and sample as well as on the spin polarization of the electronic states of tip and sample contributing to the tunneling current. Figure adapted from Ref. [29].

magnetization directions. $\vec{m}_t = \rho_t^\uparrow - \rho_t^\downarrow$ and $\vec{m}_s(E) = \rho_s^\uparrow(E) - \rho_s^\downarrow(E)$ are the differences of the spin-up and the spin-down DOS of the tip and the sample, respectively. Their direction is aligned with the tip and sample magnetization, respectively, but can be either parallel or antiparallel at a given energy. In turn, the magnetization is proportional to the integral of \vec{m} over all occupied states:

$$\vec{M}_t \propto \int_{-\infty}^0 \vec{m}_t(E) dE \quad \text{and} \quad \vec{M}_s \propto \int_{-\infty}^0 \vec{m}_s(E) dE. \quad (1.7)$$

The differentiation of Eq. 1.6 with respect to the applied bias yields:

$$\frac{dI}{dV}(V) \propto n_t n_s(eV) + \vec{m}_t \vec{m}_s^>(eV). \quad (1.8)$$

So the spin-polarized differential conductance can be expressed as a sum of a non-polarized term $n_t n_s(eV)$ and an SP term $\vec{m}_t \vec{m}_s^>(eV)$, which depends on the spin-polarization of the two electrodes at a given energy and the relative orientation of their magnetization. Current theoretical effort is devoted at improving Equation 1.6, in particular at including the spin-dependence of the transmission probability. For an review on the principles and methods of SP-STM and SP-STs see for example Ref. [29]. Section 4.3 presents an SP-STs study on CoPc molecules adsorbed on magnetic cobalt nanoislands (see Figs. 4.14 and 4.15 for examples of SP measurements on individual molecules).

1.2 Sample and tip preparation

A commercial OMICRON STM operating in ultra-high vacuum conditions at 4.6 K was used during this thesis to investigate metal islands, individual atoms and molecules residing on metal surfaces. In the following a brief overview of the *in vacuo* sample preparation is given.

Crystal preparation: The Cu(111) surface was cleaned *in vacuo* by repeated cycles of argon ion bombardment and annealing to ≈ 700 K until the crystal showed large terraces up to 100 nm wide and an impurity level as low as one impurity per 100 nm².

Cobalt island preparation: Two atomic layers high cobalt nanoislands were obtained by evaporating 0.7 monolayers (MLs) of Co at 0.15 ML/min onto the Cu(111) surface at room temperature from a thoroughly outgassed Co rod. After deposition, the sample was immediately transferred into the pre-cooled STM to avoid Co–Cu intermixing. A typical image after cobalt deposition is presented in Figure 2.5 of chapter 2.2.

Atom deposition: Metal atoms tend to diffuse on metal crystalline surfaces until they find a stable adsorption site, usually step edges or defect sites. Thus, if individual adatoms are needed, they have to be deposited at temperatures as low as possible. The kinetic energy of the incoming atoms is then no longer sufficient to overcome the diffusion barrier at the surface. In this work we used two types of low-temperature metal atom deposition, namely through a classical evaporation technique carried out *in situ* in the STM chamber, and through controlled tip-sample contacts as described below.

i) *Atom deposition by metal evaporation:* The evaporator consists of a wire of the desired element, in our case Cu, Au, Co and Fe (> 99.99% purity), which is wound around a tungsten spiral (wire diameter: 0.25 mm; spiral diameter: ≈ 5 mm) as presented in Figure 1.5c. A current passing through the tungsten wire heats the points of contact between the wire and the tungsten spiral, small amounts of the chosen element being then evaporated. Figure 1.5b shows the homebuilt metal evaporator charged with copper (left) and cobalt (right), respectively, hosting two metal spirals at a time. The tungsten spiral wrapped with wires of the desired element is connected at one end to a copper electrode and at the other end to the stainless steel tube, which is grounded. At the same time, the tube acts as a shield to prevent evaporation from one



Figure 1.5: Homebuilt evaporators: a) molecular evaporator. The substance powder is held by a ceramic crucible and evaporated by means of Joule heating through a wiled tantalum filament. b) multiple-metal evaporator. The metal wire is wound around a tungsten filament [shown in (c)]. By means of joule heating small amounts of atoms can be evaporated, the shielding tubes preventing cross-contamination of the filaments.

wire onto the other one. The evaporator was installed in the STM chamber in a way that the atom beam reached the sample surface in the STM when opening the liquid-helium shield of the cryostat. The sample temperature during evaporation increased from 4.6 to approximately 10 K due to the opening in the shield. After thoroughly degassing the wires, atoms of the different elements were evaporated onto the cold surface. Different coverage in the order of 0.1 atoms/nm^2 could reproducibly be obtained with no appreciable increase of other impurities. Figure 3.5 in chapter 3 shows the result of copper deposition onto a cold Cu(111) surface and in Figures 5.19 the deposition of atoms of different elements onto a ferrocene layer is presented.

ii) *Atom deposition by tip-sample contact*: Alternatively single nickel, cobalt, and copper atoms were deposited onto the substrate by a controlled transfer of the tip-apex atom as described by Limot *et al.* [31], so that isolated atoms residing at the desired location could be obtained as presented in Figure 3.3 (page 38). To do so, the feedback loop is opened above the clean substrate and the tip is held at a bias in the order of 10 mV. The tip is approached towards the surface until a tip-sample contact is established (the junction resistance is then close to $12.9 \text{ k}\Omega$), and finally retracted back to the feedback position. In 80% of the cases STM topography shows then a single atom left at the contact site, where the tip was positioned before the approach. The coating material of the tip apex is chosen accordingly to the desired atom.

Molecule deposition: For the deposition of CoPc and C₆₀ a homebuilt evaporator shown in Figure 1.5a was employed. It consists of a ceramic crucible holding the substance powder and a tantalum-foil spiral wound around the crucible. The crucible is heated by means of Joule heating, *i.e.* a current flow through the tantalum ribbon.

CoPc was provided as 95% pure powder by *Alfa Aesar*. Prior to deposition the powder was cleaned *in vacuo* by thorough degassing and by sublimation. Deposition was carried out at temperatures ≥ 400 K. A calibration of the deposition rate allowed for well-defined and reproducible coverage in the order of fractions of a monolayer with deposition times of several seconds.

Vacuum sublimated C₆₀ was provided as 99.9% pure powder by MER CORPORATION. After thoroughly degassing the powder *in vacuo*, C₆₀ was deposited at 400 K. No noticeable increase of the impurity concentration on the surface was detected after deposition.

Tip preparation: For the STM/STS experiments described in this thesis different kind of STM tips were used. All tips employed were chemically etched prior to the introduction into the vacuum chamber and then cleaned *in vacuo* by argon-ion bombardment and annealing. Tungsten tips, which were employed for most of the experiments, were subsequently treated by soft indentations into the clean copper surface and therefore the tip apex was presumably coated with copper.

For the deposition of single atoms described in chapter 3 nickel tips as well as cobalt or copper coated tungsten tips were used. For the SP experiments of section 4.3 cobalt coated Ni tips were employed. All tips were treated by indentations and/or voltage pulses until tip-structure artifacts were negligible in the dI/dV over the voltage range of interest, the step-like onset of the Shockley surface state of Cu(111) appearing then as a sharp feature in the dI/dV (*cf.* Fig. 2.3).

CHAPTER 2

Two model (111) surfaces ¹

This chapter is dedicated to two archetype (111) metal surfaces, namely the (111) surface of a copper single crystal and cobalt nanoislands grown on this surface. The electronic structure of the copper surface near the Fermi energy (E_F) is governed by a Shockley surface state [32], situated in the projected bulk band gap. It is a suitable model substrate for studies of adsorbates, such as single atoms (*cf.* chapter 3) or molecules (*cf.* chapters 4 and 5). Its electronic properties will be introduced in the first part of the chapter. Contrary to copper, the cobalt islands hold a complex density of states with spin-polarized (SP) states near E_F , *i.e.* majority and minority bands are shifted in energy with respect to each other. The existence of magnetic surfaces with opposite magnetization in the nanometer range makes these islands a model playground for SP-STM studies [7, 8, 33]. Nevertheless a detailed knowledge of how the crystal structure influences the electronic structure of these islands is indispensable to identify spin-related properties [6]. Therefore a detailed study of the LDOS of the islands is presented, determining the origin and character of the different electronic states. The influence of stacking and size as well as inhomogeneities in the island, *i.e.* differences in the LDOS in the center compared to edge or corner sites of the island, are unveiled. A pathway towards an interpretation in terms of strain, interatomic distances and "mesoscopic" relaxation [34, 35], will be presented.

The theoretical calculations presented in this chapter have been carried out by Pavel Ignatiev,² Valeri Stepanyuk² and Patrick Bruno^{2,3} in the framework of a publication [9].

¹This chapter presents results published in *Phys. Rev. Lett.* **99** 246102 (2007)

²Max-Planck-Institut für Mikrostrukturphysik, Halle

³Present address: European Synchrotron Radiation Facility, Grenoble

2.1 The (111) surface of copper

2.1.1 Electronic states at the surface

The broken three-dimensional periodicity near the surface of a metal modifies the electronic structure compared to the bulk. The more the electrons of a band are delocalized, the stronger are these changes. In the surface region, the electronic wave functions differ therefore from the Bloch wave functions of the infinite crystal. Two types of waves are possible [36, 37]. There are extended wave functions, describing bulk electrons, which propagate towards the surface, and which are reflected by the surface and propagate back into the bulk. These states decay exponentially into the vacuum but extend into the bulk. If these states have an enhanced weight at the surface, they are called surface resonances. Second, there are wave functions localized in the vicinity of the surface decaying both into bulk and vacuum. These surface states host electrons that are trapped in the surface region but propagate along the surface. They exist, under certain conditions, in gaps of the projected bulk band structure at the surface of a metal and can be regarded as an electron wave trapped between the bulk crystal and the surface barrier [38]. Due to their infinite extension in the two dimensions parallel to surface and the localization in the third dimension perpendicular to the surface, these states are regarded as a quasi-two dimensional electron gas (2DEG). However their effective mass usually differs from the mass of free electrons [39]. The energy at which the surface state occurs is determined by the phase shift of the wave upon reflection at the crystal and at the vacuum barrier. The following condition for the round-trip phase accumulation ϕ has to be matched [40]:

$$\phi(E) = \phi_C(E) + \phi_B(E) = 2\pi n , \quad (2.1)$$

n is an integer, ϕ_C and ϕ_B are the phase shift upon electron reflection at the crystal and the surface barrier, respectively. Hence, if surface states exist in a projected bulk band gap, their energy and number depend on the amplitude of the energy-dependent variation of the phase accumulation.

2.1.2 Surface states of Cu(111)

Under standard vacuum conditions, the (111) surface of the face centered cubic (fcc) copper crystal is unreconstructed and hence weakly corrugated. Figure 2.1 illustrates the energy-

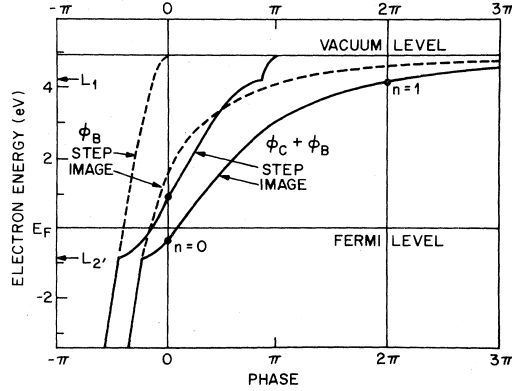


Figure 2.1: Phase variation upon reflection as a function of energy for the L gap in Cu(111). Figure adapted from Ref. [40].

dependent variation of the phase shift for electrons reflected at the crystal and at the vacuum barrier. The $L_{2'} \rightarrow L_1$ band gap at the $\bar{\Gamma}$ -point is a so-called "Shockley inverted" gap, as the p -like $L_{2'}$ level lies below the s -like L_1 level [42]. For the two other low-index surfaces of copper, *i.e.* (110) and (001), the same L gap occurs at the \bar{Y} -point and \bar{X} -point, respectively [40]. As shown by Figure 2.1 the first solution ($n = 0$) of equation 2.1 is found below E_F and yields a Shockley surface state [32]. The appearance of this state can be evidenced by angle-resolved photoemission spectroscopy (ARPES) [39, 41, 43], or STM/STS [44, 45], as is presented in Figures 2.2 and 2.3, respectively. A second solution ($n = 1$) is found close to the top of the gap more than 3 eV above E_F . This image state originates from the long-range nature of the image potential at the surface. Further solutions for $n \geq 2$ are found, but lie within the upper L_1 bulk band. Thus they can extend into the bulk and form image surface resonances [36], the $n = 2$ states being observed by two-photon photoemission [46]. We will focus our attention on the Shockley surface state ($n = 0$) as it is involved in the adsorption and LDOS of adsorbed atoms (called "adatoms" in the following; see chapter 3 for details) and molecules. Figure 2.2 presents results of ARPES measurements on the Cu(111) surface. The Shockley surface state centered at the $\bar{\Gamma}$ -point is clearly visible in Figure 2.2a. Figure 2.2b shows the parabolic dispersion of this state as extracted from the measurements. An analysis of the ARPES data leads to a natural peak width for the surface state at the bottom of the band of 23 meV, which corresponds to a lifetime of 29 fs [41]. Contrary to Au(111), no k splitting of the surface state due to a spin-orbit coupling is observed [41].

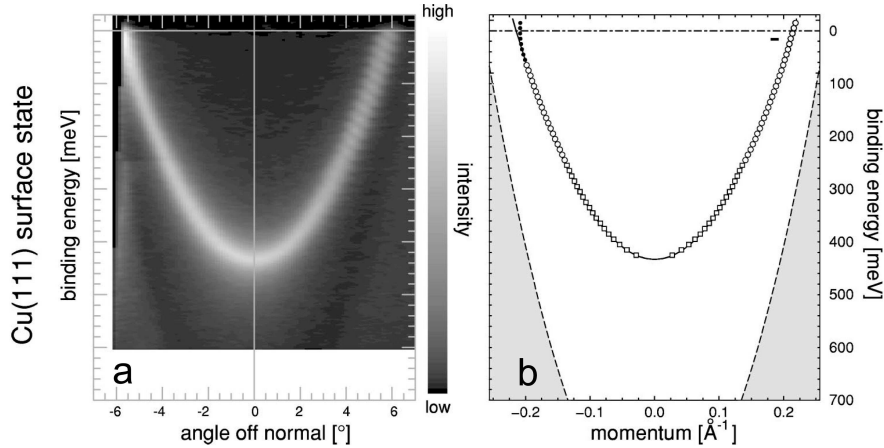


Figure 2.2: a) Shockley surface state of Cu(111) near $\bar{\Gamma}$ as measured by ARPES. b) Parabolic dispersion of the surface state as extracted from the ARPES measurements in (a). The areas in grey are projected bulk states of copper. Figure adapted from Ref. [41].

STS of the surface states is shown in Figure 2.3. Below -1 V the differential conductivity increases sharply as the bottom of the bulk gap is reached. Between -1 and $+3$ V, the dI/dV is quite flat, presenting just a small feature below E_F . The flat background originates from tunneling from and into bulk states, but is weak compared to lower energies due to the bulk band gap around the $\bar{\Gamma}$ -point. The inset of Figure 2.3 reveals the nature of the small feature observed below E_F . Just below E_F a step-like onset is detected and corresponds to the bottom edge of the surface band. Its energy can be determined to be -0.445 eV as indicated by a grey line. Kliewer *et al.* have, in good agreement with the ARPES data, determined a natural peak width at the bottom band edge of 24 meV [45]. Additionally to the dI/dV spectrum, STM can visualize the surface states by imaging the standing wave pattern of the scattered surface state electrons. Scattering may occur at copper step edges [44, 47, 48], nanoislands (*cf.* Fig. 2.4), single atoms (*cf.* Fig. 3.5) or adsorbed molecules. Figure 2.4 shows a standing wave pattern around cobalt nanoislands at a bias of 200 mV. The spatial oscillations in the images can be used to determine the wave vector at given energies and thereby estimate their parabolic dispersion and effective electron mass (of $0.38 m_e$ [44]). Repp *et al.* showed that the surface state electrons can mediate long-range interaction between transition-metal adatoms and thus influence the atom adsorption at low temperatures [49]. At the same time a localization of the surface state at the adatom site appears, which is referred to as bound state [50–52], and

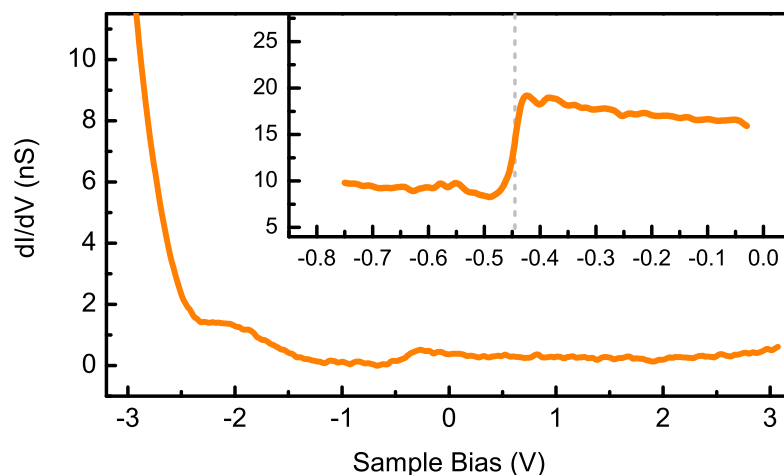


Figure 2.3: Differential conductance over Cu(111). A typical dI/dV spectrum acquired above Cu(111) from -3 to $+3$ V (feedback opened at 5.0 nA and -3.0 V). The high-resolution spectrum in the inset shows the step-like onset of the Shockley surface states at -0.445 V (feedback loop opened at 0.50 nA and -0.03 V).

will be treated in detail in chapter 3. So-called quantum corrals, *i.e.* specifically ordered arrays of adatoms produced by means of tip-assisted atom manipulation [53–56], or of self-assembled molecular structures [57] can be used to confine the surface-state electrons.

The surface state itself is highly sensitive to the presence of adsorbates like atoms or molecules. In many cases the adsorption removes the surface state completely. However it has been shown that alkali metals [58], and rare gases [59, 60], modify the electronic structure just slightly, so that the surface state survives but shifts in energy. Furthermore the adsorption of monolayers of salt transform the surface state into an interface state, which, however, keeps its nearly free-electron-like character and can be investigated by means of STM [61]. The adsorption of specific organic molecules was also proven to modify surface states in some cases [62–64]. In *conclusions and perspectives* (page 107) we will present a brief outlook on the Ferrocene/Cu(111) system, where an interface state exists on monolayers of Ferrocene, originating from the Shockley surface state.

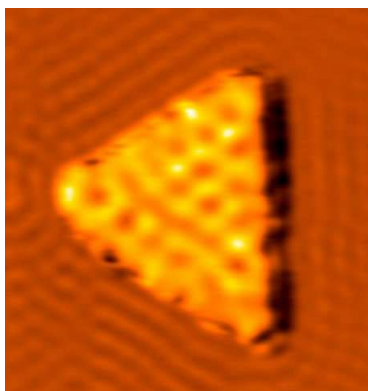


Figure 2.4: Standing wave pattern of the Shockley surface state on Cu(111) due to scattering at a cobalt nanoisland ($21 \times 22 \text{ nm}^2$, dI/dV map at 200 mV, gap conditions: 5.0 nA, 200 mV). On top of the island a standing wave pattern of a different wavelength is visible, which originates from the majority surface states of the island (*cf.* chapter 2.2).

2.2 Cobalt nanoislands on Cu(111) - a magnetic (111) surface

The epitaxial growth of Cobalt on Cu(111) and the resulting electronic and magnetic properties have been the subject of numerous studies since the early nineties [4, 5, 65–69], and still yield fascinating results [6, 7, 70]. For STM/STS studies, the Co/Cu(111) system is of particular interest due to several reasons. Firstly, in the low coverage regime, the system has a perpendicular magnetic anisotropy [71], leading to an out-of-plane magnetization at LHe temperature, which was, by SP-STM, first evidenced by Pietzsch *et al.* Secondly, due to the island growth mode at low cobalt coverage, surfaces of opposite magnetization can be accessed simultaneously with the STM tip, which is important for the comparability and reliability of the SP-STM data. Furthermore, their size in the nanometer range makes them suitable hosts for magnetic and nonmagnetic adsorbates. We will use this particular property later in this work for single atoms (*cf.* chapter 3) and molecules (*cf.* chapters 4 and 5). Before focusing on their SP properties, it is first necessary to understand the electronic structure of the islands in detail. In the following, we focus on how the electronic properties of the islands are influenced by structural details, as size and stacking, which in turn depend on the growth process.



Figure 2.5: Two-monolayer-high cobalt nanoislands of different size and stacking on Cu(111) grown at room temperature (size: $80 \times 70 \text{ nm}^2$, gap conditions: 0.03 nA, 0.80 V).

2.2.1 Cobalt growth on Cu(111)

When depositing cobalt onto Cu(111) at low temperatures in the submonolayer regime, dendritic shaped islands are formed [67, 70]. The adatom diffusion along the edges of nucleated islands as well as the hopping between different layers is reduced due to the small thermal energy of the adatoms compared to the diffusion barriers. Hence, irregular shaped islands are achieved. With increasing temperature, the diffusion is enhanced and the island shape is getting more and more regular. Finally, when depositing cobalt at room temperature, two-monolayer-high compact islands of triangular shape are formed (see Fig. 2.5) [65, 67, 70]. The energy of the adatoms is large enough to overcome the diffusion barriers and allows for all different kinds of diffusion. The actual shape of the islands is then determined by the total energy of the resulting system as well as by the ratio between competing diffusion steps [72].

As schematically shown in Fig. 2.6, due to the substrate symmetry, the islands possess two types of closed packed edges, namely $\{100\}$ -faceted edges (labeled A in Fig. 2.6) and $\{111\}$ -faceted edges (labeled B in Fig. 2.6). In the early stage of growth the shape of the island is determined by an anisotropic corner diffusion [70]. As presented in Fig. 2.6a for edge A, the barriers for the diffusion along A and from A to B are close in energy and so the corner diffusion from A to B is operative. On the contrary the diffusion barrier for the transition from B to A is much higher than the one for diffusion along B. So the mass transport from B to A is limited and $\{100\}$ edges are growing at the expense of $\{111\}$ edges resulting in triangular shaped

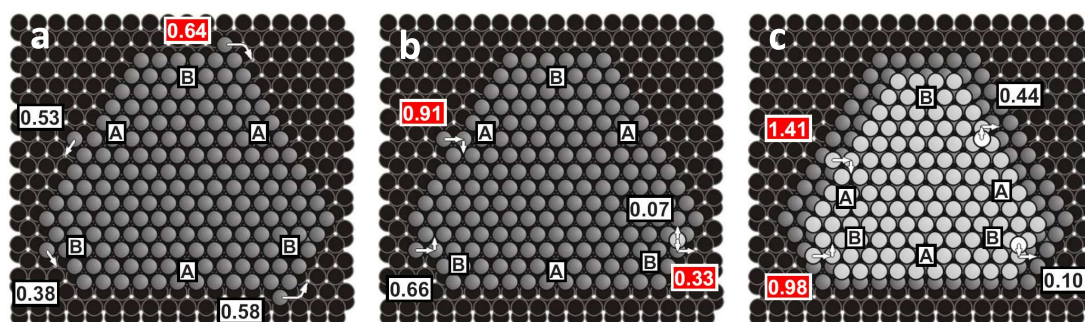


Figure 2.6: Calculated diffusion barriers for the adatom diffusion along the island edges and corners (a) and for the hopping between the substrate and the first cobalt layer (b), respectively first and second cobalt layer (c) [Cu: black, Co: grey]. The barrier (in eV) for operative (suppressed) diffusion steps is indicated in white (red) squares. Figure adapted from Ref. [70].

islands. While the shape is determined by the mass transport from one edge to the other, the height of the islands is a result of the interlayer diffusion although both processes take place at the same time. As the upward diffusion onto the first cobalt layer is favored compared to the downward diffusion towards the surface, a net mass transport onto the first layer takes place (see Fig. 2.6b). Thus a second cobalt layer is formed. Chado *et al.* could show for the closely related system of cobalt islands on Au(111) that, above a size of 20 atoms, bilayer islands are energetically more stable than monolayer islands [73]. A third layer formation is unfavorable because the downward hopping barrier for edge B is roughly ten times smaller than the one for the upward hopping (see Fig. 2.6c).

During the nucleation process of the islands, cobalt atoms can either occupy *hcp* or *fcc* hollow sites of the (111) surface, giving rise to two different island orientations on the surface. The complex interplay of the different diffusion barriers and two possible nucleation sites lead to the well-known triangular-shaped, two-monolayer-high islands of cobalt with two distinct orientations on Cu(111) in the sub-monolayer regime as visualized by means of STM topography in Fig. 2.5.

When further increasing the temperature during cobalt deposition, *i.e.* at temperatures above 300 K, intermixing of cobalt with copper appears [67, 74, 75]. This is associated with incorporation of Co atoms into the surface as well as with the appearance of mixed cobalt/copper islands and of vacancy islands in the copper surface. During the experimental work of this thesis care was taken to prevent any intermixing by carefully monitoring the temperature during deposition and immediately cooling down the sample to 4.6 K after deposition.

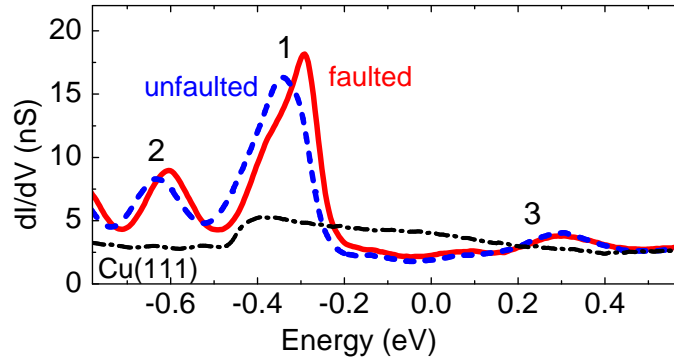


Figure 2.7: dI/dV spectra acquired over Cu(111), faulted and unfaulted cobalt islands, respectively. Feedback opened at 1.5 nA and 0.6 V. Island spectra are averaged over 60 spectra acquired on distinct 12 nm islands. Labels 1 to 3 indicate the three dominant d -like resonances near E_F .

2.2.2 Spin-polarized surface states of cobalt nanoislands

The electronic structure of the nanoislands has been extensively investigated by STS [4–7] due to the delicate interplay between their structure, which is influenced by the underlying copper, and the resulting electronic and spin-polarized properties. Typical spectra are shown in Fig. 2.7. Around E_F the dI/dV is dominated by three distinct peaks, labeled 1, 2 and 3 in Fig. 2.7. The two occupied peaks fall at biases of roughly -0.3 V (in the following called P1) and -0.6 V (P2), the unoccupied peak falling at 0.3 V (P3). The difference between spectra from faulted and unfaulted islands will be treated in section 2.2.3. The line shape of the different peaks is tip dependent, but while P2 shows significant changes from one tip to another, P1 and P3 present just minor changes. Given the asymmetric line shape of the peaks, the peak position is defined as the center of gravity of the line.

Ab initio calculations from the Patrick Bruno and Valeri Stepanyuk group from the MPI in Halle provide some insight into the island local density of states (LDOS), revealing in particular the origin of the peaks. In the first step of these calculations, the fully relaxed atomic configuration of the islands was determined by means of *ab initio* fitted many-body potentials formulated in the second moment approximation of the tight-binding theory as described in Ref. [9, 34, 35, 76]. In the second step, the LDOS was calculated using the Korringa-Kohn-Rostocker (KKR) Green’s function method based on density functional theory (DFT), employing the full potential approximation [5, 9, 77–79]. The islands were modeled as an infinite cobalt bilayer on a copper slab, using the interatomic distances calculated in step one. By extracting

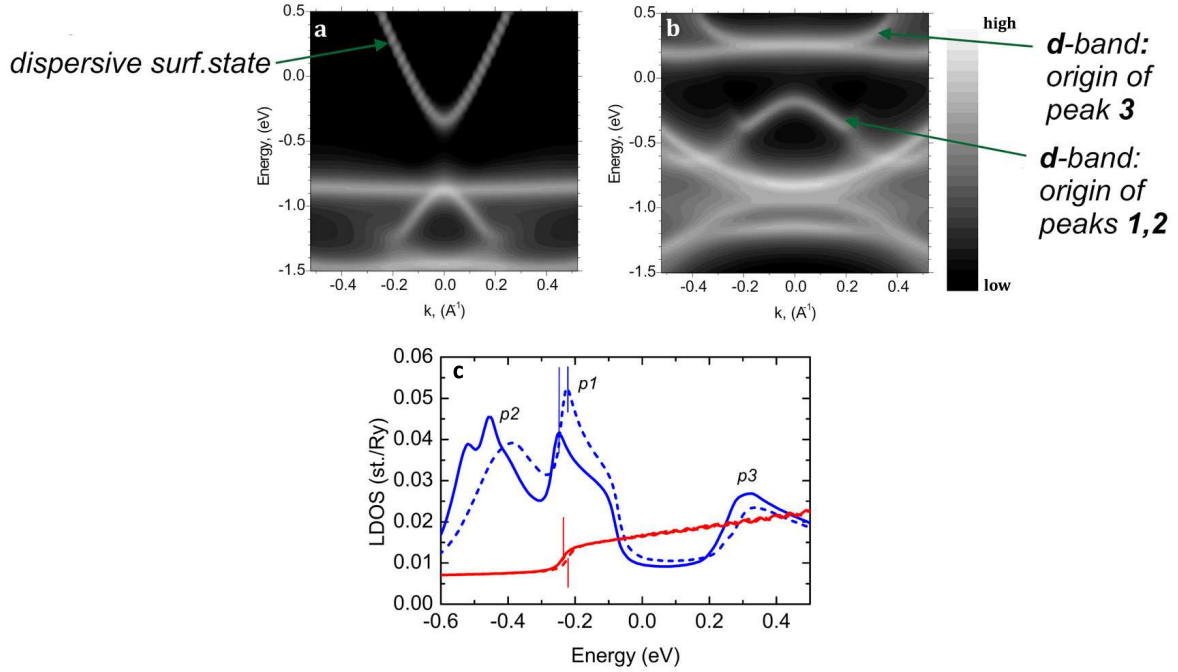


Figure 2.8: Calculated Spectral Density Maps of the topmost cobalt layer by DFT for majority (a) and minority (b) bands. c) Spin-polarized LDOS calculated by means of the KKR Green's function method in the 2nd vacuum layer above a unfaulted (solid lines) and faulted (dashed lines) infinite Co-bilayer on Cu(111). Minority spin states are in blue, whereas majority states are in red.

the imaginary part of the momentum-resolved energy-dependent Green's function one can plot Spectral Density Maps as done for the upper cobalt layer in Fig. 2.8.

From Figure 2.8b it can be deduced that all peaks originate from minority bands. P1 and P2 arise from the same minority $d_{3z^2-r^2}$ band that is hybridized and split at the intersection with the Cu(111) bulk band. While P1 originates from a hybridization of $s-p$ states with the minority $d_{3z^2-r^2}$ band that is situated in the projected bulk band gap, P2 is caused by an overlap of the minority cobalt d band with copper bulk states. The unoccupied cobalt minority d band finally leads to P3 [9]. As all peaks are close to the Γ point, they contribute to the tunneling current. While d -like bands dominated the minority structure around E_F , the majority structure is dominated by a dispersive $s-p$ band (see Fig. 2.8a).

To improve the comparison with the experiment, the SP local density of states in the second vacuum layer has been calculated (see Fig. 2.8c). The minority spectrum (blue lines) clearly

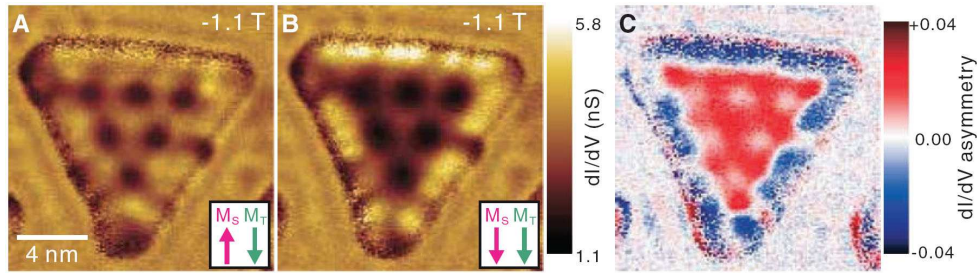


Figure 2.9: dI/dV (A and B), and dI/dV asymmetry (C), maps of the same Co island. The dI/dV maps were recorded at a sample bias of $+0.03$ V and a magnetic field of -1.1 T, but with different magnetization configurations between the magnetic tunneling tip and the Co island: antiparallel (A) and parallel (B). The insets represent the antiparallel (AP) and parallel (P) configurations. Feedback loop opened at $+0.5$ V and 1.0 nA. (C) dI/dV asymmetry map calculated from the images in (A) and (B) $[(A-B)/(A+B)]$. Figure adapted from Ref. [80].

exhibits the three dominant features also observed in STS (*cf.* Fig. 2.7). The majority states (red lines) are characterized by the onset of the dispersive surface state and otherwise featureless. This recalls the situation for the clean Cu(111) surface where the spectrum is dominated by the Shockley surface states (*cf.* Fig. 2.2c). The onset of this majority surface band falls roughly at the same energy as the minority P1 feature. Hence, in STS measurements, this majority feature of the spectrum is buried under this peak. Nevertheless it can be evidenced by STM/STS through dI/dV maps at energies above the onset of the dispersive surface state as presented in Fig. 2.4 and shown in reference [5]. A dI/dV map consists in measuring the differential conductance at a given bias for each pixel of the STM image. By doing so, the standing wave pattern of the surface state electrons at the island edges is visualized, and its k -dependence determined by varying the energy, *i.e.* the applied bias. The effective electron mass was found to be $m^* = 0.38 m_e$, which is the same effective mass as found for the Shockley surface states on Cu(111) (see section 2.1.2), and the bottom of the band was estimated at -0.2 eV or at lower energies [5, 7]. As the dispersive majority state is confined and the minority LDOS is constant over the island, the polarization above the island presents a spatial variation [7, 81], a visualization of this variation being recently provided by Oka *et al.* (see Figure 2.9) [80].⁴

⁴To obtain these so called dI/dV asymmetry maps, SP dI/dV maps of a Co island were acquired, once with a parallel and once with an antiparallel magnetization with respect to the magnetic tip. The switching of the island magnetization was done by means of an external magnetic field. Then the difference of the signal intensity at each pixel was calculated and divided by the sum of the intensities, the resulting image defined as asymmetry map, which provides the spatial variation of the polarization above the island.

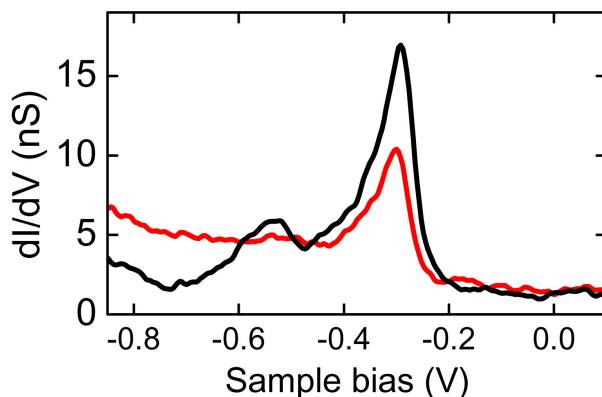


Figure 2.10: Spin-polarized dI/dV spectra acquired above two Co nanoislands on Cu(111). The islands have the same size and the same stacking, but opposite magnetizations (feedback opened at 0.50 nA, 0.60 V).

As shown above by calculations, cobalt nanoislands on copper possess a strongly spin-polarized electronic structure below E_F , which can also be evidenced by SP–STS as presented here in Fig. 2.10. By means of an SP tip, dI/dV spectra were acquired above two distinct islands. While the two spectra look quite similar in shape, the intensities of different spectral features differ significantly. At positive bias, the two spectra present the same intensity, but for negative bias this is no longer true. While for the black spectrum P1 is roughly 50 % more intense compared to the red one, at biases below -0.6 V the red spectrum becomes more intense. This determines unambiguously that the out-of-plane magnetizations of the two islands are opposite [7].

This spin-polarized nature of the cobalt islands was evidenced and exploited by SP–STM studies [6–9]. In fact, the accessibility of electronically equal surfaces with opposite magnetization in nanometer distances, combined with a size suitable for hosting single adsorbates, make this system very appealing for this technique. Nevertheless care has to be taken when comparing the SP signal of different islands as structural details like stacking [6], or size may influence the electronic structure and may "pollute" the SP signal. Thus, in the following section, a more detailed analysis of the interplay between structural and electronic properties will be carried out.

2.2.3 Changing the band structure - influence of the interatomic distances

As mentioned above, cobalt islands have two different orientations on the surface due to a different stacking of the cobalt layers with respect to the fcc stacking of the (111) surface. The islands continuing perfectly the fcc stacking are referred to as *unfaulted*, those presenting a stacking fault at the interface with copper are called *faulted*. This structural difference affects the electronic structure of the islands. This can be evidenced by STS [5,6]. Figure 2.7 presents averaged spectra acquired over the center of a faulted and an unfaulted island, respectively, both with an edge of 12 nm. For the unfaulted island, P1 falls at a bias of -0.31 V, while, for the faulted one, it shifts towards higher biases of 0.28 V. P2 is found at -0.64 V (unfaulted) and -0.60 V (faulted), respectively, and P3, finally, falls at $+0.3$ V for both types of islands (in good agreement with Ref. [6]). Comparable peak shifts are found by calculations (see Fig. 2.8c). Furthermore the DFT calculations show that the onset of the majority $s-p$ band shifts as well with stacking, which influences also the coupling of adatoms to the surface electronic states, this being explored in chapter 3.

Along with stacking, size can also influence the electronic structure of the island. To exemplify this, we present in Figure 2.11 a series of dI/dV spectra, which were acquired above unfaulted islands of different size employing the same tip for all islands. Although the same spectrum is observed for all the islands, the positions of P1 and P2 differ. While the island size decreases from 22.5 nm to 4.8 nm, P1 shifts from -0.31 V to -0.40 V. A similar behavior is found for P2, which also shifts downwards in energy with decreasing island size. Contrary to the first two, P3 does not change its energetic position. We performed the same experiment for faulted islands resulting in qualitatively similar results (see Ref. [82]).

To quantitatively analyze this behavior, spectra were taken above the center of 230 faulted and unfaulted islands employing a variety of different W-tips (see Fig. 2.12). The island size ranges from 4.8 to 31.9 nm for unfaulted, and 6.7 to 32.9 nm for faulted islands, respectively. The peak position has been determined for each island and binned by steps of 0.5 nm. For unfaulted islands, a monotonic shift over 0.09 V is observed reaching -0.31 V for the largest islands. For faulted islands a comparable trend is evidenced, although presenting minor differences. While for the smallest islands, the increase in energy with island size is more pronounced as for unfaulted islands, *i.e.* steeper, an asymptotic convergence towards -0.28 V is found for islands larger than roughly 13 nm. The slightly different behavior of faulted and unfaulted

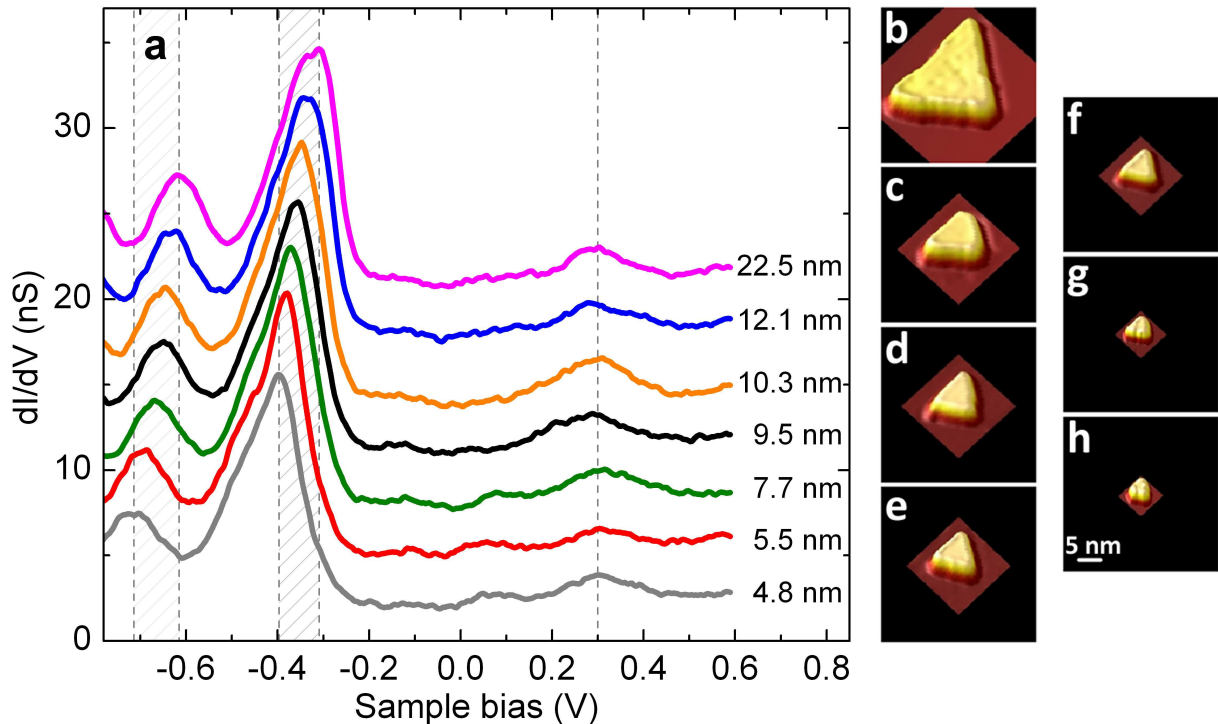


Figure 2.11: dI/dV spectra (a) on unfaulted nanoislands of increasing size and corresponding topographic images [(b) to (h)] [9]. Feedback opened at 1.5 nA, 0.6 V. Spectra over the islands with edge sizes of 5.5, 7.7, 9.5, 10.3, 12.1, 22.5 nm are vertically shifted upward by 3, 6, 9, 12, 16, 19 nS, respectively. The hatched areas delimit the range over which an energy shift is observed for P1 and P2 in these spectra. The dashed line is positioned at P3.

islands remains still unclear. An asymptotic saturation for the unfaulted islands might set in for larger sizes, which were not explored here, as the probability to find islands larger than 30 nm is very low. However, taking into account that for P2 similar curves as for P1 can be obtained, in general one can state the simple rule: The larger the island, the higher the energy of Peak 1 and 2.

Still, there is the possibility of an influence of the edges of the islands on the electronic structure. Hence position dependent studies have been carried out. Fig. 2.13a shows selected dI/dV spectra acquired on different positions above a faulted island of 7.1 nm edge size. The tip was moved along a line reaching from a corner of the island to the opposite edge as depicted in the inset of Fig. 2.13c. The corresponding profile of the island along this line is shown in Fig. 2.13c and the different tip positions during the spectra acquisition are indicated. The tip

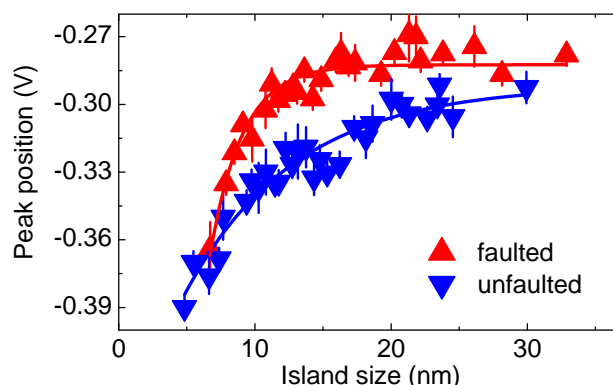


Figure 2.12: The position of P1 versus the island size for faulted (red) and unfaulted (blue) islands (solid lines are added as a guide to the eye). The data are binned by steps of 0.5 nm. For unfaulted islands a monotonic increase of the energy with the island size is observed. For faulted islands, the increase is steeper but saturates asymptotically for sizes larger than 13 nm.

employed in this study differs from the one of Figure 2.11 and P2 is not resolved here. As stated above, the structure of this peak is strongly tip-dependent.

Examining the spectra in Fig. 2.13a as a function of the tip position two effects become evident: a change in the energetic position of P1 and a change of its intensity. Starting in the center region of the island (spectra 5 – 7) for all spectra we find the peak at an unchanged position of approximately -0.36 V with a constant intensity, the low energy being due to the small island size as evidenced above. When approaching the corner the peak shifts to lower energies and decreases in intensity (spectra 4 and 3). Close to the corner it almost vanishes (spectrum 2) and finally disappears completely at the corner (spectrum 1). A similar behavior is observed when approaching the edge, the only difference being that this behavior sets in much faster, *i.e.* within a shorter distance (spectra 8 and 9).

For a more precise picture, the peak energy has been determined for all spectra and drawn versus the tip displacement in Fig. 2.13b. The lateral displacement corresponds to the displacement along the island profile shown in the inset of Figure 2.13c. A plateau of constant peak energy with a diameter $d \geq 1$ nm is discernible around the center of the island. However, beyond this plateau, a downward energy displacement of the peak is evidenced. At a distance of ≈ 2.5 nm from the corner, a shift sets in and increases while approaching the corner. The final and still detectable peak position is 0.05 V lower than the one in the central region. For the edges a similar behavior is observed. Nevertheless, here the zone in which the shift occurs is reduced to approximately 1 nm in the vicinity of the edge. Therefore it becomes more difficult

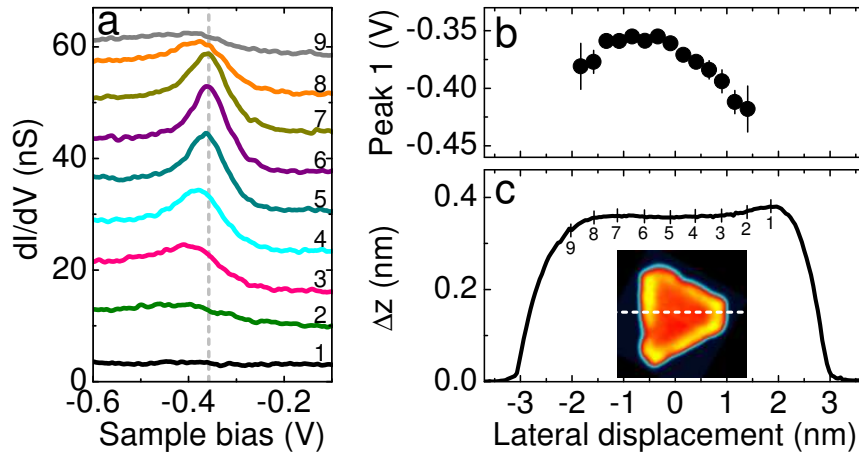


Figure 2.13: Study of the relation between peak position and tip position above the island. a) dI/dV spectra acquired across a faulted 7.1 nm nanoisland (1.0 nA, 0.5 V, spectra 2 – 9 shifted vertically by steps of 7 nS). The dashed line is centered on the peak positions of spectra acquired in the island center (spectra 5 – 7). b) Energy shift of P1. c) Line profile across the island (from corner to edge as depicted by the dashed line on the inset). Number 1 to 9 corresponds to the position where the spectra labeled 1 to 9 on panel (a) were acquired.

to correctly determine the peak displacement. A value of roughly -0.03 V was found, similar results being obtained for different faulted and unfaulted islands. An earlier study by Pietzsch *et al.* [7] evidenced the attenuation of P1 at the edge but did not evaluate any peak shift. Even the smallest islands studied provide a plateau of 1 nm diameter of constant electronic structure around the center of gravity, this structure, however, depending on the island size. Hence edge and corner effects are negligible for the size-dependent study above as care was taken to always position the tip close to the center of the nanoisland.

In order to support the experimental results and gain some insight into the origin of the observed phenomena, the theoretical calculations presented above (*c.f.* section 2.2.2), have been extended to islands of various sizes. Instead of computing just the relaxed configuration and LDOS of one island, a whole set of calculations was carried out for unfaulted islands with a size ranging from 4 to 30 nm. In a first step, the fully relaxed island configuration was determined as a function of island size. The relaxed in- and out-of-plan Co-Co bond length can then be extracted. These parameters were used in a second set of calculations as input parameters for infinite Co-bilayers on Cu(111). These then mimic different sized islands in the KKR Green's function approach and a link can be established between the Co-Co distance and the energy shift of the electronic structure. A summary of the theoretical results is given in

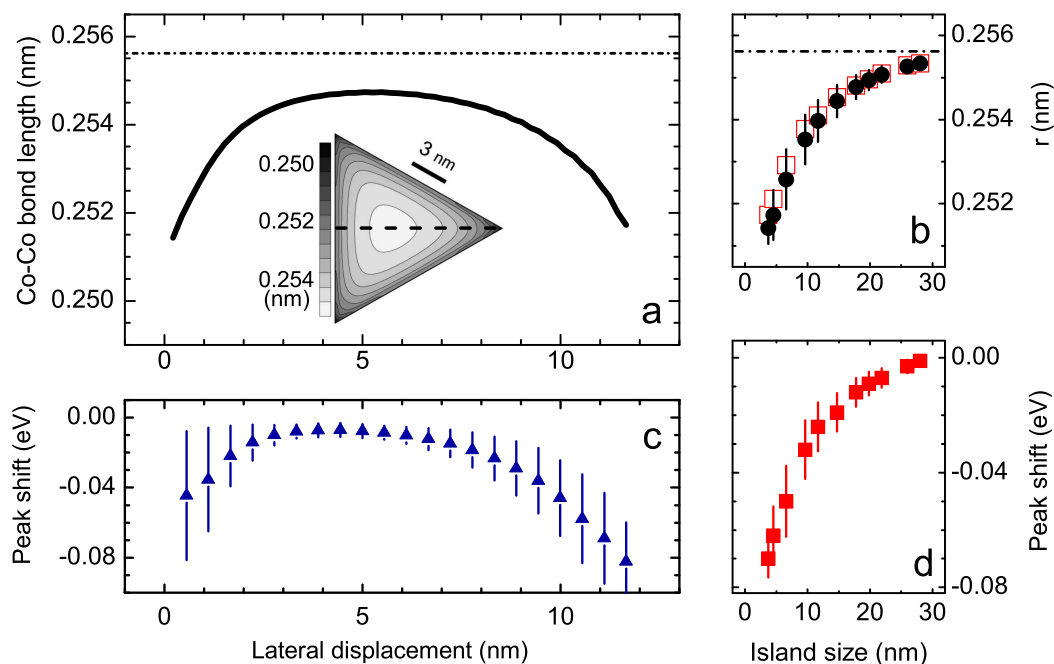


Figure 2.14: a) In-plane bond length of the top Co layer across a 15 nm island (from corner to edge as depicted by the dashed line on the spatial distribution of in-plane Co-Co bonds in the inset). Dash-dot line: ideal bulk Cu bond. c) Predicted peak energy of P1 across the island along the same line as in (a). b) Average-bond length r , described in the text, for the top (solid circles) and bottom (open squares) Co layers, and, d) Corresponding energy shift for calculated P1 with increasing size.

Fig. 2.14.

Figure 2.14a presents the in-plane Co-Co bond length of the top layer of a 15 nm island as a function of the position. In the inset, the regions with the same bond length have the same greyscale: the brighter the region, the larger is the interatomic distance. In the center of the island an area of several square nanometers with a constant bond length is found. Here the interatomic distance is largest. Figure 2.14a shows the bond length as a function of the lateral displacement when following the dashed line in the inset. At the edge (left side) and at the corner (right), the interatomic distance is below 0.252 nm. Approaching the island center it increases rapidly and saturates, leading to a plateau of constant bond length larger than 0.254 nm. An

average bond length r and an interlayer distance z can be determined for the central region. This was done for all different sized islands. A dependency of both r and z on the island size is predicted (Fig. 2.14b). While small islands provide the shortest interatomic distances close to the Co bulk value, r increases with increasing island size and approaches asymptotically the Cu bulk value of $r_0 = 0.2556$ nm. The substrate-island mismatch $(r_0 - r)/r_0$ varies from almost 2%, which is the macroscopic mismatch, to 0.1% for the large islands. At the same time, z decreases about 1% with increasing island size.

In order to evidence how these changes in the atomic configuration impact the band structure, the so-obtained sets of r and z have been used to fix the Co-Co bond length and the interlayer distance of infinite Co bilayers on Cu(111). Thereby a dependency of the energetic position of P1 and P2 on r and z could be established (see Fig. 2.14d). In good agreement with the experimental results, the calculated P1 shifts downwards in energy by about 0.07 eV when changing the island size from 30 to 4 nm. A comparable energy variation is found for P2 (not shown here).

In a last computational approach the peak position on different spots of the islands has been explored. Fig. 2.14c shows the energy of P1 versus the lateral displacement (same as in Fig. 2.14a). Once again there is a central region of more or less constant peak energy as was observed by experiment (*cf.* Fig. 2.13b). Approaching the edge or corner P1 shifts down by 0.03 and 0.06 eV, respectively, in agreement with experiment (*cf.* Fig. 2.13). Thus the bond-length variation within the island is sufficient to explain the resulting peak shift, and other effects, which occur at the edges and might influence the LDOS, *e.g.* the redistribution of the electron density due to the Smoluchowski effect [83], play no, or at most, a minor role.

Given the theoretical approach, in which the only altered input parameter was a change of the interatomic distances depending on the island size, the calculations evidence that the peak shifts observed for P1 and P2 in experiment are due to a change of the interatomic configuration, which is a function of the island size as well as of the position above the island.

The interatomic distances, *i.e.* the bond length in nanoislands on a surface are determined by a competition between the substrate lattice and the island contact layer. If the lattice constant of the substrate and the ideal atomic distances of the island differ, the atoms tend to adopt the substrate lattice introducing then strain within the island. The influence of the substrate is different for the center of the island compared to the edges or corners and leads to an inhomogeneous bond-length distribution, which also changes with island size. These relaxation processes due to a lattice mismatch are called mesoscopic relaxation, and proved

here experimentally to alter the electronic structure as predicted before by theory [34, 35]. Recently, a study on Co islands on Cu(001) also evidenced a mesoscopic relaxation through surface X-ray diffraction [84].

Our results are in line with experimental findings on the electronic structure of Co nanoislands on different (111) surfaces, like Au(111) [85], Pt(111) [86], and of cobalt thin films [87]. These systems possess peaks similar to P1. Table 2.1 provides the energetic position E of these peaks and the macroscopic mismatch M , which is defined as $M = (r_{sub} - r_{Co})/r_{sub}$, r_{sub} and r_{Co} being the bulk bond length of the substrate and of cobalt, respectively. A well-marked trend is observed: the larger the mismatch between substrate and cobalt, the higher in energy the peak. The mismatch with the substrate induces strain on the Co islands, which pulls the Co atoms apart (the substrate lattice constant being larger than the one of Co) and enlarges the interatomic distances. So, the larger the mismatch, the larger is also the Co-Co bond length, which in turn shifts the peak towards higher energies. This is what was observed above for the Co islands of different size on copper.

Insight into the mechanism behind the observed peak shift can be gained within the framework of a tight-binding model. For an infinite cobalt bilayer we can express the energy shift ΔE of the band as a function of the Co-Co bond length r as follows:

$$\Delta E(\vec{k}, r) = \beta(r) F(\vec{k}, r).$$

The function $F(\vec{k}, r)$ is a positive sum of k -dependent cosine functions with $\|\vec{k}\| < \pi/2r$. As proposed by Friedel [88], we write the transfer integral as $\beta = \beta_0 \exp(-qr)$, q being a positive material-dependent constant, and neglect the crystal field contribution. For occupied electronic states the transfer integral is negative ($\beta_0 < 0$). And in the limit of a small variation of the average bond length ($r = r_0 - \delta r$) as it is the case in our study (see Figs. 2.14a and 2.14b), the band shift becomes proportional to the bond length, *i.e.* $\Delta E \propto (1 + q \delta r) \beta_0$. Based on this

Table 2.1: Peak energy E corresponding to the dominant peak position of unfaulted Co nanoislands as a function of the macroscopic mismatch M with the underlying substrate.

	Au(111)	Pt(111)	Cu(111)	Co(film)
M (%)	13	9	2	0
E (eV)	-0.15 Ref. [85]	-0.23 Ref. [86]	-0.31	-0.43 Ref. [87]

relation, P1 and P2 exhibit a similar negative shift, which varies linearly with the Co-Co bond length in agreement with Figures 2.14b and 2.14d. The two peaks possess the same shift as they originate from the same occupied $d_{3z^2-r^2}$ band, i.e. they have the same negative transfer integral β_0 . For P3 the situation is different. This peak has its origin in the unoccupied minority d band, which is relatively flat around the Γ -point and therefore has a narrow bandwidth, i.e. $\beta_0 \approx 0$. Thus a negligible band shift is expected for P3, which is in agreement with the experiment where no cognizable energy variation of this peak was detected.

Summary and conclusions

In the first part of this chapter, the DOS in the vicinity of E_F of the Cu(111) surface was presented and shown to have a strong contribution of a Shockley surface state appearing in the projected bulk band gap. Compared to copper, the bilayer cobalt islands grown on Cu(111) host a more complex LDOS, which is spin-polarized. By means of STS experiments and DFT calculations we established a direct relation between the d -like resonances of the island LDOS and the size of the cobalt islands. These results constitute the first experimental observation of "mesoscopic" relaxation [34, 35]. They show that the surface electron states may act as a sensitive probe for the local atomic configuration of nano-objects. By changes in size or shape one may modify the electronic and chemical properties.

A consequence of our findings can be seen in the spin-polarized dI/dV map in Fig. 2.15. Four cobalt islands of different sizes and stacking are presented, all showing different contrasts. The contrast is determined by the intensity of the dI/dV signal. On the one hand this intensity depends on the amplitude of the d resonance, which in turn is a function of on the magnetization direction (cf. Fig. 2.10), and on the other hand it depends on the energetic position of the resonance, which shifts depending on the size or the stacking of the island. So differences in contrast can either be due to one of these parameters, or due to a mixture of these. As the two faulted islands in the map are of the same size and stacking, the observed contrast difference can be unambiguously assigned to an opposite magnetization. However the unfaulted islands have different sizes, so the contrast between the two unfaulted islands is either due to the size difference or due to a mixture of size and polarization effects, the origin being ambiguous. When comparing the faulted with the unfaulted islands, the contrast originates from a mixture of the stacking and the size effect and, maybe, a spin-polarization effect, an unambiguous correlation

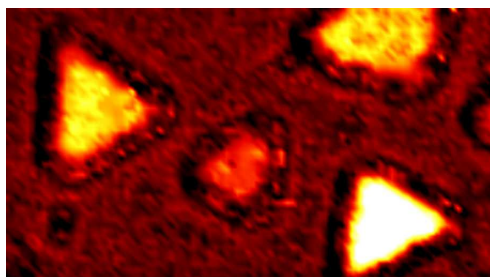


Figure 2.15: Spin-polarized dI/dV map of cobalt nanoislands on Cu(111) at -405 mV (37×20 nm², feedback opened at 300 mV and 0.10 nA). Due to the crystal symmetry and its orientation, here faulted islands point with one corner to the right, while unfaulted islands point to the left.

again being impossible. This exemplifies the importance of a careful choice of the island size and stacking, when studying SP properties, as otherwise electronic effects may interfere with SP effects. Studying adsorbates on cobalt islands, care has to be taken to work with islands of the same stacking and same size. Then SP properties may be explored as was done in chapter 3, where adatoms on cobalt islands are investigated, or in chapter 4, where we study electronic states of organic molecules adsorbed on these islands.

CHAPTER 3

Electronic states above an adatom on a magnetic surface¹

In recent years subtle interactions of adatoms with crystalline surfaces have been evidenced by STM/STS. Due to the spatial resolution of the STM direct access to the adatom as well as to the surface is possible at the same time. This, in turn, facilitates the investigation of a vast variety of adatom related phenomena like the localization of surface states [51, 52, 89–93], magnetic effects [8, 94–98], like the Kondo effect [89, 98–106] or even the surface electron confinement in quantum corrals [53, 107], *i.e.* artificially modeled adatom structures. Here we focus on the interaction of transition metal adatoms with the surface electron states of cobalt islands on Cu(111). The cobalt islands on the (111) surface of copper turned out to be ideal hosts for atom adsorption. The SP nature of the adatoms can be identified, since the band structure of the nanoislands is well studied and understood (see section 2.2 for details). For spintronic applications, the spin-polarization, which can be written as:

$$P(E) = \frac{n_{\uparrow}(E) - n_{\downarrow}(E)}{n_{\uparrow}(E) + n_{\downarrow}(E)}, \quad (3.1)$$

where $n_{\uparrow}(E)$ and $n_{\downarrow}(E)$ stand for the majority and minority LDOS, respectively, is of special interest. Several contributions to $P(E)$ are evidenced and shown to be opposite in sign, namely the polarization of surface-induced states and of atomic resonances. Single adatoms on the Co surface will be shown here to act as spin filters.

¹This chapter presents results published in *Phys. Rev. B* **79** 113401 (2009)

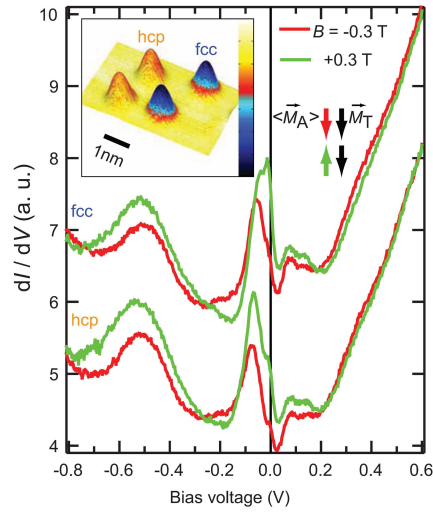


Figure 3.1: Spin-polarized dI/dV by means of an external magnetic field \vec{B} . Spectra of individual Co adatoms adsorbed on Pt(111) in hcp or fcc site, respectively. The time-averaged magnetization of the adatoms $\langle \vec{M}_A \rangle$ is aligned with \vec{B} , resulting in a change in the dI/dV curve depending on the relative orientation of $\langle \vec{M}_A \rangle$ and \vec{M}_T . The inset shows a topograph with the simultaneously recorded dI/dV map at -0.1 V. Figure adapted from Ref. [96].

The theoretical calculations presented in this chapter have been carried out by Pavel Ignatiev,² Valeri Stepanyuk² and Patrick Bruno^{2,3} in the framework of a publication [11].

3.1 Single atoms in spin-polarized STM experiments

Among the numerous STS/STM studies on adsorbed atom (adatom) systems published in recent years [51–53, 89–94, 98–105, 107], only very few employed spin-polarized STM/STS [8, 95–97]. Bergmann *et al.* evidenced spin-polarized standing waves with an anisotropic spatial distribution around oxygen atoms adsorbed on a Fe double layer on W(110) [95]. For the direct detection of a spin-polarized signal above individual adatoms, two distinct methods have successfully been employed [8, 96].

²Max-Planck-Institut für Mikrostrukturphysik, Halle

³Present address: European Synchrotron Radiation Facility, Grenoble

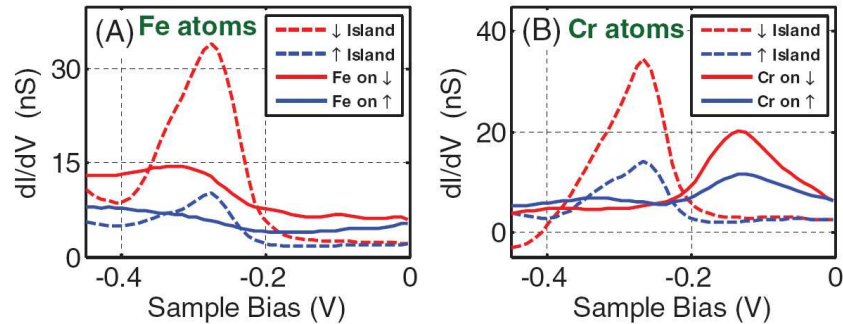


Figure 3.2: Averaged SP dI/dV spectra over two Co islands with opposite spin orientation (dashed lines, -0.025 eV, 3 pA), as well as over Fe (A) and Cr (B) adatoms residing on these two islands (solid lines, -0.05 eV, 2 pA). Figure adapted from Ref. [8].

External fields for SP-STM on single atoms

Meier *et al.* used cobalt adatoms on a Pt(111) substrate [96], which possess large effective magnetic moments of about 5 Bohr magnetons (μ_B) with a strong out-of-plane anisotropy [108], due to a spin-orbit coupling. If a magnetic field \vec{B} is applied either parallel or antiparallel to the tip magnetization, different SP dI/dV spectra are recorded as shown in Figure 3.1. Time-averaged magnetization curves of the individual cobalt atoms were measured, and the magnetic moment was shown to depend on the local environment. For a deeper insight in the role of the environment, one monolayer high Co nanowires were deposited onto the substrate prior to the adatom deposition, and the magnetization of adatoms was measured as a function of the distance to the magnetic Co nanowires. An oscillatory Ruderman-Kittel-Kasuya-Yosida (RKKY) interaction [109–111], between the Co nanowire and the adatoms in its vicinity was established. Recently, this study was extended to the RKKY exchange between the spins of individual Co adatoms on Pt(111), which was shown to be distance- and direction-dependent [97].

SP-STM on adatoms on magnetic surfaces

In contrast to these measurements, Yayan *et al.* stabilized the spins of the adatoms through the interaction with a ferromagnetic substrate, resulting in an SP contrast, which depends on the relative orientation of the substrate and tip magnetizations [8]. They used two cobalt nanoislands with opposite magnetization, and deposited Fe and Cr at low temperatures. The dI/dV spectra over the islands, which are acquired with a Cr-tip with an out-of-plane component

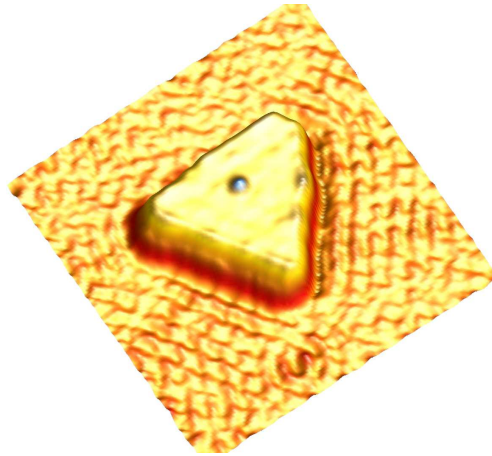


Figure 3.3: Constant-current STM image of a faulted cobalt nanoisland after the transfer of a Cu atom from the tip apex to its center ($24 \times 24 \text{ nm}^2$, 0.3 nA , -0.03 V). The scattering of Shockley surface-states produces the spatial oscillations on Cu(111).

of the magnetization, present different intensities as shown by the broken lines in Figure 3.2. The islands are defined as either "up" or "down", which is marked in the figure with arrows pointing up or down, respectively, since the change in intensity can be traced back to two islands possessing opposite magnetization. For both types of adatoms, the spin-polarized dI/dV spectra, which are shown as full lines in this figure, differ, depending on the magnetization of the island on which the atom is adsorbed. An SP contrast is observed. While iron atoms show a stronger signal for an antiparallel configuration over the whole bias range investigated, the contrast above chromium atoms is inverted at $\approx -0.2 \text{ V}$. For higher biases (between -0.2 V and E_F), the antiparallel configuration is dominant, but for lower biases (between -0.2 and -0.4 V), a small contrast, favoring the parallel configuration, is observed. Although a ferromagnetic and antiferromagnetic coupling is predicted for Fe and Cr atoms, respectively, the origin of the observed spin-contrast remained unclear.

In this chapter we present a further investigation of the LDOS above transition-metal adatoms in interaction with the SP surface states of cobalt islands by means of STS and DFT calculations to better understand the origin of the observed contrast. While Meier *et al.* focused on the magnetization of adatoms and the RKKY interactions, our main focus lies on the interplay between adatom and substrate states that determines the spin-polarized LDOS above the adatom. Surface-induced states as well as atomic resonances are found, which lead to changes in the sign of the spin-polarization above the atom.

3.2 Unveiling SP contributions to the LDOS above adatoms on cobalt islands

To go beyond the study of Yayan *et al.* and identify the different contributions to the LDOS, single magnetic (Co, Ni) and nonmagnetic (Cu) atoms residing on faulted and unfaulted islands were studied by STS, while *ab initio* calculations were performed for all these atoms as well as for Fe and Cr. Figure 3.3 shows a single copper adatom in the center of a nanoisland, which was transferred from the tip apex via a controlled tip-sample contact as described by Limot *et al.* [31]. To do so, the feedback loop is opened above the clean substrate and the tip is approached towards the surface until a tip-sample contact is achieved and a sudden change in the tunneling current is observed, which results in a conductance of roughly $1 G_0 = 2e^2/h$. Afterwards, in most cases STM topography confirms the presence of a single adatom left at the site where the tip was positioned prior to the approach. For the deposition of different elements, the coating material of the tip apex has to be chosen accordingly. We preferred this deposition method to standard evaporation techniques, because in this way isolated atoms could be deposited in a controlled manner in the center of the island. This allows ruling out artifacts like atom-atom interaction mediated by the surface states or inhomogeneous islands LDOS due to neighboring adatoms. To avoid edge effects, the adatom has always been placed near the center of the island. Single transition-metal adatoms appear as protrusions with an apparent height of approximately 0.1 nm depending on the applied bias and the atoms nature.

3.2.1 Differential conductance above adatoms on cobalt nanoislands

The dI/dV spectra of individual adatoms are shown together with the well-known island spectrum in Figure 3.4. The bias range is limited to values between -0.6 V and E_F , as for biases beyond this range the adatoms moved during the acquisition of the spectrum due to their high intrinsic mobility on this surface. The intensity of the signal above the adatoms is strongly attenuated with respect to the pure cobalt surface, as shown in Figure 3.4a for the case of a copper adatom,⁴ although it is valid for all studied elements. If we zoom-in on the intensity scale (see Fig. 3.4b), details of the acquired spectra of the magnetic (Co, Ni) and nonmagnetic (Cu) adatoms become visible. All spectra of adatoms residing on faulted islands have a com-

⁴The full black and the dashed red line correspond to the clear island and the copper adatom spectrum, respectively.

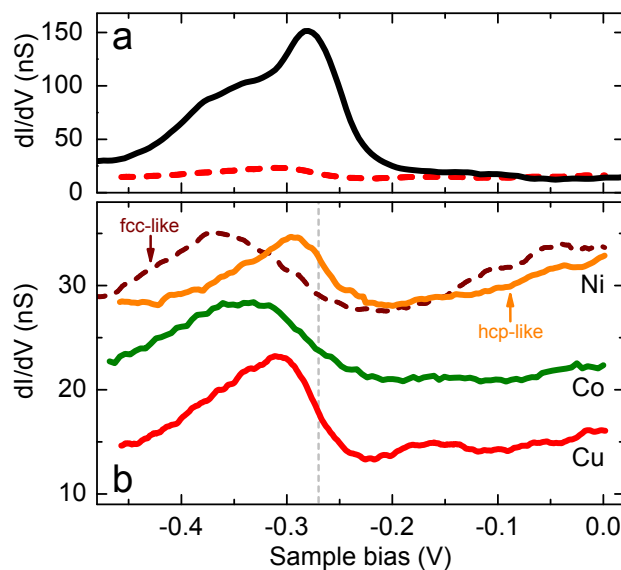


Figure 3.4: a) dI/dV over a Co nanoisland (solid line) and over a Cu atom adsorbed on a faulted (hcp) nanoisland (dashed line). Feedback opened at 0.4 nA, 0.03 V. b) dI/dV over Ni, Co and Cu atoms adsorbed near the center of a faulted cobalt nanoisland (feedback loop opened at 0.4 nA, 0.03 V.); the dashed curve is a dI/dV acquired over a Ni adatom of an unfaulted (fcc) island. The Ni and Co spectra are shifted vertically by 14 and 7 nS, respectively. All spectra are averaged over various atoms of same nature. The dashed line gives the approximate position of the majority $s - p$ surface-state onset.

mon resonance falling at -0.30 V. A similar resonance can be found in the spectra of iron in Fig. 3.2 [8]. On unfaulted islands the resonance falls at lower energies (as shown for the case of Ni in Fig. 3.4b). Although the line shape of the different spectra varies with the atom's nature, Ni in particular showing a marked upturn of the dI/dV towards E_F , the origin of this spectral feature seems rather surface-related than element specific.

This resembles the adsorption of transition-metal atoms on Cu(111) and Ag(111), where adatoms different in nature all produce a resonance at an energy close to the onset of the Shockley surface state [51, 52]. But the situation on the cobalt islands is more complicated compared to these coinage surfaces. In fact, the cobalt islands host a $s - p$ majority surface state with a 2D electron gas-like character, but additionally they possess d -like minority resonances (see section 2.2.2 on page 21 for details).

The dispersive majority $s - p$ state is similar to the Shockley surface state of Cu(111) and a similar interaction of an adatom with the dispersive $s - p$ states is expected for both

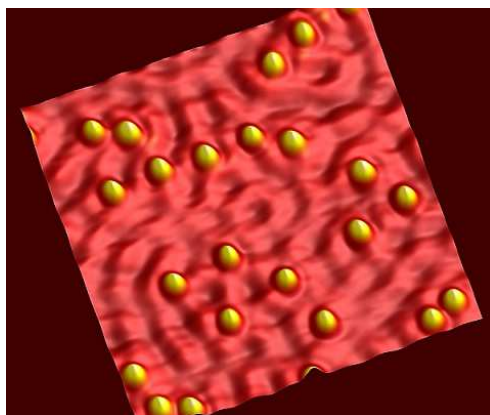


Figure 3.5: Copper adatoms on Cu(111). Standing waves of the Shockley surface-states due to a scattering at the atomic protrusions are visible ($20 \times 20 \text{ nm}^2$, 0.03 nA, 0.03 V).

systems. The common resonance over the adatoms in Fig. 3.4 could therefore be produced by a similar mechanism encountered for adatoms on Cu(111) or Ag(111). However, the minority surface resonances in the surface LDOS are expected to interfere as well. Before focusing on the adatoms on cobalt, we therefore present and explore the simpler case of copper, cobalt and nickel atoms adsorbed on Cu(111).

3.2.2 Localization of dispersive surface states by an adatom

Ni, Co and Cu atoms have been deposited onto the Cu(111) surface either by controlled tip-sample contacts, or by thermal evaporation at a temperature of 10 K, resulting in individual adatoms as shown for the case of copper atoms in Figure 3.5. In the topographic image a standing-wave pattern is clearly visible in between the atoms [53]. To explore the changes in the LDOS above the adatoms compared to the clean surface, spectra of the differential conductance were acquired, which are presented in Figure 3.6. Although slightly different in shape (see Fig. 3.6b), the spectra acquired above Ni, Co or Cu adatoms, respectively, present a common feature just below the onset of the surface state (*cf.* Fig. 3.6a, the onset is indicated with a dashed line in both figures). This is in good agreement with Ref. [52], who investigated Cu and Co adatoms on Cu(111), both giving rise to similar spectra.

In general, if an atom is adsorbed on a surface, three qualitatively different cases of adsorption may occur: ionic, neutral and metallic [114, 115], which follow respectively from a full electron charge transfer, no charge transfer, or a partial charge transfer between the surface

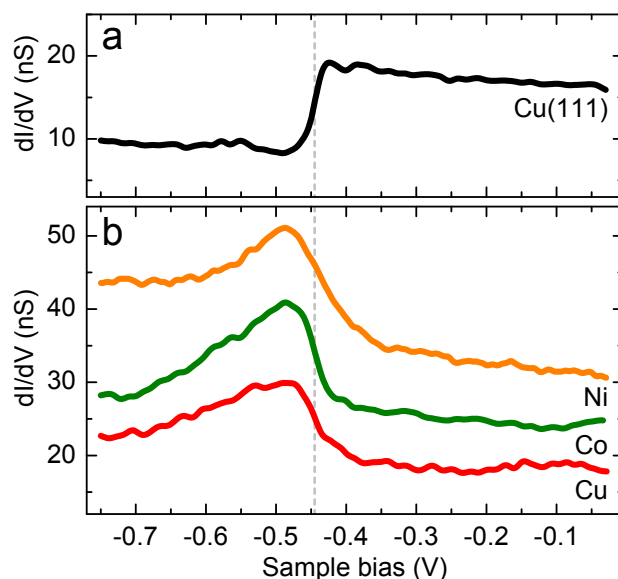


Figure 3.6: dI/dV spectra over the (111) surface of copper (a), and over Ni, Co and Cu adatoms on this surface (b). The Ni and Co spectra are shifted vertically by 14 and 7 nS, respectively. The dashed line is centered at the surface-state onset. All spectra are averaged over various atoms. Feedback opened at 0.5 nA, -0.03 V. Atomic-like resonances are also predicted for Ni in this energy range [112].

and the adatom. For the adsorption of transition metal atoms on a metal surface, we expect metallic adsorption. Upon adsorption an originally unperturbed adatom level ε_a is shifted and broadened through the interaction with the continuum of the substrate states as depicted in Figure 3.7 [113]. While widths of 1 – 2 V for s orbitals and width larger than 2 V for p orbitals have been predicted by Lang *et al.*, d resonances have been experimentally determined to be 0.1 V wide [101]. Therefore the experimentally observed resonances could only originate from d states, but not from s or p orbitals given the narrow width of 0.1 V for all types of atoms. However d -states should fall at different energies depending on the atom's nature, which is not the case here. Thus we expect the origin of the resonance to be rather related to the interaction of the adatom with the surface electronic structure.

As mentioned in chapter 2.1, the (111) surface of copper hosts 2DEG-like surface states. When placing a transition-metal atom onto this surface, its local positive potential acts on the 2DEG and leads to the appearance of a so-called bound state [116, 117], a localization of the surface states at the atom's site. By means of STM bound state-related features have been first observed by Kliewer *et al.* [118], for the case of manganese atoms on Ag(111), but only

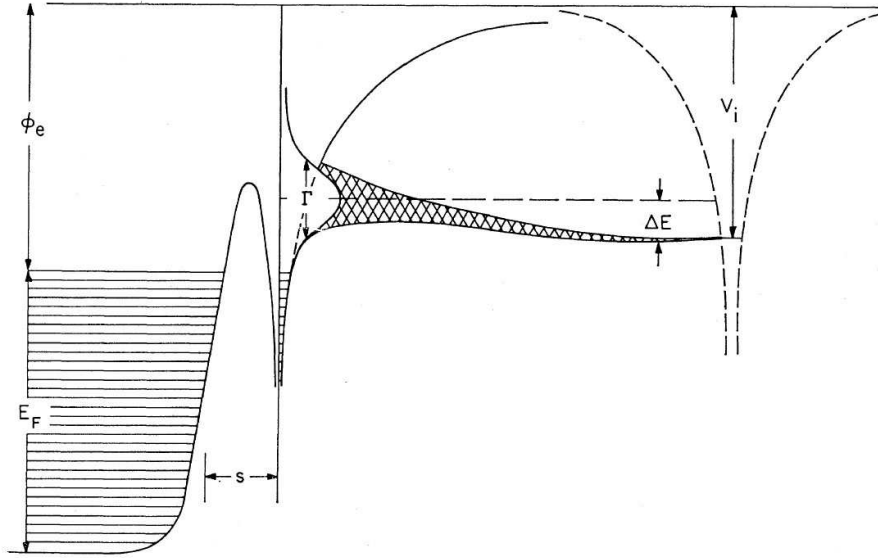


Figure 3.7: Energy-level diagram for the interaction of an adatom level ϵ_a with an electronic band of a metal substrate. The dashed curve is the ion-core potential for the atom at infinity. The solid curve is a scheme of the combined atomic and metal potential for the atom being at a distance s from the surface. V_i represents the ionization energy of the isolated atom, ΔE here presents the shift of the energy level (different in the following), and Γ is the natural broadening due to the atom's interaction with the solid. Figure adapted from Ref. [113].

later the existence of a surface bound state has been unambiguously established [51, 52].

3.2.3 Newns-Anderson model for surface impurities

Following Limot *et al.* [52], some insight into the appearance of a bound state is gained by means of an extended Newns-Anderson model [50, 119]. We express the Newns-Anderson Hamiltonian for the interaction of a single adsorbate level $|a\rangle$ with the bulk states $|\mathbf{q}\rangle$ and the surface states $|\mathbf{k}\rangle$ as follows:

$$\mathcal{H} = \begin{pmatrix} \varepsilon_a & V_{a\mathbf{q}} & \tilde{V}_{a\mathbf{k}} \\ \tilde{V}_{a\mathbf{q}}^* & \varepsilon_{\mathbf{q}} & 0 \\ \tilde{V}_{a\mathbf{k}}^* & 0 & \tilde{\varepsilon}_{\mathbf{k}} \end{pmatrix},$$

where ε_a is the eigenenergy of $|a\rangle$; the submatrices $\varepsilon_{\mathbf{q}}$ and $\tilde{\varepsilon}_{\mathbf{k}}$ contain the eigenenergies of the Bloch bulk and surface states, respectively; $V_{a\mathbf{q}}$ and $\tilde{V}_{a\mathbf{k}}$ are the coupling matrix elements between the adsorbate level and the bulk or surface states, respectively. For the transition-metal

atoms investigated, the adatom level $|a\rangle$ is a s orbital. Standard Green's function methods [120], lead to the following expression for the projected density of states at the adatom site:

$$n_a(E) = \frac{\pi^{-1} \Delta(E)}{[\varepsilon - \varepsilon_a - \Lambda(E)]^2 + \Delta^2(E)}. \quad (3.2)$$

The imaginary part of the self energy $\Delta(E)$ is the sum of contributions from the coupling of the adsorbate level to the bulk and surface states, respectively:

$$\Delta(E) = \Delta(E)_b + \Delta(E)_s.$$

$\Lambda(E)$, the real part of the self energy, follows from $\Delta(E)$ via a Hilbert transform. The bulk contribution can be assumed featureless and constant over the investigated energy range due to the bulk bandwidth:

$$\Delta(E)_b = \pi \sum_{\mathbf{q}} |V_{a\mathbf{q}}|^2 \delta(E - \varepsilon_{\mathbf{q}}) = \Delta_b.$$

Contrary to the former, the surface state contribution is energy-dependent and is governed by the step-like onset of the Shockley surface state:

$$\Delta(E)_s = \pi \sum_{\mathbf{k}} |V_{a\mathbf{k}}|^2 \delta(E - \varepsilon_{\mathbf{k}}) = \Delta_s \Theta(E - E_0).$$

Based on Equation 3.2, the adsorbate's LDOS $n_a(E)$ depends on $\Delta(E)$, and hence the structure in the surface LDOS will translate into a surface-induced feature in $n_a(E)$, e.g. a bound state, as shown in Figure 3.8. On the contrary, bulk contributions just shift and broaden the spectrum, transforming the bound state into a resonance. The bound state in Figure 3.6b is the signature of the localization of the surface state below, but exponentially close to the surface-state onset. A more accurate modeling of the surface state is achieved [99], when using:

$$n_a(E) = \frac{1}{2} + \frac{1}{\pi} \arctan \frac{2(E - E_0)}{\Gamma},$$

Γ being the inverse lifetime of the surface state [120]. The bound state acquires then an increased linewidth (*cf.* Fig 3.8b), and a smooth variation occurs near the onset of the surface state in agreement with observations.

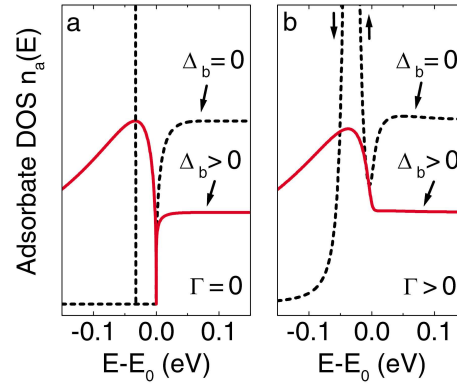


Figure 3.8: Adatom DOS with a surface-state DOS (a) $n = \Theta(E - E_0)$, (b) including lifetime effects. Dashed lines: without a coupling to the bulk states; solid lines: with a coupling to the bulk states. For clarity, part of the bound state is not shown in panel (b). Figure adapted from Ref. [52].

3.2.4 Density of states: surface induced states versus atomic resonances

The section above provided some insight into the localization of the surface state at the adatoms site, *i.e.* the formation of a bound state, when placing an adatom with an attractive potential onto dispersive $s - p$ states. A similar behavior is expected for transition metal atoms residing on the cobalt islands, which will interact with the dispersive majority $s - p$ states leading to a majority bound state. The common resonance in the dI/dV in Figure 3.4b should, at least in part, be due to such a bound state. However, additionally to the majority $s - p$ states, minority d resonances are present on the islands as unveiled in section 2.2 and will cause additional minority states in the LDOS above the adatoms following the News-Anderson approach presented above. Moreover, bare d resonances of the adatoms may also contribute to the LDOS. To sum up, we expect:

- surface induced majority and minority states
- atomic d resonances

to be present above the adatom.

To gain a quantitative picture on how these different contributions combine for the different transition-metal atoms (Cr, Fe, Co, Ni and Cu), *ab initio* calculations based on the density

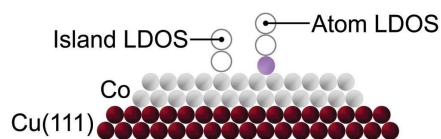


Figure 3.9: Setup for the LDOS calculation above the atoms (Fig. 3.10) and islands (Fig. 2.8), respectively.

functional theory implemented in the multiple-scattering KKR Green's function method in the atomic sphere approximation [79], were performed at the Max-Planck-Institut in Halle. The nanoislands were modeled as a cobalt bilayer, placed on semi-infinite Cu(111) in a way that the atoms of the lower cobalt layer occupy either fcc or faulted hcp sites of the substrate. The LDOS for the atom has been calculated in a vacuum sphere 0.42 nm above the adatom as shown in the scheme in Figure 3.9. This accounts for the experimental tip position during spectroscopy.

Magnetic moments

A first result of the calculations is presented in Table 3.1. All atoms are coupled ferromagnetically to the substrate, except Cr, which couples antiferromagnetically in agreement with Ref. [8]. The net magnetic moment decreases with increasing atomic number from roughly $4 \mu_B$ for chromium to almost zero for copper. However, the energy-dependent spin-polarization $P(E)$ as defined in equation 3.1 (page 35) does not correlate with the global magnetic moment, as we show hereafter.

Spin-resolved density of states

Figure 3.10 presents the majority and minority LDOS above a clean faulted island and above the different calculated adatoms residing on a faulted island. The majority states (red lines) of

Table 3.1: Calculated magnetic moments of transition-metal atoms residing on cobalt nanoislands on Cu(111).

Cr	Fe	Co	Ni	Cu
$4.16 \mu_B$	$3.18 \mu_B$	$2.00 \mu_B$	$0.74 \mu_B$	$0.03 \mu_B$

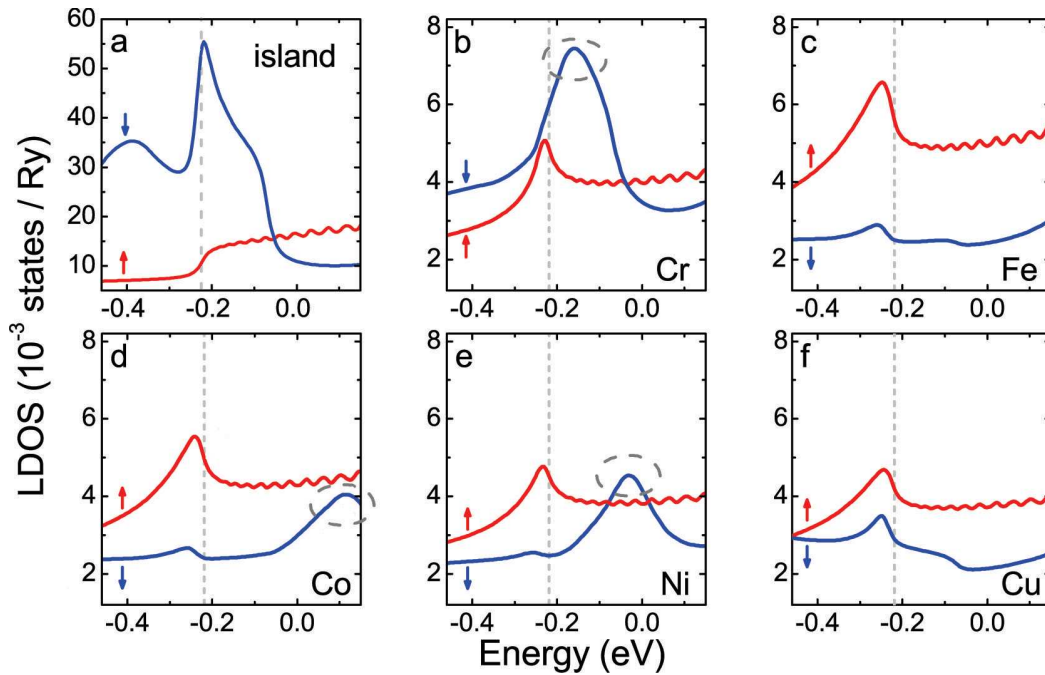


Figure 3.10: Calculated spin-polarized LDOS of transition-metal adatoms residing on faulted cobalt nanoislands. The LDOS is calculated in a vacuum sphere 0.42 nm above the adatom as depicted in Fig. 3.9 to account for the tip position in the STS experiment. The adatom element is indicated in each graph.

all atoms present, as expected from the Newns-Anderson model, a bound state just below the calculated onset of the dispersive $s - p$ states of the island (indicated by a dashed line). The island's minority states are dominated by d -like structures (*cf.* Fig. 3.10a). These translate for all different atoms into surface induced minority states. Both minority and majority states vary in intensity depending on the atoms nature. For Ni, Co and Cr, in addition to these surface-induced states, atomic d resonances of minority character appear [112,121]. In Figure 3.10 they are marked by dashed circles.

The multiple contributions can result in different scenarios for the elements investigated. For Fe, the majority states dominate over the whole spectrum and the majority bound state is well superior to the surface induced minority states, no atomic-like resonances are evidenced. For Co and Ni the majority bound state still dominates the surface induced minority states, but at higher energies a minority atomic resonance is observed. These resonances, falling at 0.1 eV for Co and close to E_F for Ni, reduce the polarization at the respective energies. In view of the dominant majority states, it is most likely, that the resonances observed by STS for Fe [8],

Co and Ni are bound states of majority character. We can then use the high-energy flank of the Ni and Co resonances (grey dashed line in Fig. 3.4b for faulted islands), to determine the onset of the dispersive majority $s - p$ states. STS provides thereby another way to estimate the energy onset of the majority surface state although it is buried under the dominant d states of the islands. We find energies of respectively -0.27 eV and -0.30 eV for faulted and unfaulted islands, which lies within the range found by Pietzsch *et al.* [7]. This stacking-dependent shift for the onset of the $s - p$ states is also predicted by theory (*cf.* Fig. 2.8, page 22). Regarding the influence of the atomic-like resonances, they all lie outside of the experimentally examined range (other energies turned out to be unstable for spectroscopy), but the marked increase in intensity towards E_F in the Ni spectrum could be interpreted as the onset of the atomic-like resonance at the Fermi level.

For Cu, no atomic-like resonance is observed but the difference in intensities of majority and minority states is less pronounced. Hence the observed peak in STS is more likely to be a mixture of minority and majority states. In the case of Cr finally, the only element coupled antiferromagnetically to the substrate, the atomic-like resonance falls just above the surface-induced majority and minority states and dominates the spectrum over a wide energy range. Therefore the resonance observed in STS in Ref. [8] at -0.1 V (see Fig. 3.2) likely originates from an atomic d resonance.

Energy-dependent spin-polarization

In the following we will focus on how different adatoms, which act as impurities (Cu, Fe, Cr and Ni) or protrusions (Co), alter the energy-dependent spin-polarization above the sample (see Fig. 3.11). The polarization determines the spin-dependent transport properties of the tunnel junction and is therefore of interest with respect to SP-STM or planar magnetic tunnel junctions (MTJs). Below the Fermi level the spin polarization of the pristine island is negative with a minimum of -66% at -0.23 eV, which is just below the calculated energy of the main d resonance of the island (called P1 in section 2.2). All adatoms, except Cr, cause an inversion of the polarization at this energy, the polarization becoming positive with local maxima at the same energy. With increasing atomic number the maximum decreases in intensity from $+41\%$ for Fe to $+19\%$ for Cu. Furthermore, for Co and Fe the polarization over the whole investigated energy range is now positive, for Ni a negative polarization is only observed around E_F , where the atomic-like resonance is located, and for Cu a shift to negative polarization is

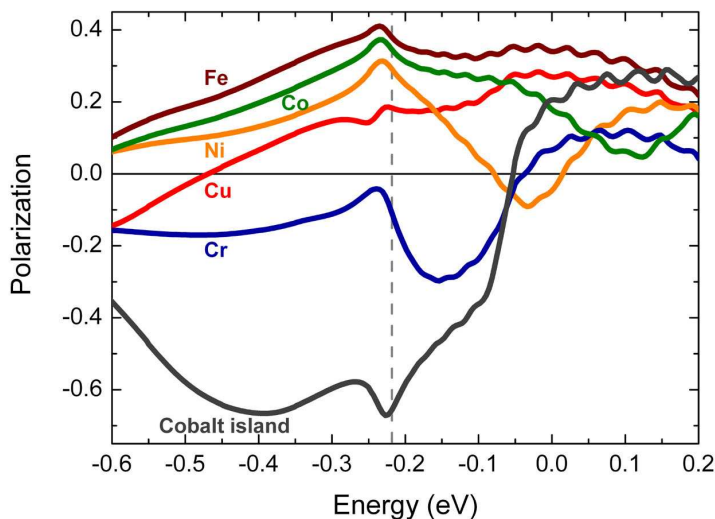


Figure 3.11: Calculated spin-polarization above clean cobalt nanoislands and individual atoms residing on the islands as a function of energy. The dashed line indicates the position of the onset of the calculated $s - p$ states.

seen for energies below -0.4 eV. Chromium has a negative, but, compared to the island, strongly reduced polarization below E_F due to its minority d resonance. It reaches its minimum of -30% at -0.18 eV and increases to low positive values above E_F . From a spintronics' viewpoint, the spin-polarization at the Fermi level is of particular interest. Here iron reaches the highest polarization of $+37\%$, which is even higher than the one of the pristine island. Remarkably, the copper atom with an almost zero magnetic moment, has a stronger polarization ($+27\%$) compared to Cr ($+7\%$), Co ($+18\%$) and Ni (-5%), which is due to the minority atomic-like resonances falling near E_F for the later elements.

Summary and conclusions

Single atomic adsorbates on a magnetic surface are shown to locally alter the spin-polarization. This holds even when the protrusion consists of the same element as the surface (*cf.* the case of Co). Our results compare well with recent simulations on impurity atoms at the tip apex of Cr-coated W-tips [122]. While the pristine island is governed by minority d states and provides strong negative polarization, the adatom LDOS shows positive polarization in vacuum aside the

energies where atomic resonances fall. Surface-induced states favor the majority LDOS, while atomic resonances are of minority nature. Hence a single atom acts here as a bias-dependent spin filter, which opens up perspectives for future spintronic devices. Additionally, some insight into the influence of surface roughness on the properties of planar MTJs is gained. Since a single protrusion locally inverts the polarization, for surfaces with a small number of protrusions, the global spin-polarization of the surface is reduced compared to the ideal surface. For higher coverage, even an opposite global polarization is possible.

The presented calculations do not take into account the spin-polarized electronic transport, *i.e.* spin-dependent conductance of the MTJ, but are LDOS-based. However, the conclusion that roughness weakens surface d states and therefore reduces the polarization is in good agreement with recent calculations on spin-transport through tunneling as a function of surface roughness in a planar Fe|vacuum|Fe MTJ [123]. Although atomic resonances were not explicitly evidenced in the study by Xu *et al.*, it was shown, that the majority conductance channel is enhanced by atomic roughness, even more, as the tunneling current depends exponentially on the distance, protrusions being closer to the opposite electrode compared to the surrounding surface.

If we turn back to the initial point of our study, *i.e.* the SP-STs data reported for Fe and Cr atoms residing on the cobalt nanoislands by Yayon *et al.* [8], we can find some encouraging agreement for the Cr atom (*cf.* Figure 3.2B), since the experimental polarization is indeed weak near -0.30 eV, and negatively enhanced at -0.15 eV, where the atomic-like resonance is predicted. On the contrary, even though the spectra acquired above Fe adatoms (*cf.* Figure 3.2A) agree well with our calculations, the polarization found in experiment is opposite to our predictions. Our results indicate, that the antiferromagnetic Cr tips employed in the experiment by Yayon *et al.* favor a negative polarization of the tunnel junction. At the same time, this indicates that pure LDOS calculations are not sufficient to completely understand SP-STM experiments, but a theoretical description in terms of spin transport [124], which is beyond the scope of the present study, would be needed, taking the antiferromagnetic tip structure and the transmission factor of different transport channels into account.

Furthermore, the presented results underline the key role played by the tip structure in SP-STM experiments. In a gedankenexperiment that turns the STM setup upside-down, a flat, magnetic surface (in our case the cobalt island) with a single atomic protrusion can mimic an atomic SP-STM tip. The tunneling from the tip is dominated by the LDOS above the atom's site and therefore favors majority polarization. If the protrusion is removed, a flat surface,

i.e. a blunt tip remains and the LDOS is now governed by minority states over a large bias ranges, the polarization being inverted. This demonstrates on the one hand the necessity of carefully modeling the tip, when theoretically calculating the electronic transport in an SP-STM experiment. And, for the experimentalist, on the other hand, this highlights the influence of the tip nature, shape and treatment on the results of the experiment.

CHAPTER 4

Single Cobalt-Phthalocyanine molecules on a magnetic and a nonmagnetic surface¹

Understanding the adsorption of a molecule on a metal surface, the interaction between adsorbate and adsorbent and its impact on the electronic transport properties of the system are among the key interests in the fields of molecular electronics and spintronics nowadays. In this context, we investigated individual Cobalt-Phthalocyanine (CoPc) molecules adsorbed on Cu(111) and on cobalt islands grown on Cu(111), respectively. While, for the adsorption on the magnetic surface, an overview is given on how the stationary spin-states of a single molecule can be visualized by means of SP-STM, for molecules residing on copper, we focus more specifically on the adsorption geometry, adsorption energy and the electronic transport. The theoretical calculations presented in this chapter are part of collaborations in the framework of two publications [33, 125].

The DFT calculations regarding the adsorption and the partial density of states (pDOS) of CoPc on Cu(111) and on cobalt islands presented in this chapter have been carried out by Thomas Brumme^{2,3} and Jens Kortus.² The transport calculations for CoPc on Cu(111) have

¹This chapter presents results published in *Phys. Rev. Lett.* **101** 116602 (2008), and *J. Phys. Chem. Lett.* **1** 1517 (2010), respectively.

²Institut für Theoretische Physik, Technische Universität Bergakademie Freiberg

³Present address: Institute for Materials Science and Max Bergmann Center of Biomaterials, Dresden University of Technology

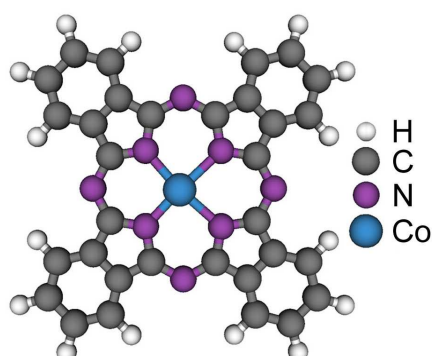


Figure 4.1: Chemical structure of CoPc. Different chemical elements are shown in different colors following the color code in the caption. The central cobalt ion binds to four nitrogen atoms; eight nitrogen and eight carbon atoms form a macrocyclic, which presents the core of the organic ligand.

been provided by Werner A. Hofer.⁴

4.1 Cobalt-Phthalocyanine - a brief introduction

Cobalt-Phthalocyanine is a member of the family of phthalocyanines, which are among the most studied molecules in molecular electronics and spintronics. Phthalocyanines and the closely related porphyrins provide a huge variety of properties paired with a relatively simple chemical structure, which makes these molecules appealing for surface scientists. The class of phthalocyanines is named after its simplest member, phthalocyanine (H_2Pc). H_2Pc is a macrocyclic compound with an alternating nitrogen-carbon ring structure that binds two H atoms in its center. The whole structure consists of four benzopyrrole units, which are connected via azo-bridges (see the chemical structure of CoPc in Fig. 4.1). In chemical nomenclature the name of H_2Pc is tetrabenzotetraazaporphyrin. Via exchange of the central hydrogen atoms with a metal atom a wide variety of metallophthalocyanines (MPc) is achieved as most metals have been found to coordinate to the phthalocyanine macrocycle. Furthermore some metal ions allow for binding of additional ligands. CoPc is one of the members of the family that possesses an unpaired spin and hence is particularly interesting from a spintronics point of view. However the magnetic anisotropy of CoPc is not strong enough to fix the magnetic moment of the central cobalt. Figure 4.2 shows the symmetry of selected molecular orbitals as presented by calculated

⁴Surface Science Research Centre, University of Liverpool

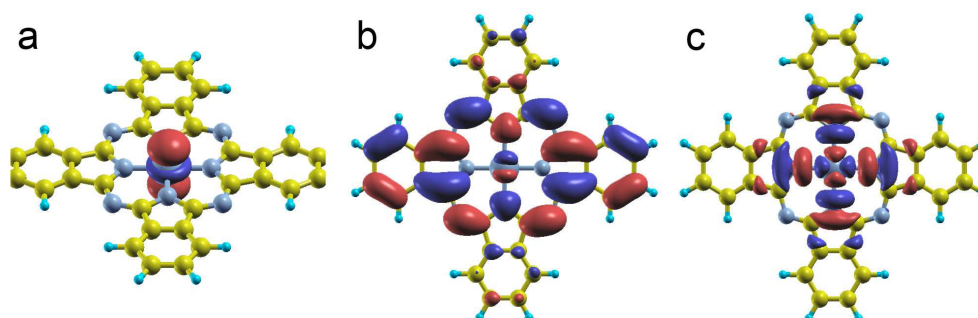


Figure 4.2: Isosurface plots of CoPc in vacuum at energies of: -6.32 eV (a), -4.68 eV (b), and -4.06 eV (c).

isosurface plots.

After a first "accidental" synthesis of H_2Pc in 1907 [126], $CuPc$ became in 1927 the first metallophthalocyanine that was intentionally synthesized [127]. Its chemical structure was determined by means of X-ray diffraction [128], and finally, in 1987, $CuPc$ became the first molecule investigated by STM [129]. Since then numerous STM/STS studies explored various phthalocyanines on metal and semi-conductor surfaces, individual molecules as well as mono- or multi-layers of phthalocyanines (see *e.g.* Refs. [130–137]). Regarding industrial applications, phthalocyanines have been used as dyes in textile and paper industries since the 1930s due to their brilliant colors and chemical stability. But since then they have found numerous applications in different fields of industry and technology [138], for example as electrode material in fuel cells, in organic light-emitting diodes and solar cells [139, 140], or in cancer therapy [141]. It is the relatively simple chemical structure of phthalocyanines, which can easily be modified, paired with its vacuum-compatibility (it is vaporizable but chemically stable), and the built-in metal-organic structure, which makes these molecules standard compounds for molecular spintronics [142, 143], or optoelectronics [144], and a first choice for our studies, as described below.

4.2 Cobalt-Phthalocyanine on Cu(111) - how adsorption affects transport properties

Recent STM/STS studies demonstrate the compelling necessity of determining the adsorption site [145], the close environment [146, 147], and the distortions [148–151], of metallophthalocyanines on metal surfaces.

cyanine and metalloporphyrin molecules on a surface to correctly describe their conductance. Additionally, the adsorption process on surfaces is crucial for the self-assembly of molecules into thin films. Generally speaking, a self-assembled molecular layer reflects a subtle balance between molecule-surface and molecule-molecule interactions, the latter including direct (dipole-dipole and $\pi-\pi$ interactions, hydrogen bonds, etc.) as well as surface-mediated interactions [152,153]. The intermolecular interactions, and consequently the growth into the self-assembled layer, are in turn affected by the symmetry that the molecule adopts upon adsorption onto the surface. However the behavior of a molecule on a surface is still difficult to predict, unambiguous results for the exact adsorption geometry and the symmetry being rare. Regarding the adsorption, most STM studies are still limited to the determination of the angle between molecular axes and the high symmetry directions of the surface, Refs. [22, 23, 151, 154–156] being rare exceptions. And the question of symmetry, which, in principle, could be answered by means of STM, is not straightforward either [157]. STM visualizes the electronic structure of a molecule, which is to a large extent determined by the molecular orbitals (MOs). From quantum chemistry we know that a free-standing molecule has MOs of different symmetry—which can differ from the structural symmetry, and, as a consequence, the imaged symmetry depends on the applied bias. Moreover, once the molecule is adsorbed the MOs mix due to the molecule-metal interaction. Additionally, the molecule may distort and the tunneling process may be favored for some MOs compared to others so that it is quite challenging to predict the symmetry of an adsorbed molecule. Despite the potential symmetry transfer from individual molecules to their self-assembled layer, chirality being one of the most striking examples [158–160], STM/STS studies devoted to the symmetry of an adsorbed molecule still remain limited [22, 161].

In this section we present how well-known scanning techniques such as tip-assisted atom manipulation and constant-height conductance maps, which were acquired for the first time in relation to single molecules, can be used to determine the adsorption geometry and to visualize the molecular conductance with a high intramolecular resolution of a single CoPc molecules on a copper (111) surface. By comparing our results with DFT calculation by Thomas Brumme, Jens Kortus and Werner Hofer we can unveil the central role played by the nitrogen atoms in both the adsorption and the tunneling process.

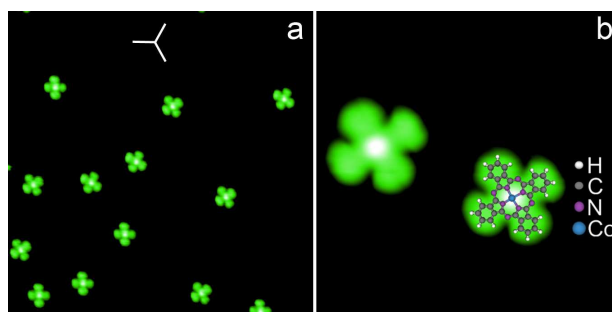


Figure 4.3: Topographic images of isolated CoPc molecules residing on Cu(111). a) Constant current image ($220 \times 220 \text{ \AA}^2$, -1.0 V , 0.02 nA). The closed-packed high symmetry directions $\langle 110 \rangle$, $\langle 101 \rangle$ and $\langle 011 \rangle$ of the crystal as determined by tip-assisted atom manipulation (see Fig. 4.4c) and copper step edges are indicated by white lines. b) High-resolution image with a structure scheme of CoPc superimposed over one molecule ($40 \times 40 \text{ \AA}^2$, -1.0 V , 0.5 nA).

4.2.1 Unveiling the adsorption site of CoPc on Cu(111)

Figure 4.3 shows isolated CoPc molecules deposited at room temperature on the Cu(111) surface and cooled down to 4.6 K after deposition. At this coverage,⁵ the molecules are randomly distributed in agreement with results for other MPc molecules [22,161], and well separated. This distribution could be influenced by a repulsive interaction between the molecules as reported for phthalocyanines on other surfaces [152]. An additional study with a series of different coverage is necessary to conclude concerning the molecule–molecule interaction, which is beyond the focus of this chapter. At -1 V , the molecule (*cf.* Fig. 4.3b) has a four-lobe pattern (1.2 \AA high) with a central protrusion (1.6 \AA), which corresponds to the cobalt ion. The apparent width of 18 \AA is consistent with the chemical structure of the molecule. The analysis of different topographs like the one in Figure 4.3a reveals three different in-plane orientations of CoPc molecules on Cu(111), which differ one from another by a rotation of 120° . Each molecule has one pair of opposite benzopyrrole units (in the following called "legs") aligned parallel to the closed-packed high symmetry directions $\langle 110 \rangle$, $\langle 101 \rangle$ and $\langle 011 \rangle$ of the crystal. Therefore the three orientations are equivalent due to the surface symmetry.

However, to determine the exact adsorption site, one has to image the copper surface atoms, which is not straightforward for the compact (111) surfaces of noble metals due to the weak electronic corrugation. To do so in a routinely manner, we co-deposited CoPc molecules and

⁵0.03 monolayers of CoPc on the Cu(111) surface. One monolayer corresponds to one molecule occupying an area of 140 \AA^2 .

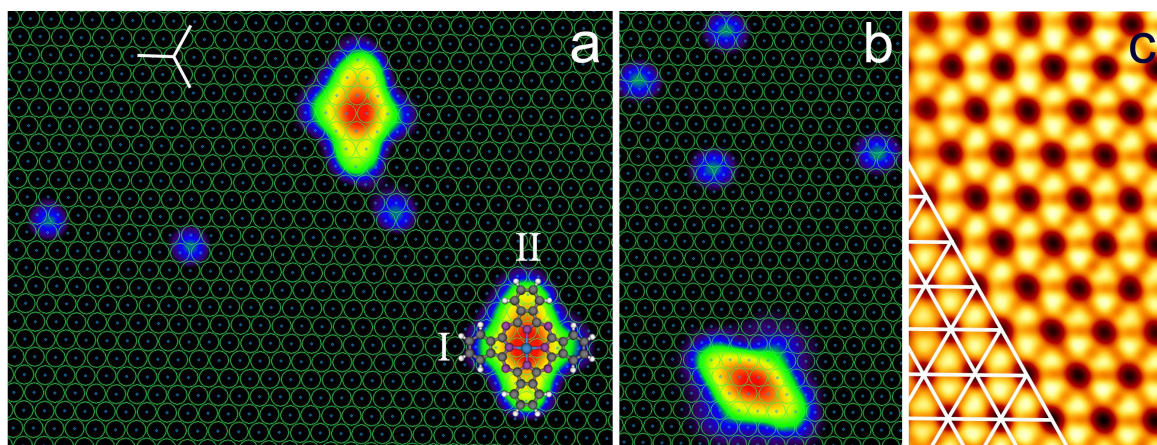


Figure 4.4: Determination of the adsorption site of CoPc on Cu(111). a and b) co-deposition of copper atoms and CoPc molecules ($76 \times 55 \text{ nm}^2$ (a) and $41 \times 63 \text{ nm}^2$ (b), 50 pA, -1 V). The copper lattice as determined by atom manipulation [*cf.* (c)] is superimposed. c) Manipulated-atom image of the Cu(111) surface by means of tip-assisted copper atom manipulation ($13 \times 22 \text{ \AA}^2$, 15 nA, -5 mV).

copper atoms and applied tip-assisted atom manipulation (for details see section 1.1) [12, 23]. Figure 4.4c shows an example of a so acquired manipulated-atom image. The image shows dark spots (minima), which correspond to the surface copper atoms, while the bright triangular protrusions (maxima) are the fcc and hcp hollow sites. The exact orientation of the symmetry directions of the surface as well as the interatomic distances can then be determined. A scheme of the surface lattice is superimposed in the lower left part of the image of Figure 4.4c. Furthermore this method allows to accurately calibrate the voltage-versus-elongation of the piezo element in the close vicinity of the molecule.

To determine the adsorption position of CoPc, we imaged simultaneously CoPc molecules and co-deposited copper adatoms in the normal topography mode with high resolution and superimposed the lattice scheme extracted from the atom manipulation image (see Fig. 4.4a and b). The copper adatoms, which adsorb in the hollow sites of the (111) surface, are used as markers to position the lattice sketched in Figure 4.4c [23, 154–156]. Auwärter *et al.* used a similar technique to determine the adsorption site of tetrapyrrolyl-porphyrin molecules on Cu(111) by co-depositing CO molecules, which adsorb on top of the surface copper atoms [151]. To get a clearer picture of the adsorption, we superimpose the model structure of CoPc over an imaged molecule in Figure 4.4a. The two mirror axes of the imaged molecule unambiguously determine the position of the molecular structure. As shown in Figure 4.4a the central cobalt

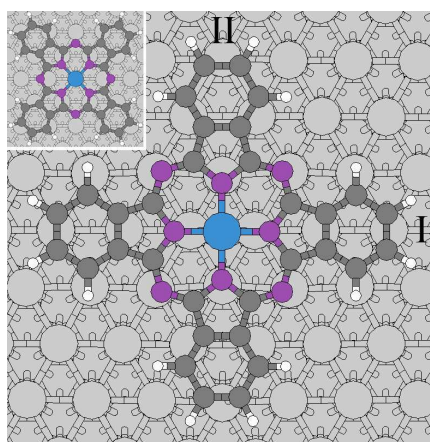


Figure 4.5: Adsorption optimization of CoPc on Cu(111) by DFT. The calculation reveal a bridge position of the center Co atom and an alignment of axis I with the closed-packed symmetry direction of the (111) surface. The molecule remains planar upon adsorption. The inset shows the metastable top position, which is 0.3 eV higher in energy compared to the bridge ground state.

atom is situated in a bridge position between two copper surface atoms. One pair of organic legs is aligned following an axis labeled I. This axis is perfectly aligned with a compact, high symmetry direction of the surface lattice. The axis II has an angle of 90° with respect to the high symmetry direction. Axis I of the molecule in Figure 4.4b is aligned parallel to a different high symmetry direction compared to the other molecules in the figure, but presents an equivalent adsorption site, as may be anticipated by the sixfold rotational symmetry of the surface.

A closer look at axes I and II of CoPc in the topographies of Figure 4.4a and b shows that the legs have a different contrast along the two axes. This difference could either arise from a distortion of the molecule upon adsorption as conjectured by Chang *et al.* [161], or from differences in the electronic structure, i.e. the LDOS above the axes, since the two axes are not equivalent from a structural viewpoint. To reveal the possible existence of distortions and the contribution of the different parts of the molecule to the adsorption, density functional theory (DFT) calculations⁶ were performed by Thomas Brumme and Jens Kortus. The substrate was

⁶Adsorption optimization and LDOS calculation by means of density functional theory (DFT) as implemented by the PWSCF code [162]. Ultrasoft (Vanderbilt) pseudopotentials based on local density approximation (LDA) together with a kinetic-energy cutoff of 25 Rydberg (Ry) for the plane wave basis set were employed. The charge density cutoff was set to a value more than 10 times larger and the ground state density for a single Γ -point proved to be sufficient. The convergence has been tested with a larger kinetic energy cutoff of 30 Ry. The

modeled using three layers of copper in the (111) orientation with about 22 Å vacuum to the next periodically repeated layer.⁷ The distance between the CoPc molecules of the periodically repeated cells was about 6 Å resulting in a 249 atom model. The CoPc was initially placed at 2 Å above the Cu layers. During the following adsorption optimization, only the atoms of the lowest copper layer were held fixed at the position according to the bulk values. Different starting geometries (central atom on a top, bridge, hollow position) have been checked with various orientations of the four benzopyrrole groups relative to the copper compact rows.

The geometry optimization always showed that the lowest energy is obtained for a bridge position of the central cobalt ion as shown in Figure 4.5 (cobalt in blue) with one pair of opposite benzopyrrole groups aligned with a compact row (axis I in Figure 4.5). Furthermore all nitrogen atoms (purple) are found close to or on top positions. The calculated adsorption site is in excellent agreement with the experimental findings of Figure 4.4. Wang *et al.* found a similar adsorption for SnPc on Cu(111) [150]. An on-top adsorption site was found to be metastable, to say higher in energy compared to the bridge site (see inset in Figure 4.5). The hollow site is always unstable, regardless of the initial configuration. The actual adsorption site of CoPc on Cu(111) is a compromise between the favored positions of the nitrogen atoms and the benzene rings on the surface. The p_z orbitals of nitrogen and carbon tend to hybridize with the d_{z^2} orbitals of the surface atoms (*cf.* Fig. 4.9). While nitrogen favors a position on top of a surface copper atom as can be anticipated from other molecules [151, 163, 164], the benzene rings adsorb preferably flat with the center above a hollow site [164–166]. In the case of FePc/Au(111) this leads to two co-existing adsorption geometries close in energy, with the central Fe atom either in a top or in a bridge position [145]. As mentioned above, for CoPc on Cu(111) we also find two adsorption geometries. In the top position, the four benzene rings are centered in a hollow site of the surface, which is the favored site. However all nitrogen atoms are more or less strongly displaced relative to the copper surface atoms and therefore in less favorable positions (see inset of Figure 4.5). A determination of the surface–molecule distance reveals a distortion of CoPc. While the center of the benzene rings is found at 2.15 Å from the surface plane, the pyrrole rings are 0.20 Å higher. The central cobalt ion is in a top position at a distance of 2.45 Å from the underlying copper atom and therefore highest. Nevertheless this

self-consistent solution of the Kohn-Sham equations was obtained when the total energy changed less than 10^{-6} Ry and 5×10^{-3} Ry/Bohr in case of force.

⁷Increasing the slab to four copper layers only shifted the Fermi energy by 0.1 eV, with no appreciable change in the adsorption geometry of CoPc.

distance is well below the ideal Co–Cu bond length of 2.64 Å, as the robust molecular body prevents further bending. Contrary to the top adsorption, in the bridge position the molecule remains undistorted as in vacuum, all functional groups lying in one molecular plane at 2.30 Å above the surface. While in this configuration only two benzene rings are centered above a hollow site and the two others are found above a bridge site, all nitrogen atoms are close to a top adsorption. Hence, additional hybridization between nitrogen and surface copper atoms is possible and lowers the ground state energy by 0.3 eV compared to the top adsorption. The cobalt atom in the bridge position is 2.60 Å away from the two nearest copper atoms, which is close to the ideal value. In agreement with the experimental results, CoPc is found to adsorb in a bridge position with one molecular axis parallel to the compact symmetry direction of the surface. The molecule remains undistorted upon adsorption.

	Component	Energy [Ry]
a.	CoPc/Cu(111)	−17476.932
b.	Cu(111)	−16859.877
c.	CoPc (vacuum)	−616.550
d.	H ₂ Pc (vacuum)	−544.595
e.	H ₂ Pc/Cu(111)	−17404.910
f.	Co ²⁺ /Cu(111)	−16933.649
g.	Co (vacuum)	−73.674

Table 4.1: Calculated DFT total energies (in Rydberg) used for determining the adsorption energy of CoPc on Cu(111). The Co atom has been placed above the Cu layers at the same distance as in the CoPC molecule. The positive charge of Co²⁺ was neutralized by a corresponding negative background charge in the cell.

4.2.2 Contributions to the adsorption energy

The determination of the adsorption of CoPc on Cu(111) allows now to estimate the contributions of the different parts of the molecule to the total binding energy by means of DFT calculations. To do so, the total energy of different subsystems, like the Cu(111) surface, the CoPc molecule in vacuum or different parts of CoPc in vacuum and adsorbed on copper have been calculated. The results are presented in Table 4.1. The total binding energy of CoPc on Cu(111) can be obtained directly by comparing the total energy of CoPc/Cu(111) (4.1a) with the total energy of the Cu(111) surface (4.1b) and of the free-standing CoPc (4.1c). Their

sum yields an energy of: $\text{Cu}(111) + \text{CoPc}(\text{vacuum}) = -17476.427 \text{ Ry}$, the difference with $\text{CoPc}/\text{Cu}(111)$ being -6.9 eV . This is the total energy gain upon adsorption.

Molecular fragments have been constructed to simulate the adsorption of different parts of the molecule and learn about their contribution to the total adsorption energy. The binding energy of a fragment can be calculated by using only closed shell structures to avoid additional charge transfer upon adsorption. Charged particles would make the comparison with the free-standing fragment unreliable. Free bonds of the fragments have been saturated with H atoms. In the case of the organic ligand of CoPc, for example, the central cobalt atom was removed and two H atoms were added and relaxed, resulting in H_2Pc . The total energy was determined for H_2Pc (Table 4.1d) and $\text{H}_2\text{Pc}/\text{Cu}(111)$ (Table 4.1e), for which the adsorption configuration found for CoPc was used and only the additional two H atoms were relaxed. The binding energy was estimated as 6 eV. The organic ligand contributes therefore with 6 eV to the binding energy while cobalt adds about 1 eV. This is in agreement with the calculated binding energy for an individual cobalt atom where the energy difference between Co^{2+} on Cu(111) (same bridge position as in CoPc, zero magnetization, Table 4.1f) and the sum of Co in vacuum (Table 4.1g) and Cu(111) is calculated as 1.3 eV. All energies are calculated without taking into account Van der Waals interactions, but due to the chemisorption of the system, they should play a minor role contrary to the case of physisorbed molecules [167]. The LDA approach tends to overestimate binding energies, but the qualitative results should hold.

4.2.3 Electronic transport and hybridization of CoPc/Cu(111)

The adsorption site and the binding energy being explored, we can now focus on the electronic transport of the CoPc/Cu(111) system. We use constant-height dI/dV spectroscopy and maps (see section 1.1.1 for technical details) to study the differential conductance, which is closely related to the density of states in vacuum [27]. The advantages of the constant-height mode compared to "normal" constant-current mode in spectroscopy are significant, as it offers a simplified comparison with DFT calculation and an enhanced contrast between areas of different conductance but same height. Furthermore topography-related artifacts [21, 27, 28], which also alter the imaged symmetry of the molecule, can be avoided. In chapter 1.1.1 in Figure 1.3 a comparison of topographic images, constant-current dI/dV maps and constant-height dI/dV maps of a single CoPc exemplifies this technical improvement. However, it has rarely been employed (for an exception see Ref. [168, 169]) and, to the best of our knowledge, never for

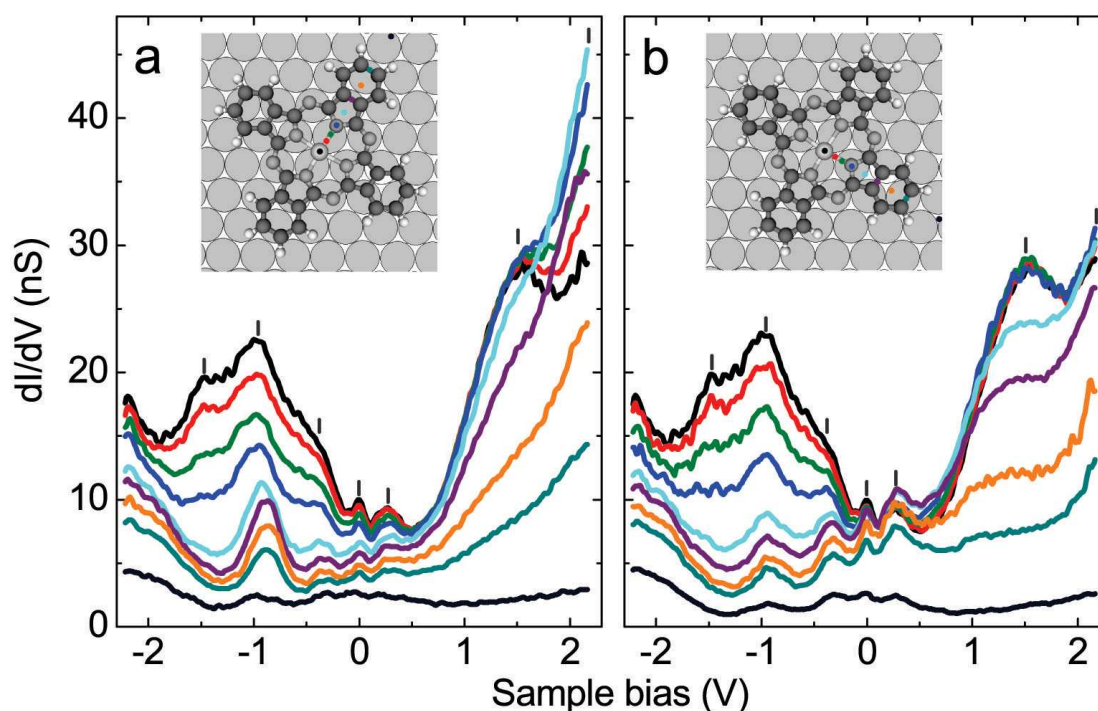


Figure 4.6: Constant-height dI/dV spectra of CoPc on Cu(111) along axis I (a) and II (b). Feedback opened above Cu(111) at 0.35 nA and -0.50 V. All spectra were acquired with a constant tip height with respect to the copper surface plane.

molecular systems. By comparing the experimental data with calculations of the pDOS from Thomas Brumme and Jens Kortus and transport calculation⁸ from Werner Hofer, we can learn more about the origin of the conductance observed.

Differential conductance of CoPc/Cu(111)

Figure 4.6 shows a collection of dI/dV spectra acquired above different spots along the two molecular axes I (Fig. 4.6a) and II (Fig. 4.6b), which are indicated in the corresponding inset. The tip-sample distance estimated at 9 \AA [175, 176], was fixed above copper and held constant with respect to the surface plane for all spectra. The spectra provide a series of features (marked

⁸Simulation of the conductance between the molecule/substrate system and a copper model tip was done by means of a multiple scattering approach [170, 171]. The surface and tip Kohn-Sham states were obtained using an all-electron method, the projector-augmented-wave method, which also includes the core region in the description of the electronic structure and is therefore generally more precise. In addition, the exchange and correlation potential were simulated by a well tested hybrid-functional, the HSE03 functional [172], as implemented VASP [173, 174].

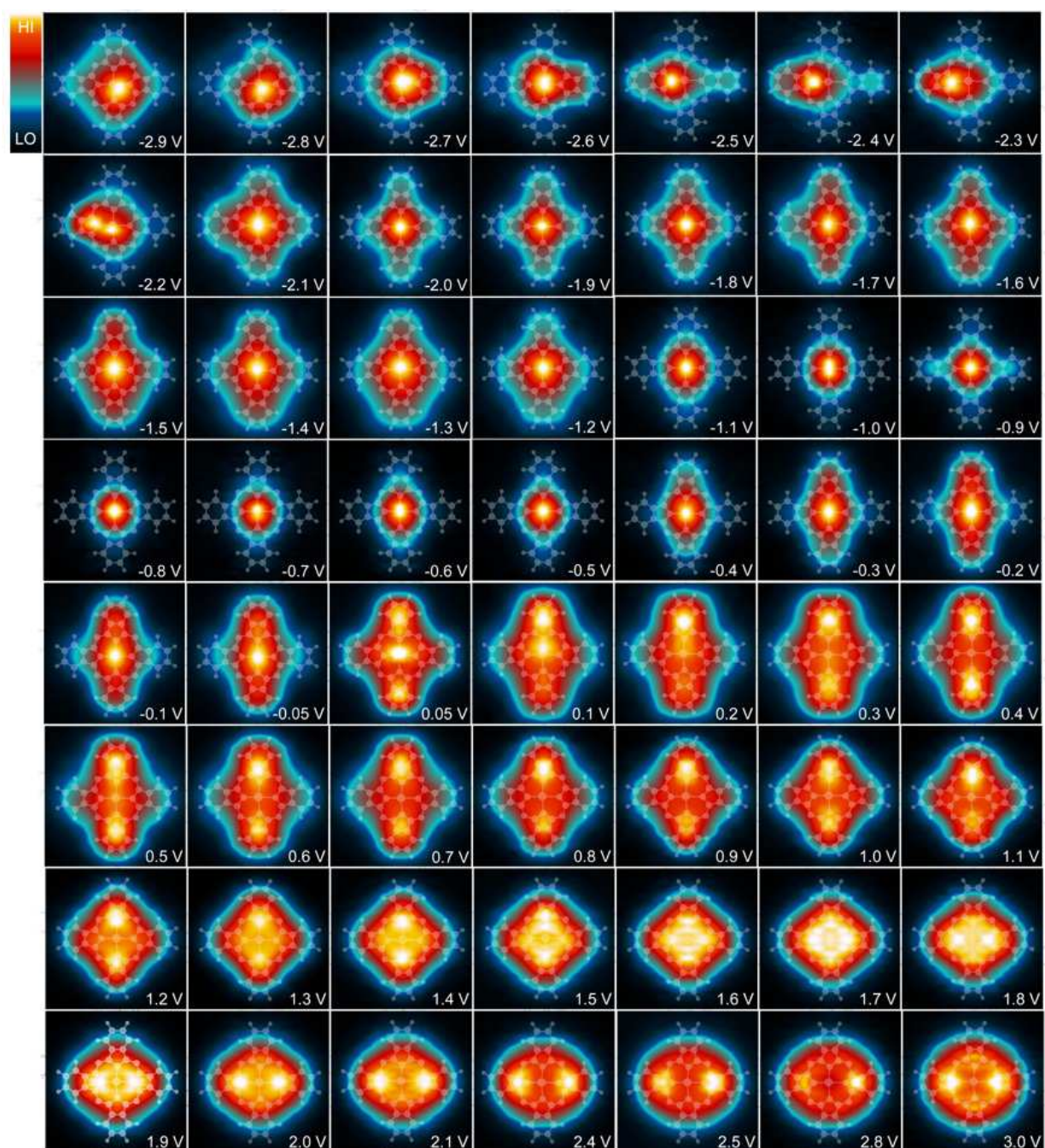


Figure 4.7: Constant-height dI/dV maps over CoPc ($20 \times 20 \text{ \AA}^2$). The feedback loop was opened over Cu(111) at 0.01 nA and at the bias indicated in each map. Maps were recorded every 100 mV in the bias range from -2.9 V to 3.0 V (exceptions: maps taken at $\pm 50 \text{ mV}$ but not at E_F ; above 2.1 V only four maps are shown at $2.4, 2.5, 2.8$ and 3.0 V). The model structure of CoPc is superimposed to the dI/dV maps in order to localize the signal maximum on the molecule.

by vertical lines in Figure 4.6), which vary in intensity depending on the tip location above the molecule. In the negative bias region, three main spectral features with a maximum at -1 V in the differential conductance are observed, the whole energy range being dominated by the central region of the molecule, mainly the cobalt atom. Towards the outer benzene rings a reduced conductivity is detected and differences along the two axes become visible, at -1 V the intensity of axis I is superior to the intensity of axis II. The positive bias region is dominated by a pronounced peak at 1.4 V, which is located on the N atoms. The spectrum is marked by an increased intensity when approaching 2 V, the signal maximum being now located over the pyrrole rings. The intensities found differ along the two axes, as in the negative bias region. Close to the Fermi energy and at 0.3 V, two more peaks are observed that vary in intensity over the molecule.

To get a clearer picture of the spatial distribution of the differential conductance, constant-height dI/dV maps were acquired. The feedback loop was opened above copper and then the area was scanned with a constant tip-copper distance, recording the differential conductance at each pixel of the image. In Figure 4.7 dI/dV maps at energies ranging from -2.9 to 3.0 V are presented and give an overview of the evolution of the spatially resolved differential conductance in this energy range. In the low energy range between -2.9 and -2.1 V, the signal maximum migrates in the proximity of the central cobalt. It is located between two nearest neighbor (n.n.) N atoms of Co at -2.8 V or directly over a n.n. nitrogen of axis I (-2.5 V). All maps present a C_1 rotational symmetry, some of them with a mirror plane through axis I. Between -2.0 V and -0.1 V the signal above cobalt dominates all maps in agreement with the spectrum in Figure 4.6. However, differences in the contribution of the differential conductance along the benzopyrrole units are apparent. Most maps show a C_2 symmetry with axis II being more intense than axis I. This is due to different signal contributions from the n.n. nitrogen of the two axes. Between -1.0 and -0.7 V almost no signal is detected on the legs compared to cobalt, which leads to an apparent C_∞ symmetry. Towards E_F , the intensity above axis II increases again, a C_2 symmetry is observed. In the positive bias range the dI/dV signal above axis II first becomes comparable to the cobalt signal (50 mV) and then starts to dominate. The signal maximum is located on the bond between the pyrrole and benzene unit, which is very pronounced at 0.4 V. With increasing bias the signal maximum migrates inwards to end up at 1.2 V above the center of the pyrrole rings of axis II, the rotational symmetry still being C_2 . If the bias is further increased, a transition takes place, which moves the signal maximum from axis II to axis I. At 2.4 V the maxima are located above the pyrrole rings of axis I, the

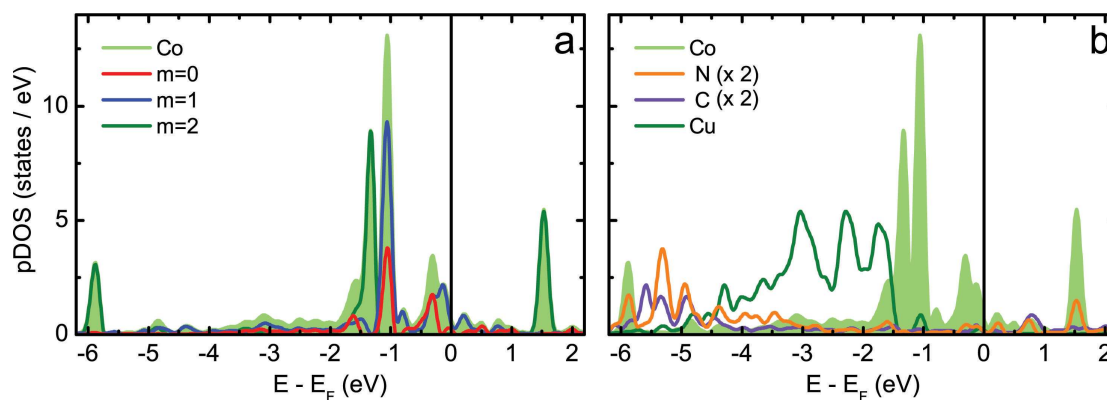


Figure 4.8: Calculated pDOS of the CoPc/Cu(111) system. a) d -state contribution of cobalt: $m = 0$ (d_{z^2} , $d_{z^2}^*$); $|m| = 1$ (d_{xz} , d_{yz} , d_{xz}^* , d_{yz}^*); $|m| = 2$ ($d_{x^2-y^2}$, d_{xy} , $d_{x^2-y^2}^*$, d_{xy}^*). b) pDOS of Co, N, C and Cu atoms. The N and Cu atoms are the n.n. of Co along axis I, while the C atom is taken on the pyrrole ring along axis I. The pDOS of nitrogen and carbon are scaled by a factor 2 for clarity.

C_2 rotational symmetry with a mirror plane through each axis is again established. During the transition, at 1.6 V, a C_4 symmetry is found, the two molecular axes being equivalent. Above 2.4 V the signal maximum migrates slightly towards the center, at 3.0 V an additional signal above axis II is observed.

Summarizing the observations from the dI/dV maps, we can conclude that the differential conductance below E_F is dominated by cobalt contributions. The positive bias range is governed by contributions from the organic ligand, mainly from N atoms and the pyrrole fragments. Over the whole energy range continuous changes in the relative intensity of axes I and II are observed, which alters the "apparent" symmetry of the molecule as a function of bias.

Partial density of states of CoPc/Cu(111) by DFT

To attribute the observed dI/dV signal to molecular orbitals, the partial density of states (pDOS) of the CoPc/Cu(111) system was calculated by DFT. Upon adsorption, hybridization between molecular orbitals and copper states takes place. The majority and minority population of the Co pDOS are equal, and the magnetization is decreased from $1 \mu_B$ to $0 \mu_B$. This is a first indication for bonding and charge transfer between CoPc and the copper surface. By means of a Löwdin population analysis an increase of the electron charge of the cobalt atom from 8.21 electrons for the free-standing molecule in vacuum to 8.63 electrons for the adsorbed

CoPc is found. At the same time, the hybridization shifts and broadens the molecular states. Figure 4.8a explores the pDOS of the d orbitals of cobalt. The $m = 0$ state, which is half filled for CoPc in vacuum, becomes filled for both spin directions and splits into a bonding state (d_{z^2} , peak at -1.0 eV) and an antibonding state ($d_{z^2}^*$, peak at -0.3 eV). The most intense peak of the $|m| = 1$ states falls at -1.0 eV and is associated with d_{xz} and d_{yz} states, while the lower peak at -0.2 eV originates from antibonding d_{xz}^* and d_{yz}^* states. Finally, the $|m| = 2$ states consist of a bonding $d_{x^2-y^2}$ state at -5.9 eV, a bonding d_{xy} state at -1.3 eV and an antibonding $d_{x^2-y^2}^*$ state at 1.5 eV.

In Figure 4.8b the pDOS of several atoms of CoPc is presented. Even though differences in intensity are found for atoms of the same species, for clarity we chose to present only a representative selection, which, however, provides the essential information. The figure includes the pDOS of the cobalt atom, a neighboring nitrogen atom, a neighboring copper atom, and a carbon atom, which are all located along axis I in Fig. 4.5. In the bias region between 0 and -2 V the pDOS is dominated by d -states of Co, in particular by the $|m| = 0$ and $|m| = 1$ states. This agrees well with the experimental data of Figs. 4.6 and 4.7 where the differential conductance in this bias range is governed by the central cobalt. For even lower biases the molecular contributions become weak but copper possesses a strong density of states. This might influence the conductance maps (Fig. 4.7) and lead to the asymmetry observed in the dI/dV maps. However this is not fully understood so far and further studies are needed to conclude on this point. In the positive bias range, strong nitrogen contribution to the pDOS are observed together with Co $|m| = 2$ states ($d_{x^2-y^2}^*$, d_{xy}^*). However STM is less sensitive to these $|m| = 2$ states as they are localized parallel to the surface plane. Therefore we expect similar conductance in the dI/dV above the pyrrole rings and the Co. This is confirmed by the transport calculations presented in Figure 4.10a.

The interaction of CoPc with the copper surface results in an overlap of the atoms pDOS at all energies. As shown in Figure 4.8b, copper possesses d states located between -5 eV and -1 eV. The CoPc molecule can hybridize with the surface in this energy range since cobalt d states as well as nitrogen and carbon p states are available as exemplified by the isosurface plots for selected energies in Figure 4.9. At -1 eV the two copper atoms n.n. of cobalt have a d_{z^2} state while cobalt has d_{xz} and d_{yz} states. These states hybridize as shown by Figure 4.9a. A typical bond between a nitrogen p_z orbital and a copper d_{z^2} state is shown in Figure 4.9b, whereas Figure 4.9c shows a typical bond between carbon p_z and copper d_{z^2} . We find also evidence for intramolecular hybridization, for example between nitrogen (p_z) and cobalt (d_{xz} , d_{yz}) at -1.2 eV

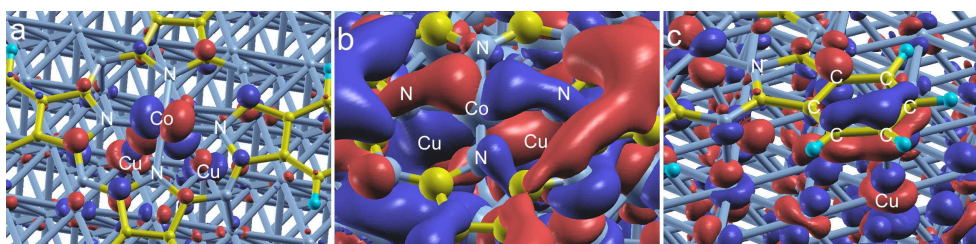


Figure 4.9: Isosurface plots at selected energies as determined by DFT give insight into the hybridization of CoPc with the surface. a) Antibonding at -1.1 eV between Co (d_{xz} , d_{yz}) and Cu (d_{z^2}). b) Bonding at -1.2 eV between N (p_z) and Cu (d_{z^2}), and between Co (d_{xz} , d_{yz}) and N (p_z). c) Antibonding at -1.2 eV between C (p_z) and Cu (d_{z^2}).

(see Figure 4.9b) and at -4.6 eV, or between nitrogen (p_x , p_y) and cobalt (d_{xy} , $d_{x^2-y^2}$) at -5.7 eV and -5.0 eV.

The pDOS of Figure 4.8 helps identifying the MO contributions of the dI/dV maps of Figure 4.7. Between -2 V and E_F , the highest molecular conductance is located over the Co and N atoms. While the d states are responsible for the signal detected over Co (likely d_{z^2} , d_{xz} and d_{yz}), the p_z -states of N govern the symmetry of CoPc. The contribution of the d states to the tunneling current through the central metal atom is a well-known property of metallophthalocyanines [33, 135, 137, 177–180], and of metalloporphyrins as well [151, 181]. At positive bias, in particular near 1.5 V, the molecular conductance is still mainly located over the Co and the N atoms. However, additional orbitals are present here compared to the negative bias. Based on the pDOS, the signal detected over Co may also be traced back to the $d_{x^2-y^2}$ orbitals of Co and to the p_x and p_y orbitals of N. The p orbitals of N are again responsible for the C_2 symmetry of CoPc. When increasing the bias to 2.4 V, a strong conductance channel is detected over the pyrrole ring, this location dominating even at higher biases. The C_2 symmetry here results from conductance through the p_z orbitals of N and C atoms. Between 1.4 V and 2.4 V the differential conductance has contributions from both the N atoms and the pyrrole rings. The rotational symmetry of the dI/dV maps in this bias range results therefore from the mixture of the maps at 1.4 and at 2.4 V. We attribute then the recovery of a C_4 symmetry at 1.6 V to this mixed contribution.

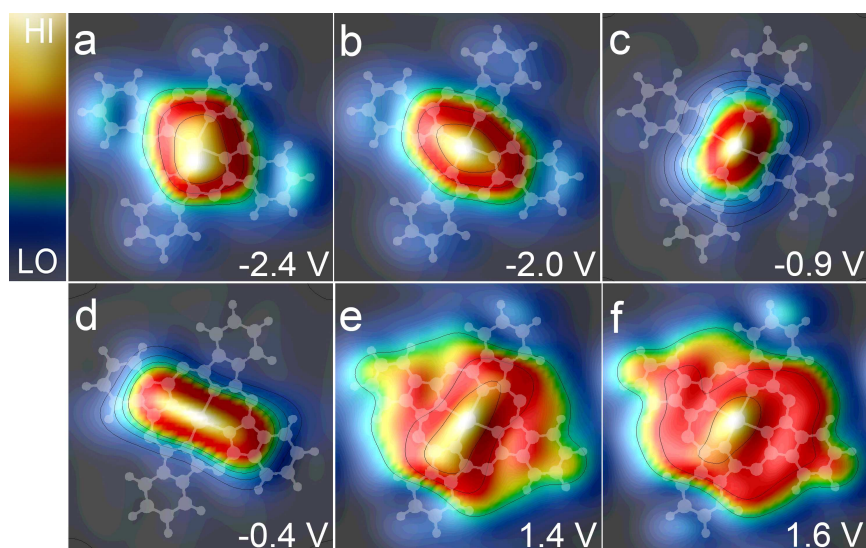


Figure 4.10: Calculated dI/dV maps over an isolated CoPc at selected biases: -2.4 V (a), -2.0 V (b), -0.9 V (c), -0.4 V (d), 1.4 V (e), 1.6 V (f).

Transport calculations for the CoPc/Cu(111) system

In order to compare Figure 4.7 to calculations, it is necessary to simulate the dI/dV maps. In fact, a dI/dV contrary to the pDOS also depends on how electrons tunnel between the tip and the molecule. However, similar spectral features are expected in the pDOS and the dI/dV , but with substantially different amplitudes. Werner Hofer provided computed conductance maps for a single molecule on Cu(111) by ramping the bias from -2.5 V to 2.5 V in steps of 0.1 V.⁸ The simulation directly summed up the differential contributions to avoid numerical instabilities due to differentiation, using a method described in a previous study [182]. In the plots shown in Figure 4.10, we evaluated the conductance at chosen energies in a plane parallel to the Cu(111) surface at a distance above the molecule, which coincides with the experimental tunneling conditions. As shown, the global features of the simulated bitmaps mimic closely the experimental data. We also find a change of symmetry with changing bias.

Since it was necessary to reduce the number of Cu-layers to a monolayer for the hybrid-functional simulations, which was shown to be sufficient regarding the overall good agreement between experiment and calculations, this indicates that the spectral features are to a large extent determined by the electronic structure of the molecule as anticipated above. The overall satisfying agreement proves that our adsorption optimization for CoPc on Cu(111) is realistic

and that the symmetry changes observed can be attributed to the detailed spatial and energetic distribution of the molecule's electronic eigenstates. However, some differences are encountered at positive bias, namely between E_F and +1.6 V, where the dominant signal above the pyrrole rings in the experimental dI/dV maps is not satisfyingly reproduced by the calculations. Further experimental findings (not shown here) yield strong evidence for an involvement of the surface state. DFT calculations by the group of Stefan Blügel⁹ are in progress in the framework of a future publication.

4.3 CoPc on cobalt nanoislands

After the in-depth study of the adsorption and conductance of CoPc on copper, we will now focus on CoPc adsorbed on cobalt nanoislands, paying attention to the spin-polarized properties of the molecules. In chapter 3, the interplay of an atomic adsorbate with the complex SP density of states of a ferromagnetic substrate was studied, revealing an energy-dependent inversion of the polarization due to a majority bound state at the atom's site and element-specific atomic resonances. A spin-filter-like behavior was demonstrated for the individual atoms, foreboding the feasibility of atomic-sized spintronic devices. However, individual-atom systems implicate a number of unsolved problems, the high atom mobility on metal surfaces being just one among others. One idea to solve these problems consists in replacing atoms by molecules, *i.e.* merging molecular electronics and spintronics, so that functional molecules become active device components within a circuitry where information is carried by electronic spins [183, 184]. Progress toward this tantalizing goal relies on the understanding of spin transport through individual molecules. Spin transport is usually measured across a well-chosen molecule attached to two magnetic leads [185, 186]. The variability of the resulting conductance is due to the incomplete control over the molecule-lead interface, which has attracted little experimental interest so far [142, 143]. A better understanding of this limiting drawback would allow engineering the desired spintronic functionalities into a molecule.

The feasibility of probing spin-polarized tunnel transport with atomic resolution by means of SP-STM and SP-STs was demonstrated in the last years [8, 96, 97]. However these techniques have, so far, never been used to study SP states of molecules adsorbed on metallic surfaces. The simultaneous access to the SP conductance and the sample geometry should provide a better

⁹Institut für Festkörperforschung, Forschungszentrum Jülich

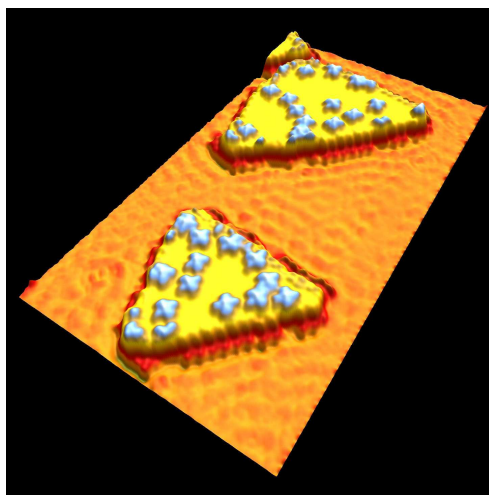


Figure 4.11: CoPc molecules on cobalt nanoislands grown on Cu(111). The pseudo-3D representation of the STM topograph shows the preferential adsorption of CoPc at cobalt step-edges (red) and on the island (blue). Interference pattern of surface-state electrons are observed on the copper surface ($40 \times 20 \text{ nm}^2$, 0.10 V , 0.50 nA).

understanding of the coupling between the molecule and the substrate and its influence on the electron transport properties. With this in mind we extend our study of individual atoms on magnetic nanoislands and "dress" a single atom with an organic ligand. We used, instead of an individual atom, a Co atom surrounded by a phthalocyanine ligand, *i.e.* a Cobalt-Phthalocyanine molecule. By employing individual CoPc molecules that reside on cobalt nanoislands grown on copper, we demonstrate the ability of STM/STS to visualize and explore the spin-polarization of individual molecules. Since this topic was treated elaborately in the thesis of Christian Iacovita [19], only a brief review will be given here.

A CoPc molecule adsorbed on a ferromagnetic island binds to the surface and its magnetic moment couples to the island magnetization. If this coupling is strong enough, the magnetization of the molecule should be blocked in time. As SP-STM/SP-STS does not measure the magnetization of a system, but the spin-polarized conductance, the experiment alone allow concluding neither about the magnetic moment nor about the direction of the magnetization. Nevertheless we are able to gather information about the spin-polarized LDOS around E_F , which is fundamental in view of spintronic applications. To conclude on the magnetic coupling between CoPc and the cobalt surface DFT calculations by Thomas Brumme and Jens Kortus were needed.

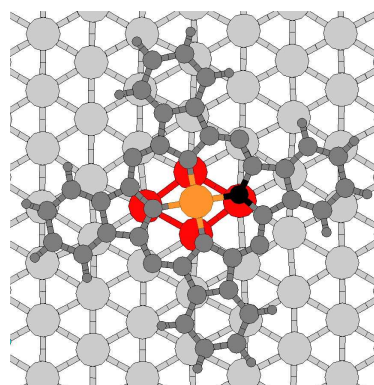


Figure 4.12: Adsorption optimization by DFT. The central cobalt is found in a bridge position while all nitrogen atoms are close to on-top positions.

4.3.1 Adsorption of CoPc on cobalt islands

CoPc molecules, evaporated at room temperature onto the Co/Cu(111) system, adsorb preferentially at cobalt step-edges and on top of the cobalt islands as can be seen in Figure 4.11. At our working coverage¹⁰ the island edges are saturated with CoPc (red), and individual molecules can be seen on top of the islands, no CoPc being observed on the copper surface. The molecules are cognizable by their four-lobe pattern (pale blue in Fig. 4.11). The selective adsorption indicates the enhanced surface reactivity of cobalt compared to Cu(111).

The exact adsorption site of single CoPc molecules on cobalt was determined through first-principles calculations¹¹ based on density functional theory by means of the PWSCF package [162], which was proved correct for CoPc on Cu(111) by STM techniques (see section 4.2.1). Figure 4.12 shows the adsorption geometry with the lowest energy as obtained by geometry optimization, which was tested for different starting geometries with the cobalt atom of CoPc in a top, bridge, and hollow position. Co resides in a bridge position and all nitrogen atoms are close to on-top positions with respect to the surface cobalt atoms. The distance between the central cobalt atom of CoPc and the two closest surface cobalt atoms is 2.5 Å, which is close to the interatomic distances in the surface layer. Even though the position of the benzopyrrole units on cobalt is slightly rotated compared to CoPc on copper, the adsorption site for the two

¹⁰Typical island coverage was 10 molecules per 100 nm² island surface.

¹¹The magnetic surface is mimicked by using a slab model consisting of three Cu layers with two Co layers on top and about 2.2 nm vacuum to the next periodic repeated layer. The CoPc was placed above the Co layers resulting in a 302 atom model. During the geometry optimization, only the Cu atoms were held fixed at their positions according to bulk values, whereas CoPc and the two Co layers were allowed to fully relax.

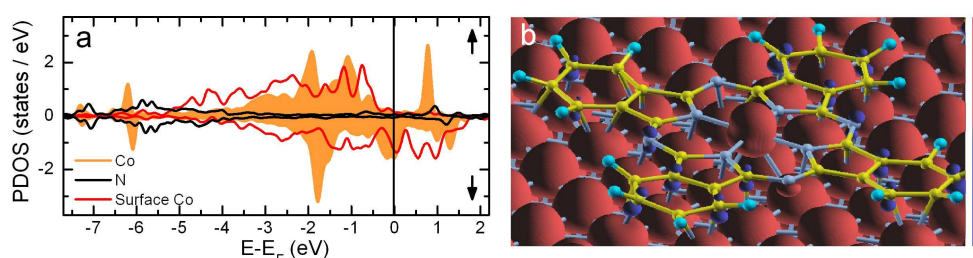


Figure 4.13: a) pDOS over CoPc and the cobalt surface (top panel: majority channel; bottom panel: minority channel). b) Isosurface plot of the magnetization density (\uparrow , magnetization in the "up" direction; \downarrow , "down" direction). The cobalt atom of CoPc and the cobalt atoms of the surface have parallel magnetizations.

surfaces is similar.

Based on the optimized geometry, the LDOS of CoPc on cobalt was calculated. It is found that the hybridization of cobalt surface atoms with nitrogen and with carbon atoms is responsible for the bonding of CoPc to the surface. Furthermore the d_{z^2} orbital of the molecular cobalt (see Fig. 4.2a), unoccupied and just above E_F for the molecule in vacuum, broadens and therefore becomes partially occupied (see Fig. 4.13a), which reduces the magnetic moment from $1 \mu_B$ for the free molecule to $0.7 \mu_B$ for the adsorbed one.

4.3.2 Spin-polarized spectroscopy and conductance maps of single molecules

The spin of the adsorbed CoPc should couple to the island magnetization and we expect this to result in a stationary spin-state of CoPc. This would be proved by SP-STM, if an SP-contrast of the dI/dV signal above a molecule is detected depending on the relative alignment of the island and the tip magnetization. As no external magnetic field is employed here, which could either switch the tip or the island magnetization [6, 187], we searched for two islands with opposite magnetization, which were close to one another. The islands were chosen of same stacking and size not to confuse structural and magnetic effects (see section 2.2.3 for details). Following this approach, the SP dI/dV spectra of molecules residing on islands of opposite magnetization can directly be compared. Differences are then due to the different magnetization alignment with respect to the tip. Figure 4.14a shows the spin-polarized dI/dV spectra of two islands fulfilling all the criteria mentioned above. The dominant d resonance

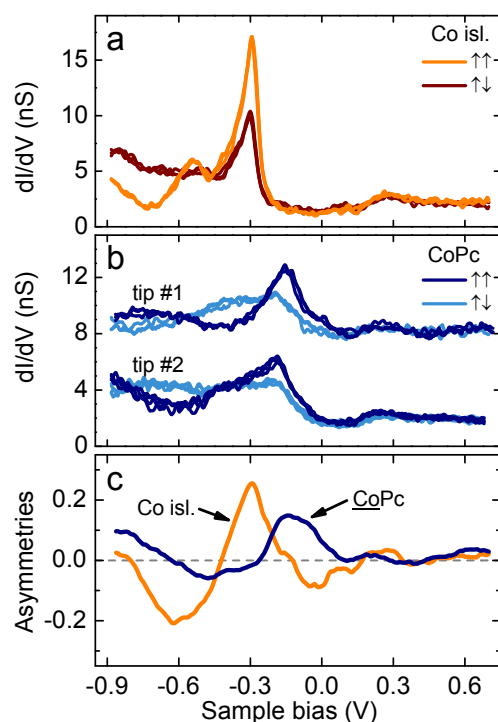


Figure 4.14: Spin-polarized dI/dV above cobalt nanoislands and CoPc. a) Typical spin-polarized spectra over two cobalt nanoislands of opposite magnetization (orange: $\uparrow\uparrow$, brown: $\uparrow\downarrow$, gap conditions: 0.60 V and 0.50 nA). b) SP spectra over the center of single CoPc molecules residing on cobalt nanoislands of opposite magnetization (dark blue: $\uparrow\uparrow$, light blue: $\uparrow\downarrow$, gap conditions: 0.60 V and 0.50 nA). Two sets of spectra acquired with distinct tips (noted #1 and #2) are presented. The spectra acquired with tip #1 are displaced upward by 6 nS for clarity. c) Asymmetries¹² arising from opposite magnetizations: CoPc (dark blue) and Co nanoislands (orange). The asymmetries are an average of all recorded asymmetries obtained with different tips.

at -0.3 V (called P1 in the following) provides a strong SP contrast, identifying the two islands as of opposite magnetization. We define the islands here as either parallel ($\uparrow\uparrow$), or antiparallel ($\uparrow\downarrow$). In a second step, SP dI/dV spectroscopy was acquired above the center of CoPc molecules being adsorbed near the center of the two islands. While the main resonance, which falls at roughly -0.2 V, does not depend on the tip, towards lower biases the spectral shape may change depending on the microscopic tip employed. Therefore Figure 4.14b provides two pairs of representative spectra acquired above CoPc molecules adsorbed on islands of opposite magnetization. Each pair was taken with the same tip. A first observation is the fact that spectra of molecules rising on a $\uparrow\uparrow$ island (called $\uparrow\uparrow$ molecules in the following) are equal,

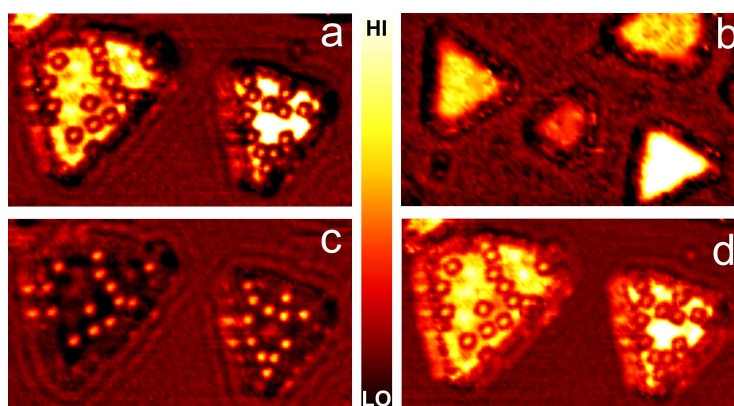


Figure 4.15: Spin-polarized tunneling conductance maps for CoPc. Maps (a), (c), (d) were taken at -0.29 , -0.16 , and -0.32 V respectively (40×20 nm², gap conditions: 0.60 V and 0.50 nA). Each map is normalized to span the same color palette range. b) Spin-polarized map of Co nanoislands at -0.29 V as in (a), in the absence of CoPc molecules (45×25 nm²).

while they differ from the spectra of molecules adsorbed on a $\uparrow\downarrow$ island (called $\uparrow\downarrow$ molecules in the following). Secondly, the prominent resonance at -0.2 V of $\uparrow\uparrow$ molecules is always more intense compared to $\uparrow\downarrow$ CoPc, irrespective of the tip employed. At lower biases differences between $\uparrow\uparrow$ and $\uparrow\downarrow$ molecules are observed as well, but depend on the tip. Contrary to the negative bias range, in the positive bias range, the spectra of the two types of molecules are similar. These results confirm our assumption that CoPc molecules on cobalt islands possess spin-polarized states, which are linked to the magnetization of the island, molecules on opposite islands having opposite spin-polarization themselves. Furthermore islands and molecules present strongly different asymmetries¹² of the dI/dV for opposite species as presented in Figure 4.14c. For example between 0 and -0.2 V, the islands asymmetry is negative, while for the molecules it is positive, or at -0.3 V, the islands asymmetry is maximal, while for CoPc it is close to zero. Hence the spin-polarized signal above CoPc does not only reflect the islands spin-polarized LDOS, but is governed by proper molecular states.

By means of SP dI/dV mapping, this opposite spin-polarization of the molecules can be visualized as presented in Figure 4.15. At a bias of -0.29 V (Fig. 4.15a), the pristine island surface provides a clear contrast between the two islands, which resembles the situation for opposite magnetized islands without CoPc as shown in Figure 4.15b. As -0.29 V is the bias

¹²The asymmetry is defined as $(\uparrow\uparrow - \uparrow\downarrow)/(\uparrow\uparrow + \uparrow\downarrow)$, the arrows referring to a dI/dV acquired on $\uparrow\uparrow$ and $\uparrow\downarrow$ CoPc molecules or islands, respectively.

of P1, the bright island is defined as $\uparrow\uparrow$ while the dim island is called $\uparrow\downarrow$. At this energy the molecules appear more or less with the same intensity on both islands, since their asymmetry is close to zero (*cf.* Fig. 4.14c). But if the differential conductance is mapped at -0.16 V (Fig. 4.15c), molecules on the $\uparrow\uparrow$ island appear clearly brighter than those on the $\uparrow\downarrow$ island while the islands themselves are almost equal in intensity. By mapping at lower biases, *e.g.* at -0.32 V, the contrast between the molecules is inverted. There $\uparrow\uparrow$ CoPc appears dimmer than $\uparrow\downarrow$ CoPc. This is due to a change in sign of the SP asymmetry between the two energies (*cf.* Fig. 4.14c). A closer look at the dI/dV maps reveals that, within the experimental resolution, the SP signal is located in the center of CoPc at and near Co as evidenced by the comparison of profiles of a $\uparrow\uparrow$ and an $\uparrow\downarrow$ molecule in Figure 4.16a. The close-up of an $\uparrow\downarrow$ molecule in Figure 4.16b shows this localization at the core of the molecule. The benzene rings present a lower and, within the experimental resolution, a non-SP conductance.

By means of DFT calculations we can gain insight into the origin of the spin-polarized signal detected by STS. Figure 4.13a presents the spin-dependent partial density of states of selected parts of the CoPc/Co/Cu(111) system. In the bias range of interest between E_F and -1 V, a strong contribution of cobalt is observed for the minority channel, which consists of d states (d_{xz} , d_{yz} and d_{z^2}), while a insignificantly small density of states is observed for the organic ligand (here only the nitrogen pDOS is shown). The cobalt contribution to the majority channel is much weaker, and therefore an SP signal can be detected in STS. The magnetization density was extracted and shown in the isosurface plot in Figure 4.13b. This plot shows the ferromagnetic coupling of the central cobalt ion of CoPc with the surface, both showing an "up" magnetization. Smaller magnetization densities, either "up" or "down" are found at certain carbon or nitrogen atoms, but are very weak compared to cobalt.

The ferromagnetic coupling between the molecule and the Co island arises from a direct Co–Co_{surface} exchange interaction, as well as from an indirect Co–N–Co_{surface} superexchange interaction, in accordance with the interpretation for the coupling of ironporphyrin to a nickel and cobalt thin films [143]. Thus the organic ligand influences the spin-polarized properties of the molecule in two ways. Firstly, the adsorption of CoPc on the island and therefore the position of the central cobalt with respect to the surface atoms is governed by the ligand and determines the direct exchange interaction. Secondly, the indirect superexchange is directly promoted by the ligand nitrogen and influences the molecular magnetization. By means of chemical engineering, *i.e.* by modifying the ligand and therefore the adsorption as well as the magnetic coupling, the spin-polarization above of the adsorbate could be optimized. Comparing the case of CoPc with

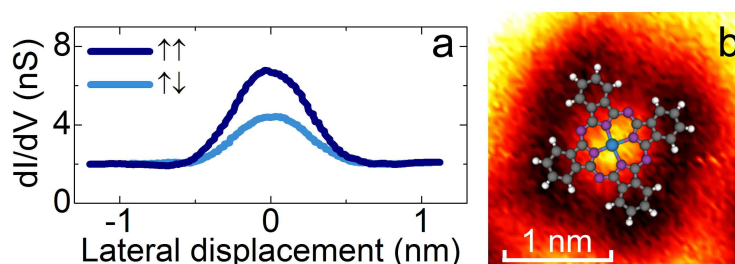


Figure 4.16: Localization of the SP signal at the central Co. a) Profiles of the differential conductance along one axis of CoPc extracted from Fig. 4.15c. Molecules on the $\uparrow\uparrow$ island (right island in Fig. 4.15c) appear higher. b) Map of a $\uparrow\uparrow$ molecule of (Fig. 4.15d) with model molecular structure superimposed ($2.6 \times 2.6 \text{ nm}^2$).

the adsorption of individual atoms, which were studied in chapter 3, some differences become evident. While the polarization above the adatoms is governed by surface-induced states and atomic resonances, for CoPc molecular SP states, mainly Co d states, determine the polarization around E_F . However, the localization of the SP signal in the center of CoPc is a consequence of the dominance of the cobalt contribution to the molecular LDOS in the bias range around E_F , which covers the contributions of the organic ligand. It is not excluded that, with an enhanced experimental resolution, a spin-polarized contrast could be also obtained on the organic ligand. Even for a diamagnetic molecule like H_2Pc , which might be the subject of a future study, an SP signal could be expected, if surface induced states are present on the molecule. The Cu adatom on cobalt islands as treated in chapter 3 provides a good example on how the LDOS above an adsorbate, which possesses a roughly zero magnetic moment,¹³ can possess a strong polarization at E_F [*cf.* Tab. 3.1 and Fig. 3.11 (pages 46 and 49)].

Summary and conclusions

In this chapter we studied CoPc molecules adsorbed on Cu(111) and on magnetic cobalt nanoislands grown on Cu(111). While in the first part of the chapter, an in-depth analysis of CoPc molecules on Cu(111) was carried out experimentally and theoretically, the second part of the chapter was devoted to the direct visualization of the spin state of a single molecule by means of spin-polarized tunnel electrons, the molecule being ferromagnetically coupled to the cobalt is-

¹³DFT calculations predict a magnetic moment of $0.03 \mu\text{B}$ for an individual Cu atom adsorbed on a cobalt island.

lands. An individual molecule showed a spin-filter-like character, which is strongly influenced by the organic ligand, even though the SP signal was centered on the core of the molecule. Firstly, the ferromagnetic interaction, which is predicted between CoPc and the surface, is partly carried by the organic ligands, and secondly, the ligands govern the adsorption geometry of CoPc.

However, the role, played by the organic ligand, is hard to predict. Until now, there are no straightforward rules that allow to foresee the adsorption site and bonding of a molecule on a surface in general. Therefore we tried to show how innovative STM techniques like tip-assisted atom manipulation and constant-height dI/dV can be used to atomically resolve the adsorption site and map the differential conductance with enhanced resolution. CoPc, used for the SP study on cobalt and one of the standard molecules for molecular electronics, was our first choice for the study, but the presented techniques should work for a broad variety of molecules. DFT calculations helped to discern the role of the organic ligand for the adsorption and the different origin of dI/dV signals. The combination of experimental and theoretical techniques allowed us to gain some insight into the complex interplay between adsorption, binding and electronic transport of an organ-metallic molecule adsorbed on a metal surface. The bias dependent appearance of CoPc in STM images can be understood while no indication for molecular distortion is found. Transport calculations were able to reproduce the main trends of the dI/dV maps even though not all features are understood so far. We suppose an influence of surface electron scattering on the differential conductance in the low positive bias region. Further studies are in progress.

The adsorption of CoPc adsorbed on the two (111) surfaces is similar. However, differences in the electronic conductance appear due to the more complex electronic structure of the cobalt substrate compared to copper. And while on copper the molecule becomes nonmagnetic due to a complete occupation of the d_{z^2} state upon adsorption, on cobalt islands, CoPc partially preserves an unpaired spin, even though the magnetic moment is slightly reduced. In future studies the constant-height conductance measurements of CoPc could be extended to CoPc on the magnetic islands. With the enhanced resolution an SP contrast might be found even on the organic ligand. The exchange of the metal-organic CoPc with diamagnetic molecules like H₂Pc could be advantageous for detecting an SP signal on the benzopyrrole legs.

CHAPTER 5

Negative differential resistance in a C₆₀ monolayer

In the following chapter we explore the fullerene C₆₀ adsorbed on cobalt nanoislands, on Cu(111), and on the tip apex by means of STM and STS. Compared to the flat, organometallic CoPc, which was treated in the preceding chapter, C₆₀ is characterized by its pure carbon nature and its spheric structure. Due to this structure not only the adsorption site but also the polar and azimuthal orientation of the buckyball has to be considered. As other fullerenes, C₆₀ molecules are an interesting subject for nanoscience due to a variety of potential technological applications. In the focus of our study lies the occurrence of a negative differential resistance (NDR). To the best of our knowledge, this study constitutes the first experimental observation of an NDR for C₆₀ directly adsorbed on a metal surface. The NDR is shown to originate from a bias-dependent match and mismatch of tip and sample electronic states, *i.e.* from a local orbital matching (LOM), and it is sensitive to the polar orientation of the molecule. Furthermore, by attaching a single C₆₀ to the tip apex, some control over the occurrence of the NDR is gained, because the orientation of the molecule at the tip apex can be modified and different surfaces, such as flat copper, flat cobalt or single adatoms can be used as a counter electrode. Additional insight in the origin of the NDR will be gained by ongoing DFT calculations performed by Werner A. Hofer.¹ Some preliminary results of these calculations are presented in section 5.4.4.

¹Surface Science Research Centre, University of Liverpool

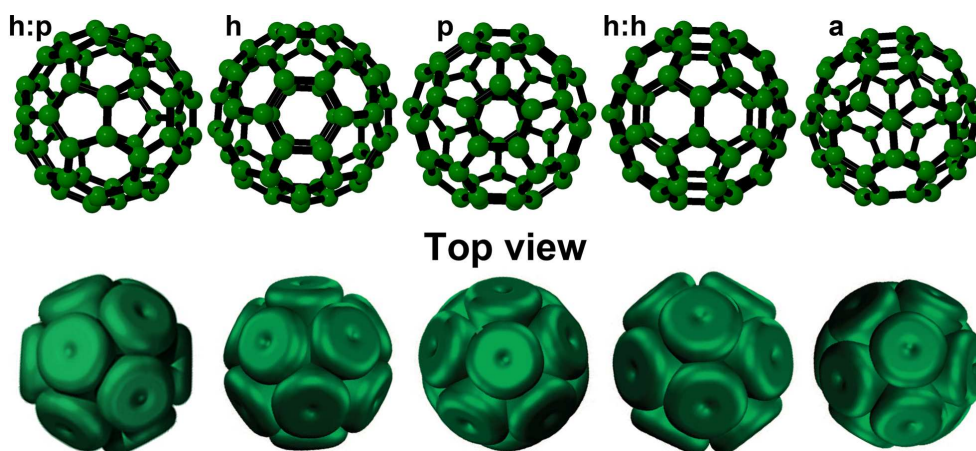


Figure 5.1: C_{60} structure and a LUMO+1 isosurface plot in different orientations, top view. Top row: C_{60} structure with different characteristic structural elements pointing up: a hexagon-pentagon bond (**h:p**), a hexagon ring (**h**), a pentagon ring (**p**), a hexagon-hexagon bond (**h:h**), and an apex atom (**a**). Bottom row: isosurface plots of the LUMO+1 corresponding to the orientations in the top row. Isosurface plots adapted from Refs. [188, 189].

5.1 C_{60} - the buckminsterfullerene

Fullerenes are three-dimensional molecules composed entirely out of carbon and representing a whole group of carbon allotropes beside the long-known allotropes like diamond, graphite or amorphous carbon. Fullerenes are made out of interlinked pentagonal and hexagonal carbon rings. Beside ellipsoidal and cylindric (carbon nanotubes) fullerenes, there is the group of spheric molecules, the so-called buckyballs among which the buckminsterfullerene C_{60} is the most common one.² The 60 carbon atoms of C_{60} form 20 hexagons and 12 pentagons, the pentagons not abutting each other. This results in an icosahedron symmetry (see Fig. 5.1 for a top view of the structure in different orientations) with a nucleus-nucleus diameter of 7.1 Å and a van der Waals diameter of approximately 10 Å. The C–C bond length of roughly 1.4 Å differs depending on the local structure, the bonds between two hexagonal rings being shorter than the pentagon-hexagon bonds. However, all carbon atoms are sp^2 hybridized and bound to three neighboring atoms via σ bonds, while the p_z orbitals form degenerated π orbitals spread over the whole molecular cage (see the bottom row of Fig. 5.1 for the example of the LUMO+1).

After a first theoretical prediction of fullerenes in 1970 by Eiji Osawa [190, 191], in 1985 C_{60} was discovered experimentally by means of mass spectrometry by Kroto *et al.* [192], and named

²IUPAC nomenclature: $(C_{60-I_h})[5,6]$ fullerene

buckminsterfullerene due to a resemblance of the C_{60} structure with the domes created by the architect Richard Buckminster Fuller. Robert F. Curl jr., Sir Harold W. Kroto and Richard E. Smalley, all of them co-authors of the 1985 paper, were awarded the Nobel Prize for chemistry in 1996 for this discovery. Since 1985 a huge variety of fullerenes has been identified and isolated, and they were shown to exist in "nature", for example in ordinary soot, even though in very small quantities.

With the isolation and purification of sizable amounts of C_{60} [193], scientists got the opportunity to study fullerenes and in particular C_{60} adsorbed on surfaces, which is appealing as fullerenes are promising candidates for applications in molecular electronics [194–198], due to their unique electronic properties paired with a high chemical and thermal stability. After a first visualization of C_{60} by means of STM in 1990 [199], and the imaging of well-ordered monolayers on GaAs(110) [200], Hashizume *et al.* could directly visualize the molecular orientation on a Cu(111) substrate and gained insight in the geometry of some of the molecular orbitals (MOs) [201]. Since then a multitude of STM/STS studies on C_{60} adsorbed on different kind of surfaces has been published focusing on adsorption, binding, electronic transport properties, *etc.* [202]. In recent years, several experiments showed that tunnel junctions containing C_{60} can possess regions of negative differential resistance (NDR) [13, 15, 203, 204], which is particularly appealing as NDR is taken for one of the essential elements of molecular electronics [18].

5.2 Negative differential resistance in STS

Negative differential resistance is a phenomenon shown by certain electronic devices: over a finite bias range the current decreases with increasing bias. It was first reported for a germanium tunneling diode by Leo Esaki in 1958 [205], and has been intensively studied thereafter [206–210]. Nowadays semiconductor devices based on NDR are widely used in electronics [211, 212], *e.g.* as fast switches, oscillators, or in frequency-locking circuits. The last two decades have seen a renewed interest of surface scientists in NDR [13–16, 18, 154, 203, 213–231], due to its importance for molecular electronics [18]. The first NDR measurements by means of STM were reported in 1989 for boron-doped [232], and boron-exposed Si(111) [233], respectively. Since then, a multitude of STM-related experiments focusing on a vast variety of systems has been published [13–16, 154, 203, 204, 218–229]. This covers studies on self assembled monolayers (SAM) on metal substrates, which show an NDR when being contacted with the STM tip [203,

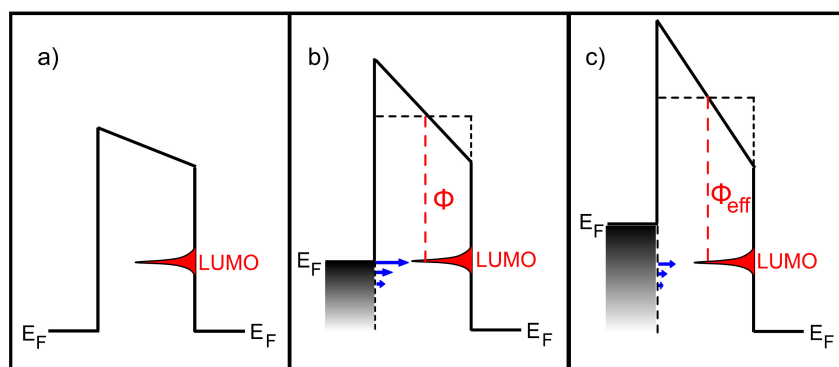


Figure 5.2: Tunneling barrier dependent NDR for the case of a flat tip DOS and a sharp LUMO without background DOS. a) Tunneling barrier without applied bias voltage. b) Tunneling barrier with applied voltage, such that the MO is aligned with the Fermi level of the tip. Tunneling into the LUMO occurs with a tunneling barrier height Φ . c) For higher biases, tunneling from tip states near the Fermi level is inhibited due to the zero DOS at the sample for corresponding energies. The effective tunneling barrier Φ_{eff} for electrons tunneling into the LUMO is higher than in (b) leading to a decrease in tunneling current and hence an NDR. Figure adapted from Ref. [228].

220–222], as well as STS measurements, *e.g.* on carbon nanotubes, which possess a defect induced NDR [223]. Individual molecules [224], and atoms adsorbed on semiconductors [225], as well as on metals [226,227], or molecules residing on an insulating overlayer on a metal [13, 16, 154, 204], were explored.

Three types of NDR can be identified in STM experiments. First, current induced changes in the junction, like charging [213, 214, 230], or conformation changes [226, 227], can lead to a sudden decrease in current. Second, the bias-dependence of the tunneling barrier of the STM junction can cause an NDR, this type attracting some attention in recent years [13, 15, 16, 154, 204, 228]. Figure 5.2 presents a scheme of an STM tunnel junction where such an NDR occurs. In Figure 5.2b the applied sample bias aligns the LUMO of the sample and the Fermi level of the tip, which yields an increasing tunneling current. The tunneling barrier for electrons tunneling into the LUMO equals Φ . When increasing the bias further (Figure 5.2c), tunneling from tip states at E_F is inhibited, as the corresponding sample DOS is zero. At the same time, the effective tunneling barrier Φ_{eff} for electrons tunneling into the LUMO is larger than in Figure 5.2b. This increase of the effective barrier height decreases the current and leads to an NDR. As the barrier-height depends on the tip-sample distance, the NDR becomes more

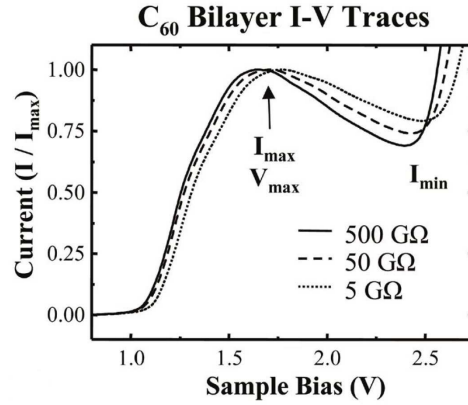


Figure 5.3: Height dependence of barrier-dependent NDR. $I - V$ curves acquired at three different tunnel junction resistances on the C_{60} bilayer. Each curve is normalized to the respective local current maximum (I_{max}) located at $1.5 V < V_{max} < 2.0 V$. Feedback opened: 2.5 V and 5, 50, and 500 pA, respectively. With increasing gap resistance, *i.e.* with increasing tip-sample distance, the NDR peak-to-valley ratio increases as well. Figure adapted from Ref. [13].

pronounced with an increased distance between tip and sample [234], as shown in Figure 5.3 for the case of a doublelayer of C_{60} . One ingredient is mandatory in this scenario: the DOS must possess narrow states (their line-width being smaller than the separation between two peaks), with an amplitude substantially stronger than the background. To fulfill such a condition, the molecules are lifted from the substrate by means of a supporting organic network [15, 228], or by introducing an insulating layer of salt [16, 154, 204], or a molecular layer [13], between the molecule and the metal substrate. For molecules directly adsorbed on metal substrates, the orbitals are broadened due to the coupling with the substrate and a background DOS is present. With increasing bias, states at energies above the MO become available and tunneling into these states compensates the decrease in current due to the increased barrier height; no NDR is observed [13].

The third cause for NDR in STS was first observed by Lyo and Avouris in 1989 [232], who showed for the case of a doped semiconductor that the convolution of energetically localized tip and sample states can yield an NDR [232]. For a simulation of the NDR they modeled the tunneling current within a 1D WKB model:

$$I_t \propto \int_0^{eV} \rho_t(E - eV) \rho_s(E) T(E) dE, \quad (5.1)$$

where $\rho_t(E - eV)$ and $\rho_s(E)$ are the energy-dependent tip and sample DOS, respectively, and $T(E)$ is the energy-dependent transmission factor. By doing so, it was shown that the existence of an occupied state at one electrode and of an unoccupied state at the other electrode is sufficient to produce an NDR, if the two states are localized in energy and the background DOS is low [232]. Chen *et al.* extended this model for CoPc molecules on Au(111) by introducing $T(E) = |M_{st}|^2$, where M_{st} is the tunneling matrix element [14]. Their model accounted for changes of the transmission depending on the states involved in tunneling [235]. Recently a theoretical study by Shi *et al.* predicted the existence of an NDR on a C₆₀ monolayer directly adsorbed on a metal surface. This NDR is based on the convolution of tip and sample states, *i.e.* on an energy-dependent local orbital matching (LOM) [17]. Different tungsten tips were shown to produce an NDR above selected sites of C₆₀ molecules adsorbed on Cu(111). Below, we present, to the best of our knowledge, the first experimental observation of an NDR for C₆₀ directly adsorbed on a metal surface, which originates from an energy-dependent match and mismatch of tip and sample states, *i.e.* an LOM. By testing different substrates and molecular orientations as well as by "inverted STM" experiments [236], insight is gained in the restrictive parameters for the observation of an NDR.

5.3 C₆₀ adsorption on cobalt islands and on Cu(111)

The Co/Cu(111) system provides the opportunity to study C₆₀ at the same time on different (111) surfaces (cobalt islands and copper) and in different orientations as shown below. Before investigating the electronic properties of the system, we want to explore the adsorption geometry of C₆₀ for this system. In our experiment double-sublimated C₆₀ was evaporated onto the Co/Cu(111) sample immediately after cobalt deposition and just before transferring the sample into the pre-cooled STM. Extreme care was taken to keep the sample at room temperature during the cobalt and C₆₀ deposition to avoid intermixing between cobalt and copper. Figure 5.4a presents a topograph of C₆₀ adsorbed on cobalt islands and copper with our typical working coverage of 0.15 ML.³ Neither islands nor copper showed an increase of the impurity level upon C₆₀ deposition. The dI/dV above cobalt, which is highly sensitive to impurities [237], remained unchanged compared to a sample preparation without molecule deposition.

Five orientations of C₆₀ on surfaces are possible: C₆₀ adsorbed with a hexagonal (**h**) or a

³One monolayer corresponds to a density of 110 molecules per 100 nm². At this coverage, no preferential adsorption on either of the two surfaces was found.



Figure 5.4: Topographic image of C_{60} molecules adsorbed around and on top of cobalt nanoislands residing on Cu(111). a) Two cobalt islands and the copper surface are partially covered with a C_{60} monolayer ($70 \times 30 \text{ nm}^2$, -0.8 V , 0.1 nA). b) Close-up on cobalt: C_{60} adsorbs on an apex atom tilted towards a hexagonal ring ($2.7 \times 2.8 \text{ nm}^2$, 2.1 V , 2 nA). c) Close-up on copper: C_{60} adsorbs preferentially on a hexagonal ring ($2.7 \times 2.8 \text{ nm}^2$, 2.1 V , 1 nA).

pentagonal (**p**) ring parallel to the surface, C_{60} adsorbed on a bond between a hexagonal and a pentagonal ring (**h:p**), on a bond between two hexagonal rings (**h:h**), or on an apex atom (**a**) [see Fig. 5.1 for the different orientations] [238]. However, slight tilts of the orientations are also possible [239]. Due to the C_{60} symmetry, the molecular structure in contact with the substrate is similar to the one on the top of the molecule pointing into vacuum (*cf.* Fig. 5.1), which is visualized by STM. Different adsorption geometries can be identified by means of the imaged orbital symmetry of molecular states [201, 240], in particular of the LUMO+1. This orbital has a ring-like structure above the pentagonal rings (see bottom row of Fig 5.1).

On copper, roughly 90% of the molecules adsorb **h**, which is in good agreement with previous studies on C_{60} deposited onto Cu(111) at room temperature [241]. The molecules possess the typical trefoil shape, but appear slightly tilted, *i.e.* one protrusion being brighter than the other two (see Fig. 5.4c and the constant-height current image in the inset of Fig. 5.14), which has been observed previously on Cu(111) [241]. It is known from literature that further annealing or deposition at higher temperatures would lead to the same orientation in even higher ordered films [201], but a reconstruction of the underlying copper surface [242], and an altered bonding and charge transfer between C_{60} and the surface would be induced simultaneously [243]. We desisted from any annealing, as this activates the intermixing between cobalt and copper [see section 2.2.1 (page 19) for details].

Contrary to copper, on the cobalt islands more than 95% of the molecules adsorb in the same configuration. Figure 5.1b shows a close-up of a monolayer on cobalt at $+2.1 \text{ V}$, a bias

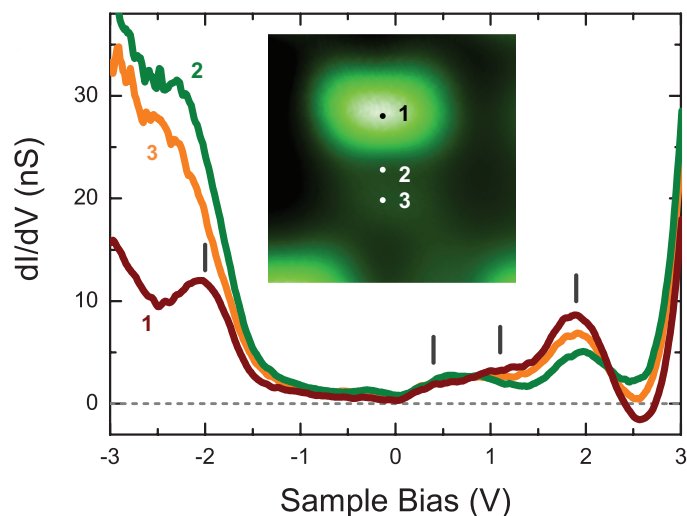


Figure 5.5: dI/dV over C_{60} on cobalt islands on Cu(111). Feedback opened at 1.0 V and 2.0 nA. Spectra labeled 1, 2 and 3 are acquired with the tip positioned over the spots indicated in the inset, which shows a constant-height current map of C_{60} on a cobalt island (bias: 1.9 V, size: $11.5 \times 11.5 \text{ \AA}^2$). Vertical lines indicate the fitted energetic positions of HOMO, $LUMO_{\alpha}$, $LUMO_{\beta}$ and $LUMO+1$.

just above the $LUMO+1$. All molecules appear as an elongated, oval protrusion with a second, but weak protrusion at one site. This hints at an *a* adsorption (*cf.* Fig 5.1), as confirmed by DFT geometry optimization by Werner Hofer predicting an adsorption on an apex carbon atom slightly turned towards a hexagon. On rare occasions, differently oriented molecules are found, these usually being isolated molecules.⁴ After the determination of the adsorption on the two (111) surfaces, we can now explore the electronic properties of these systems, focusing on the occurrence of an NDR.

5.4 C_{60} on cobalt - observing an NDR

5.4.1 Differential conductance

Figure 5.5 presents dI/dV spectra acquired above three different spots of the molecule as indicated in the inset. The HOMO derived state is detected at -2 V, the $LUMO+1$ is found at

⁴These molecules could be trapped by structural defects or impurities on the islands. Therefore we do not further explore their electronic structure.

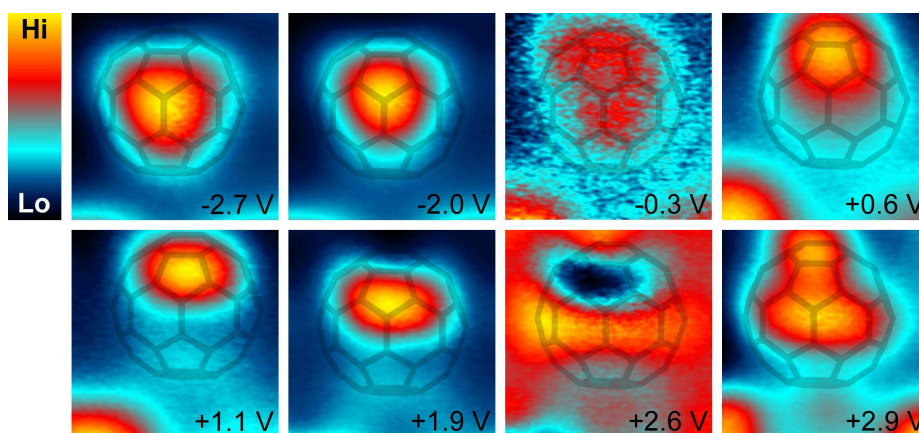


Figure 5.6: Differential conductance at a constant height. dI/dV maps of C_{60} adsorbed on a cobalt island. Sample bias as indicated in each map. Map size: $10 \times 10 \text{ \AA}^2$. As guide for the eye a C_{60} model is superimposed on each map in accordance with the DFT-determined orientation. The color code was normalized for each map in order to achieve a better contrast. All dI/dV signals have positive values, except for the map at $+2.6 \text{ V}$, where the lowest conductance (dark blue) corresponds to negative values.

1.9 V and the LUMO shows a splitting [241,244,245], two peaks were fitted to $+0.6 \pm 0.1 \text{ V}$ and $+1.2 \pm 0.1 \text{ V}$, called $LUMO\alpha$ and $LUMO\beta$ in the following. Typical peak widths are between 550 and 750 mV . For biases above the $LUMO+1$ the spectrum labeled 1 in Fig. 5.5 shows an intriguing behavior: while the $LUMO+1$ peak is more intense compared to the other spectra, behind the peak, *i.e.* at higher biases, the dI/dV decreases and becomes negative, reaching a minimal differential conductance of -1.6 nS at $+2.6 \text{ V}$ before increasing again towards the $LUMO+2$. It should be mentioned, that this NDR could not be detected with all tips employed. One out of three sharp tips that showed an excellent intramolecular resolution in topography (like in Figs. 5.4b and c) and a structureless dI/dV above $Cu(111)$ like the one shown in Fig. 2.3 (page 17), allowed for the detection of an NDR. As all tips were treated elaborately by indentations into the copper surface, a tip apex covered with copper is expected.

As observed in the spectra, the relative intensities in the dI/dV vary considerably over the molecule, the orbitals being distributed inhomogeneously over the molecular cage. To localize the NDR and the different MOs above the C_{60} cage, constant-height dI/dV maps were recorded. After opening the feedback above C_{60} at given gap conditions, the area above a molecule was scanned keeping the tip at a constant height while recording the dI/dV signal at each pixel for a chosen bias. Figure 5.6 presents the so acquired maps for different biases.

The contrast in the maps was adjusted for each map so to cover the whole color palette, as the differences in the dI/dV intensities between different maps are enormous (*cf.* dI/dV spectra of Fig. 5.5). For each map the highest conductance value was set to yellow, while the smallest value was set dark-blue. At -2.7 V, which can be interpreted as the onset of the HOMO -1 , the signal maximum is located on the bond between the two hexagon rings ($h:h$ bond) on top of the molecule, leading to a triangular shape, which is conserved when moving to the HOMO at -2.0 V, the maximum now being located above the carbon atom. At -0.3 V, still a triangular shape is found, even though the conductance is low (*cf.* the signal-to-noise ratio is lower compared to the other maps), as no MO is present at this energy.

In the positive bias regime, the observed spatial distribution of the dI/dV is less indicative for some of the orbitals. While the map at $+2.9$ V (the onset of the LUMO $+2$) shows high conductance above different hexagon rings and the LUMO $+1$ ($+1.9$ V) is, as expected, located above the pentagon, the two LUMO derived states LUMO α and LUMO β are harder to localize. The LUMO β at $+1.1$ V is observed above the pentagon, but shifted with respect to the LUMO $+1$. A localization of this state above the pentagon ring is reported in some cases [241]. The LUMO α at $+0.6$ V is observed even further displaced, probably indicating localization above selected bonds of the molecular cage. However, due to the curvature of the C₆₀ cage, the tip-molecule distance is different at different positions above the molecule, making an unambiguous determination difficult.

To spatially localize the observed NDR, we acquired a dI/dV map at $+2.6$ V. In this case, the smallest differential conductance has a negative value, the dark-blue area corresponding to a negative dI/dV signal. This zone is located above the pentagon in the region, where the LUMO $+1$ has its highest intensity too. By moving the tip across the molecule we merely change the amplitude of the molecular states in the LDOS. As we will show below, this change in amplitude is the determining parameter for the observation of the NDR.

5.4.2 The role of the tip-sample distance

To explore the NDR, in a first test, we changed the tip-sample distance and studied changes of the NDR. Figure 5.7 presents four $I - V$ characteristics, *i.e.* the tunneling current measured as a function of the sample bias [$I(V)$], acquired at different tip-sample distances.⁵ The $I - V$

⁵The feedback was opened with gap conditions corresponding to a resistance of 400 G Ω , 40 G Ω , 4 G Ω and 0.4 G Ω , respectively, which equals in tunneling regime an approximate change in the tip-sample distance of

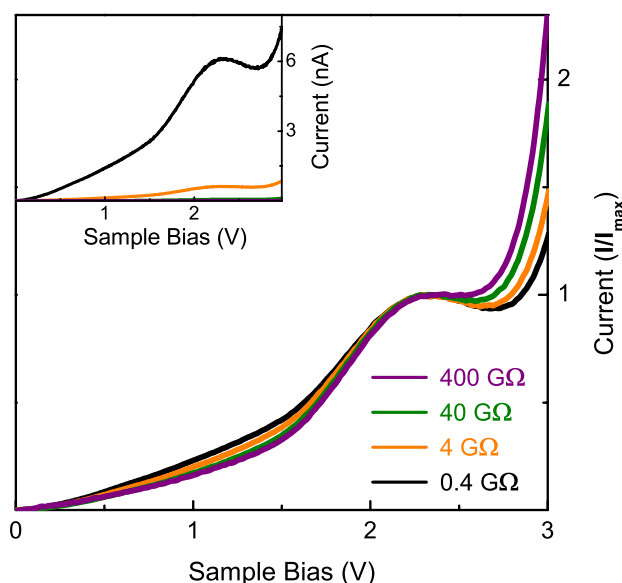


Figure 5.7: Height-dependent current-voltage characteristics. $I(V)$ spectra above C_{60} on cobalt acquired with different gap conditions. The feedback was opened at +2 V and 5 pA (400 G Ω), 50 pA (40 G Ω), 500 pA (4 G Ω) and 5 nA (0.4 G Ω), respectively. Each spectrum was acquired above the spot labeled 1 in the inset of Fig. 5.5, always testing different molecules. The curves are normalized with respect to the current value at the local maximum. The inset shows the raw $I - V$ characteristics. The NDR, *i.e.* the peak-valley ratio, decreases with increasing tip-sample distance and vanishes completely for the highest distance measured (400 G Ω).

curves are normalized with respect to the local maximum of the current. In contrast to an NDR originating from the bias-dependence of the barrier-height (Fig. 5.3), we observe the most pronounced NDR for the smallest tip-sample distance at a gap resistance of 0.4 G Ω (black curve in Fig. 5.7). With increasing tip-sample distance, *i.e.* with increasing gap resistance, the peak-valley ratio of the NDR decreases and finally vanishes for the largest distance (400 G Ω gap resistance). This definitely excludes the bias dependency of the barrier-height as the origin of the observed NDR, which is not surprising, since the molecule is coupled to a metallic surface leading to broad peaks and non negligible background DOS. Our widths are typically 550 to 750 mV, whereas widths of 300 mV and below are observed in decoupled layers [15, 16, 154]. We therefore conclude that the observed NDR originates from an LOM. To gain some insight in the limiting parameters for the LOM mechanism, we simulated dI/dV curves based on the

2.7 Å (*cf.* Fig. 5.15a). Extreme care was taken to acquire the spectra for different distances always above the same spot on the molecule. Several molecules were tested, all showing a similar behavior.

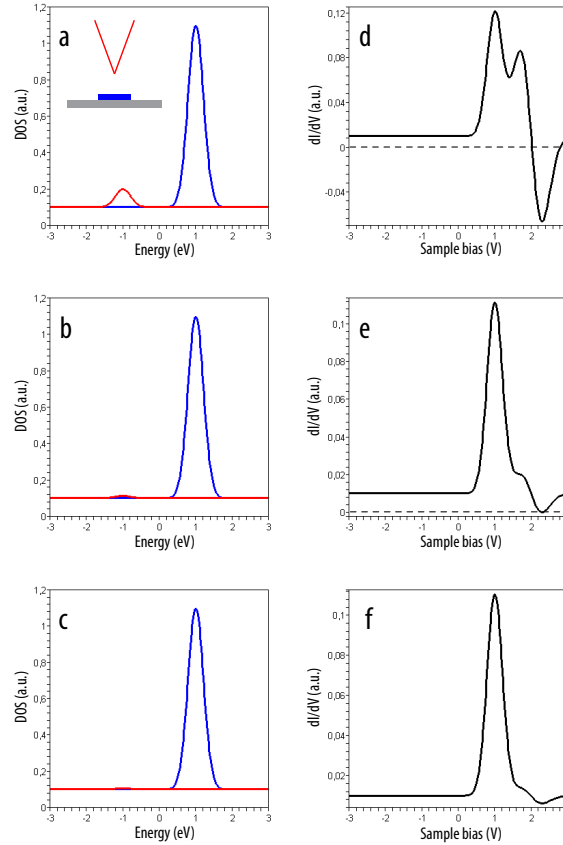


Figure 5.8: Simulated dI/dV spectra for one localized state at each electrode. a–c) tip (red) and sample (blue) DOS. The background is set to 0.1 for tip and sample, the peak width is 0.5, the sample state amplitude is 1. The tip state amplitude is 0.1 (a), 0.013 (b), or 0.005 (c), respectively. d–f) simulated dI/dV spectra for the DOS of (a), (b), or (c), respectively. The inset in (a) shows the simulation setup: STM tip (red) above a surface object (blue).

WKB approximation as shown below.

5.4.3 Simple model for the local orbital matching

From the simulations by Lyo and Avouris [232], we know that, the stronger the intensity of the peaks, the higher is the probability for an NDR to occur. Additionally, the two states should be of comparable width to lead to a good match. However, the influence of the ratio between the peak amplitude and the background, the impact of the energetic position of the peaks or of their distance remains unclear. Following Lyo and Avouris (cf. Eq. 5.1), we use a WKB-based

approach. In a rough approximation we keep T constant and can now write the tunneling current as:

$$I \propto \int_0^{eV} \rho_t(E - eV) \rho_s(E) dE. \quad (5.2)$$

I depends now only on the energy-dependent tip and sample DOS $\rho_t(E - eV)$ and $\rho_s(E)$, respectively. The numerical integration for the model tip and sample DOS then leads to $I - V$ characteristics, which can be differentiated in order to obtain a dI/dV .⁶ We also carried out simulations considering $T(eV)$. An apparent barrier height of $\bar{\Phi} = 6$ eV was determined using Eq. 1.3 (page 4) and the $I(z)$ in Fig. 5.15a [238]. No appreciable change of the calculated dI/dVs was observed. However, the adaptability of a 1D description of $T(\Phi, z)$ in the WKB approximation for the case of molecular samples is still under discussion [234].

To model a molecular state in the sample DOS (C_{60}) we used Gaussian peaks of amplitude $A_s = 1$ and width $w_s = 0.5$ eV, the background was set to $B_s = 0.1$. The structured tip DOS was modeled with a single Gaussian peak of width $w_t = 0.5$ eV and a background of $B_t = 0.1$. The amplitude A_t was set to 0.1, except for the first set of simulations, where it was varied from 0.1 to 0.005.

Figure 5.8 shows selected examples for the simplest scenario possible as also treated by Lyo and Avouris [232], the convolution of one single sample state with one tip state, but we additionally varied the amplitude of the tip state. The result should give an idea of the tip structure intensity needed to cause an NDR when combined with a C_{60} . In the simulations, for a tip state of the same amplitude as the background, a pronounced NDR is observed (Fig. 5.8d), while for an amplitude of 5% of the background, no NDR appears (Fig. 5.8f). In this specific case, an amplitude of the tip state of 13% constitutes the threshold value for an NDR (Fig. 5.8e). For this simplified scenario we can conclude:

$$\text{If } \frac{A_s A_t}{B_s B_t} \gg 1 \quad \text{and} \quad \frac{w_s}{w_t} \approx 1, \text{ an NDR occurs.}$$

To approach a more general situation, we now add a second state to the sample DOS, which corresponds to two unoccupied MOs, for instance the LUMO and the LUMO+1. In a first set of simulations, we varied the energy interval $V_{s2} - V_{s1}$ between the two sample states and explored the impact on the NDR between the two resonances. Some selected examples are

⁶Eq. 5.2 presents a Volterra integral equation of the first kind that does not have a simple analytical solution [234].

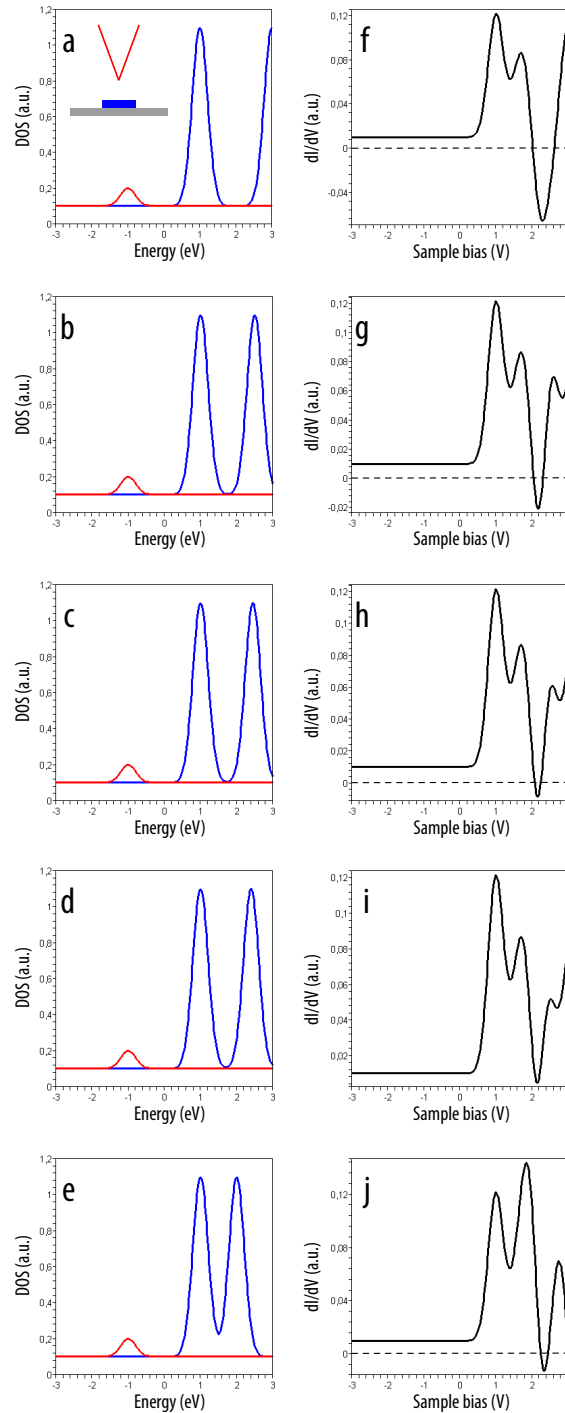


Figure 5.9: NDR as a function of the energy interval between two sample states. a–e) tip (red) and sample (blue) DOS (background: 0.1, peak width: 0.5, sample state amplitude: 1, tip state amplitude: 0.1). The interval $V_{s2} - V_{s1}$ between the sample states is varied: 2 eV (a), 1.5 eV (b), 1.45 eV (c), 1.4 eV (d), 1 eV (e). f–j) simulated dI/dV spectra for the DOS of (a)–(e). The inset in (a) shows the simulation setup: STM tip (red) above a surface object (blue).

shown in Figure 5.9. Starting with an energy interval $V_{s2} - V_{s1} = 2$ eV (Fig. 5.9a), where an NDR is observed in the corresponding dI/dV (Fig. 5.9f), we reduce the energy interval between the two states progressively. A reduction of the NDR is observed (Fig. 5.9g and h), and finally the NDR vanishes (Fig. 5.9i and j).⁷ Remarkably a reduction of the energy interval of 100 meV between Figs. 5.9g and 5.9i is sufficient to suppress the NDR.

Finally, we studied the influence of the energetic position of the tip state V_t on the NDR between two states (Fig. 5.9). Starting with the same configuration as in Fig. 5.9e, *i.e.* $V_{s2} - V_{s1} = 1$ eV and $V_t = -1$ eV, we progressively shift the tip state towards E_F , which corresponds to a change of the tip nature. For $V_{s2} - V_{s1} = |V_t|$, no NDR is observed (Fig. 5.10f). Decreasing V_t to -0.6 eV alters the peak shape in the dI/dV (Fig. 5.10g and h). For $V_t = -0.5$ eV (Fig. 5.10i), an NDR appears and is amplified for $V_t = -0.1$ eV (Fig. 5.10j). As a rule of thumb, we can state:

$$\text{If } (V_{s2} - V_{s1}) - \frac{w_{s2} + w_{s1}}{2} \geq |V_t|, \text{ an NDR occurs.}$$

To conclude, one can identify three main factors favoring an NDR:

1. the peak intensities should be high compared to the background
2. the peaks of tip and sample should be isolated
3. the peak position of the occupied state (here the tip) should be close to E_F

A second, more general, and well-known effect, is illustrated by the simulations: the position, width and shape of sample resonances in the dI/dV are sensitive to the convolution [21,246]. Even though our examples overvalue the amplitude of the tip state to better illustrate the different influences, this holds true for more realistic simulations (see Fig. 5.18) and should be taken into account, when interpreting dI/dV spectra in terms of bonding, screening *etc.* (*cf.* shift of the LUMO+1 peak in Fig. 5.5).

5.4.4 Tunneling conductance by DFT

Above, we could show how the simple convolution of a structured tip DOS with states in the sample DOS can produce an NDR. To validate this scenario for C_{60} on cobalt, in this section

⁷Note that the NDR in Fig. 5.9j does not appear in between the two states, but follows the second peak.

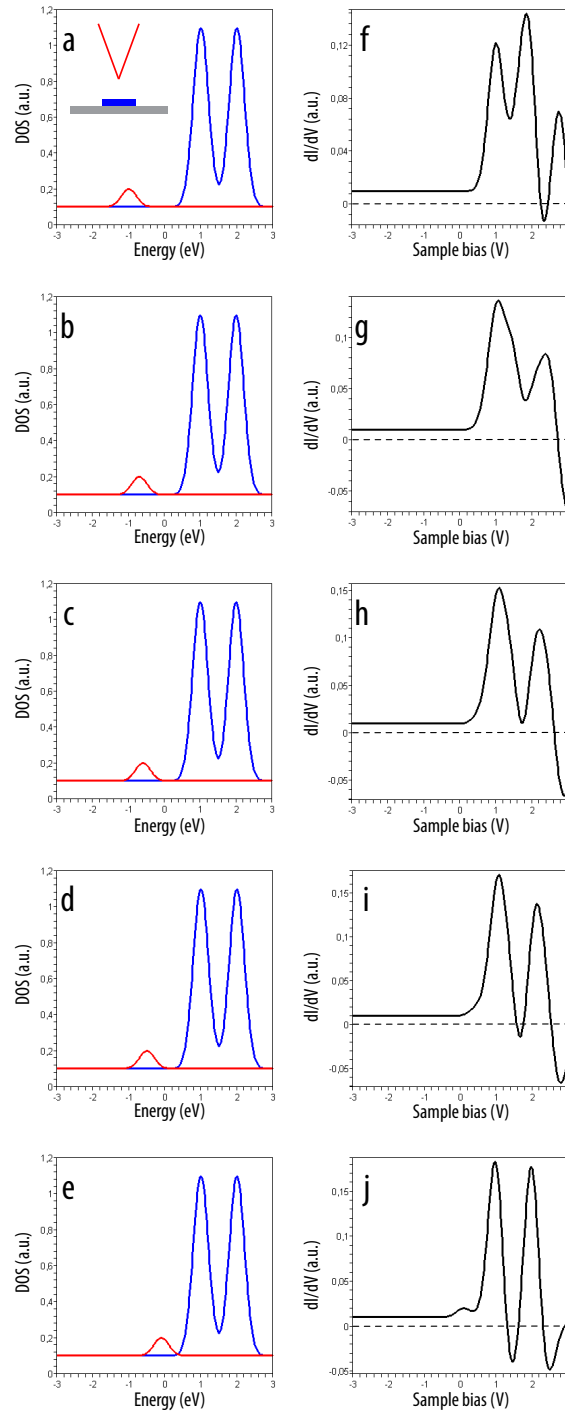


Figure 5.10: NDR as a function of the energetic position of the tip state. a–e) tip (red) and sample (blue) DOS (background: 0.1, peak width: 0.5, sample state amplitude: 1, tip state amplitude: 0.1, sample state distance: 1). The energetic position of the occupied tip state V_t is varied: -1 eV (a), -0.7 eV (b), -0.6 eV (c), -0.5 eV (d), -0.1 eV (e). f–j) simulated dI/dV spectra for the DOS of (a)–(e). The inset in (a) shows the simulation setup: STM tip (red) above a surface object (blue).

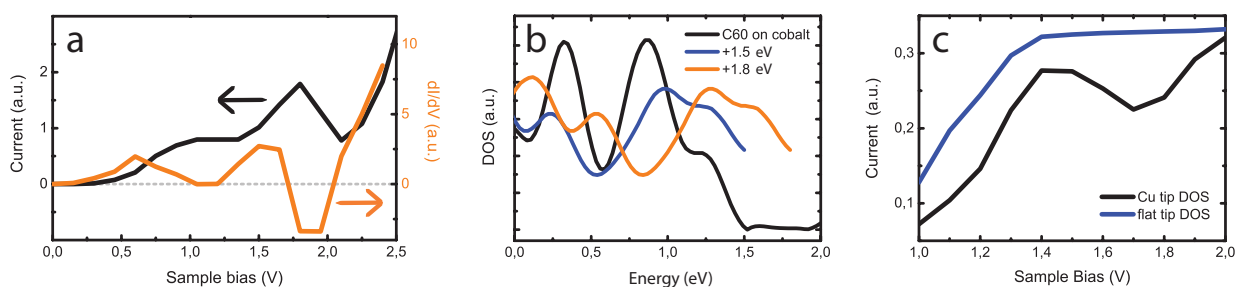


Figure 5.11: Conductance of C_{60} adsorbed on Co islands as calculated by DFT. a) $I(V)$ and $dI/dV(V)$ as calculated by means of full transport calculations. b) DOS of the tip and the sample. The tip DOS is shifted +1.5 and +1.8 V, respectively, with respect to E_F . The energetic overlap of the tip and the sample DOS depends on the applied bias. c) $I(V)$ as calculated from a simple convolution of the tip and the sample DOS. The calculated DOS as shown in (b) leads to an NDR (black curve), while with a flat tip DOS a continuous increase of the current is observed (blue line).

we present calculations of the electron transport in a realistic STM junction by means of DFT performed by Werner Hofer.¹ In a first step, the adsorption site of C_{60} on cobalt was determined (see section 5.3). The second step consisted in modeling the whole STM junction including a model copper tip⁸ at a distance above the sample that corresponds to the experimental conditions. In a final effort, the bias-dependent conductance as well as the DOS have been calculated, the results being presented in Fig. 5.11. Figure 5.11a shows the $I(V)$ [black] and its derivative, *i.e.* the $dI/dV(V)$ [orange], as calculated by means of full transport calculations. The tip was placed above the pentagon as for the experimental spectrum 1 in Fig. 5.5. In agreement with the experiment, a reduction of the current and therefore an NDR is found at energies just above the LUMO+1.

Figure 5.11b shows the DOS of the C_{60}/Co system and of the tip. The tip presents a mixture of d and s states between E_F and -0.5 eV, while the sample shows peaks of the LUMO and LUMO+1. In order to establish the origin of the NDR, the tip DOS is shifted in bias, while the sample DOS remains unshifted, to mimic the overlap of the occupied tip states with the unoccupied sample DOS at different sample biases, here shown for +1.5 V (blue) and +1.8 V (orange), respectively. For +1.5 V, sample and tip states match, while at +1.8 V a mismatch is established. In an LOM framework, this reduces the current when sweeping the bias from +1.5 V to +1.8 V. A simple convolution of the tip and sample DOS, which does not

⁸The tip was modeled as a copper pyramid, terminated by a square of four Cu atoms.

account for any transmission probabilities, already exhibits an NDR (Fig. 5.11c), while no NDR occurs for a flat and energy-independent tip DOS (blue line). This confirms that the NDR we observe is related to an LOM mechanism, the transmission playing a minor role.

If we go back to Fig. 5.7, we can now understand the observed height-dependence of the NDR. The tip DOS is composed of s and d structures and a background DOS, mainly composed of s states. The transmission probability varies differently with distance for s , p and d states [235]. When increasing the tip-sample distance, the d contributions decay faster than the s contributions. Therefore, with increasing distance, the NDR decreases, since the d structure in the tip DOS is reduced compared to the s background DOS. If one compares the situation to the case of dI/dV spectroscopy above Cu(111), it appears that these d structures will contribute to the spectrum above C₆₀ but not above Cu(111), since for similar tunneling conditions, the tip-sample distance on copper is at least 3 Å larger than on C₆₀. This explains the absence of the tip signature in the dI/dV above Cu(111) [*cf.* Fig. 2.3]. To estimate the difference of 3 Å for the tip-sample distance, it is sufficient to remark that the apparent height of C₆₀ compared to Cu(111) is around 7 Å, while the actual height is approximately 10 Å (nucleus-nucleus diameter of C₆₀ of 7 Å plus a C₆₀–Cu distance of 3 Å as calculated by DFT).⁹

5.5 C₆₀ on Cu(111) - weakening the NDR

By means of a simplified WKB-based model we could identify the limiting parameters for an LOM-based NDR. DFT calculations then helped to establish an LOM mechanism for C₆₀ on cobalt. In the following, we adsorb C₆₀ on Cu(111) to modify the NDR. By changing the substrate, we simultaneously change two parameters of the LDOS above the molecule, *i.e.* the energetic position and the amplitude of the MOs. Moreover, the relative intensities of the MOs can also be altered by the orientation of the molecule on the substrate, as we will establish below. As the NDR is a tip-dependent phenomenon, only tips, that showed an NDR for molecules on cobalt, were employed to study molecules adsorbed on Cu(111). Changes in the dI/dV for C₆₀ on copper can then unambiguously be attributed to changes of the sample LDOS.

⁹Additionally to the reduced amplitude of the d states at larger distances, the barrier height of $\Phi \approx 4$ eV for the case of copper is smaller than for C₆₀ ($\Phi \approx 6$ eV). This increases the bias dependence of the transmission factor T for copper compared to C₆₀ and reduces the tunneling for states below E_F .

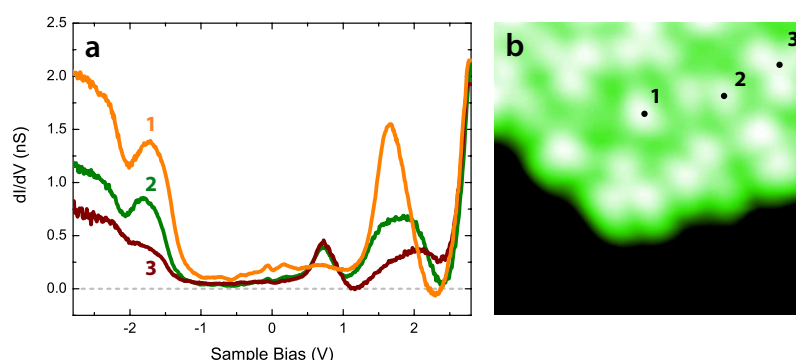


Figure 5.12: Different orientations of C_{60} on Cu(111). a) dI/dV of differently-oriented C_{60} . Feedback opened at 1.0 V and 0.2 nA. Spectrum 1 is acquired above a C_{60} adsorbed with a similar orientation as on cobalt, spectrum 2 above a C_{60} adsorbed **h:h**, spectrum 3 above a molecule with the standard **h** adsorption. The exact tip positions are marked in (b) accordingly. Spectrum 1 shows a NDR between LUMO+1 and LUMO+2, even though it is weaker than on cobalt. **h:h** and **h** adsorbed molecules show a LUMO at 0.7 V. For the **a** adsorption, no clear LUMO peak was found, while a fit supposing a split LUMO α and LUMO β yields energy positions of 0.1 and 0.7 V. b) Topograph of the zone, where the spectra shown in (a) were acquired (size: $4.0 \times 3.8 \text{ nm}^2$, gap conditions: 1.9 V, 0.2 nA).

5.5.1 dI/dV as function of the molecular orientation

Approximately 90% of the C_{60} molecules are adsorbed **h** and 10% are adsorbed in other orientations, such as **h:h** and **a**. The dI/dV acquired above molecules of the three different orientations are shown in Figure 5.12a. We find the HOMO to fall at -1.7 V for **h** and **h:h** and even slightly higher in energy at -1.6 V for **a**. The LUMO+1 is found at 2.0 (**h**), 1.8 (**h:h**) and 1.7 V (**a**), respectively. While for the **h:h** and **h** adsorption, the intensity decreases above the LUMO+1, but does not reach zero, the dI/dV of the **a** adsorbed molecules reaches zero above the LUMO+1. Since the **a** adsorption is close to the one observed for C_{60} on cobalt (Fig. 5.4b), we may conclude that adsorption **a** favors a decrease of the dI/dV after the LUMO+1. A small change in the charge transfer for copper compared to cobalt however must affect the amplitude and/or peak positions of the LUMO+1 and LUMO+2, which turns out to be favorable for an NDR in the case of cobalt.

Comparing the intersection of the LUMO+1 with a spheric Cu 4s tip orbital for different orientations allows for an understanding of the changes in the intensity of the LUMO+1 resonance (see Fig. 5.13). While **a** and **h:p** (similar to **a**, not shown here) orientations have a strong overlap with the copper 4s orbital, **p** and **h:h** present intermediate cases, and **h** shows a

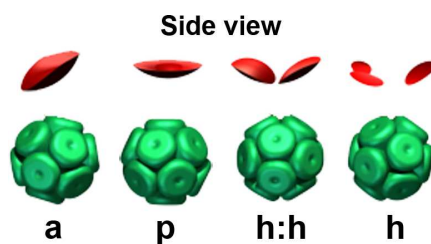


Figure 5.13: Intersection of the LUMO+1 with a spherically symmetric Cu 4s tip orbital at a distance of 5.4 Å (side view). **a** orientation yields the strongest overlap, while **h** orientation shows the smallest overlap. Figure adapted from Ref. [189].

weak overlap. The stronger the overlap, the higher is the expected intensity of the resonance. Based on the results obtained for C₆₀ on Cu(111), the **a** and **h:p** orientations should produce the highest NDR for a given tip structure. A detailed simulation is currently carried out by W. A. Hofer.

As we have seen that the NDR for the case of cobalt depends on the tip position above the molecule (*cf.* Fig. 5.5 and Fig. 5.6), we also studied the position dependence of the dI/dV for **h** adsorbed molecules on copper. Figure 5.14a shows dI/dV spectra acquired above three characteristic spots of the molecule, namely the central hexagon, a hexagon-hexagon (*h:h*) bond and a pentagon. No NDR is observed. This was tested for a variety of sharp tips showing an NDR on cobalt.¹⁰ Maps of the differential conductance at a constant height (Fig. 5.14b) confirm the absence of an NDR.

In this section we could show how the amplitude of a molecular resonance determines the NDR phenomenon. However, the structured DOS of the tip necessary for NDR is not accessible experimentally in standard STM configuration, no tip induced features being observed in the dI/dV above Cu(111) for all tips employed [see Fig. 2.3 (page 17)]. To extend our study to a case where we have experimentally access to both tip and sample electronic states, we use in the following an "inverted STM" experiment.

¹⁰In general, these spectra compare well with dI/dV spectra of C₆₀ on Cu(111) reported in literature [241, 243]. However, for the same system a downward shift in energy of the LUMO is reported for samples being annealed to 415 K [247], or 570 K [243], respectively. Annealing above room temperature was shown earlier to introduce a reconstruction of the copper surface beneath the C₆₀ layer [242], and this reconstruction changes the bonding and the charge transfer between the molecule and the surface, leading to a half-filled LUMO at E_F [243]. In our experiment, C₆₀ was always deposited at room temperature to avoid intermixing between cobalt and copper.

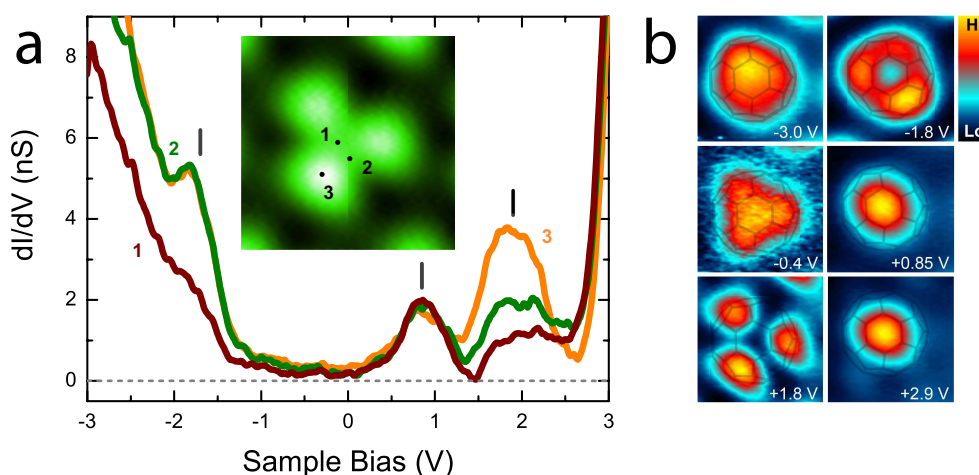


Figure 5.14: Differential conductance of **h** adsorbed C_{60} on Cu(111). a) dI/dV spectra labeled 1, 2 and 3 are acquired with the tip positioned over the spots indicated in the inset (constant-height current map, bias: 2.1 V, size: $12 \times 12 \text{ \AA}^2$). Vertical lines indicate the HOMO, LUMO and LUMO+1. Feedback opened at 1.0 V and 2.0 nA. b) Constant-height dI/dV maps of **h** adsorbed C_{60} (sample bias as indicated in each map; map size: $10 \times 10 \text{ \AA}^2$). As guide for the eye a C_{60} model is superimposed on each map. The LUMO+1 (+1.8 V) is visualized in the typical trefoil shape, indicating the position of the three pentagonal rings. The inequality of the three maxima suggests a slight tilt of the **h** adsorbed molecule, which is confirmed by means of DFT geometry optimization.

5.6 C_{60} on the tip apex - tuning the NDR

The inversion of the experimental setup can be achieved by recording dI/dV above the clean metal surface with a C_{60} adsorbed on the tip apex [236, 248, 249]. This allows for probing a C_{60} adsorbed on a metal surface with a well-characterized counter electrode, the copper surface then acting as "STM tip". Schull *et al.* have shown that it is possible to "pick up" a single C_{60} molecule with the STM tip out of a C_{60} monolayer in a controlled manner [236]. In our case, such an experiment leads to a single C_{60} attached to the copper-covered tip, representing then one of the electrodes of the tunnel junction (in the following called " C_{60} -tip"). One way to attach a molecule to the tip is to position the tip above the target C_{60} on cobalt, e.g. the central C_{60} in Fig. 5.15b, and open the feedback at -0.1 V and 0.2 nA. The sample bias is held at -0.1 V and the tip is approached towards the molecule, simultaneously recording the current $[I(z)]$ [250]. Figure 5.15a shows the conductance G as a function of the tip displacement with

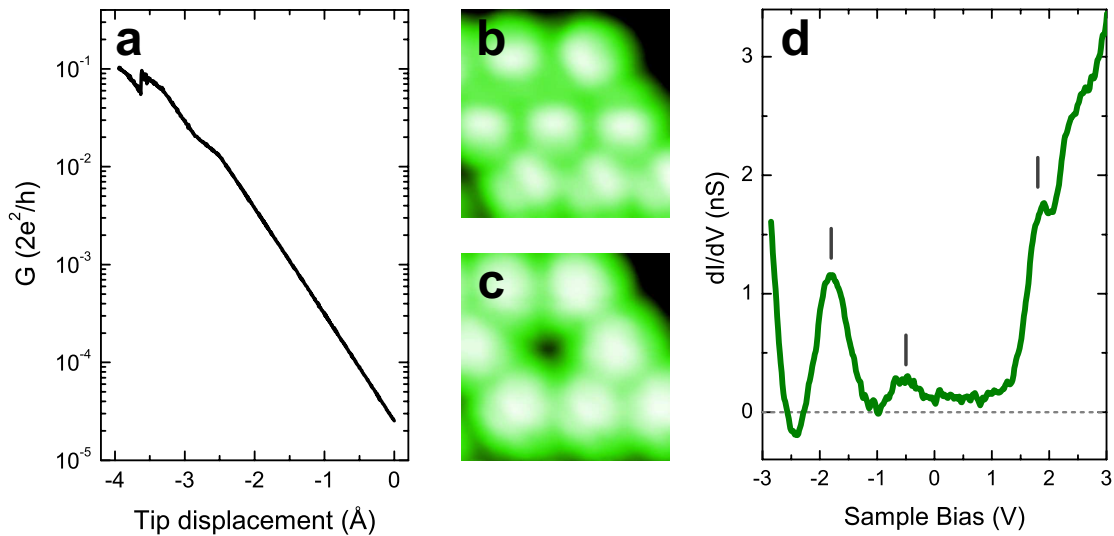


Figure 5.15: C_{60} -terminated tip. a) Conductance of the tunnel junction as a function of the tip displacement (sample bias: -100 mV, feedback opened at 0.2 nA, -100 mV). A copper-terminated tip is approached towards a C_{60} on cobalt. A discontinuity of the conductance is observed at roughly $0.1 G_0$, which is associated with a sudden change in the junction geometry, e.g. the "jump" of the C_{60} from the surface onto the tip. b and c) topographs showing a C_{60} monolayer on a cobalt island before (b) and after (c) the controlled "pick-up" of C_{60} (size: 3.0×3.0 nm², gap conditions: 1.9 V, 0.2 nA). The hole of the extracted C_{60} is clearly visible in (c). d) dI/dV spectrum acquired over the clean Cu(111) surface with a C_{60} molecule adsorbed on the tip apex (" C_{60} -tip"). Feedback opened at 3.1 V and 4.0 nA. The fitted energetic positions of HOMO ($+1.8$ V), LUMO (-0.5 V) and LUMO+1 (-1.8 V) are marked with vertical bars (mind the bias inversion due to the molecule being adsorbed on the tip). A pronounced NDR is detected below the LUMO+1.

G given in fractions of the conductance quantum G_0 :

$$G_0 = \frac{2e^2}{h} = 77.48 \mu S,$$

where e is the charge of an electron and h the Planck constant. G_0 is the conductance of one conductance channel, if the transmission probability for an electron equals one. It corresponds to a resistance of 12.9 k Ω . With decreasing tip-sample distance, the conductance increases exponentially as expected for the tunneling regime (see Fig. 5.15a). After a slight change in the slope for $G > 0.01G_0$, a sudden drop in the conductance occurs at roughly $0.1 G_0$ (750 nA), which can be associated with an abrupt change in the junction geometry. We did not further

decrease the tip-sample distance, but retracted the tip to the starting distance. Figure 5.15c shows the same zone as in Figure 5.15b, but after the $I(z)$, the central molecule missing in the monolayer. Therefore the sudden change in the conductance is associated with a "jump" of the molecule from the cobalt surface to the copper tip.¹¹ The "jump" occurs at $0.1 G_0$, *i.e.* before the formation of a tip-sample contact, which is reported for C_{60} /metal systems to occur at $0.3 G_0$ [196, 198, 236]. We also attached C_{60} to the tip following Ref. [236]. There the tip is brought into contact with the molecule (feedback opened at $1 \mu\text{A}$ and -0.2V) and pressed against the C_{60} by subsequent $I(Z)$ s. This procedure alters the tip structure and leads to a flat tip apex on which the C_{60} is adsorbed [236]. A decomposition of the molecular cage as reported by Schulze *et al.* can be ruled out, as the electric power employed here is 0.1 to $0.2 \mu\text{W}$, which is more than a hundred times smaller than the power needed for decomposition of C_{60} on $\text{Cu}(110)$ [198].

If a dI/dV spectrum is acquired with a C_{60} -tip, the dI/dV reflects the convolution of the electronic structure of the molecule adsorbed on the tip with the surface electronic states. To anticipate the experimental spectra, we can again start with Equation 5.2:

$$I_t \propto \int_0^{eV} \rho_t(E - eV) \rho_{C_{60}}(E) dE, \quad (5.3)$$

where C_{60} is on the surface and the transmission factor T is constant. For a constant tip DOS, the differential conductance is then proportional to the C_{60} DOS:

$$\frac{dI}{dV} \propto \rho_{C_{60}}(eV). \quad (5.4)$$

If now the molecule is attached to the tip, Eq. 5.2 is written as:

$$I_t \propto \int_0^{eV} \rho_{C_{60}}(E - eV) \rho_s(E) dE. \quad (5.5)$$

By introducing $E - eV = E'$ we can write:

$$I_t \propto \int_{-eV}^0 \rho_{C_{60}}(E') \rho_s(E' + eV) dE'. \quad (5.6)$$

¹¹A reproducible molecule attachment to the tip was achieved only using sharp tips, which provide a focused electric field.

In a rough approximation we take the sample DOS as constant and differentiate:

$$\frac{dI}{dV} \propto \frac{d}{dV} \int_{-eV}^0 \rho_{C_{60}}(E') dE', \quad (5.7)$$

and this leads to:

$$\frac{dI}{dV} \propto \rho_{C_{60}}(-eV). \quad (5.8)$$

Based on Eqs. 5.4 and 5.8, the dI/dV is proportional to the molecular DOS, but for the case of the C₆₀-tip the bias dependence is inverted. Unoccupied MOs will appear at negative bias, while occupied MOs appear at positive bias. The same result would be obtained by changing the polarity of the bias in the STM junction.

The experimental dI/dV of the Cu(111) surface acquired with a C₆₀-tip is shown in Fig. 5.15d. As predicted above, the spectrum shows the peaks of the molecular resonances but at opposite biases compared to C₆₀ adsorbed on the surface (*cf.* Fig. 5.5 or Fig. 5.14a). The HOMO is detected in positive bias regime as a shoulder at +1.8 V, while LUMO and LUMO+1 appear at negative biases at -0.5 V and -1.8 V, respectively. Remarkably, below the intense LUMO+1 peak, an NDR occurs at -2.4 V.

5.6.1 Orientation of C₆₀ at the tip apex

To further characterize the tip, we determine the orientation of C₆₀ at the tip apex by scanning above an individual adatom on the surface [236], which leads to an inverted topographic image of the molecule at the tip apex as seen by an individual adatom (see Fig. 5.16e–h). Thereby we can relate the dI/dV above Cu(111) to the orientation of the molecule as presented in Fig. 5.16. We therefore evaporated Au atoms in small amounts onto the cold sample. After preparing a C₆₀-tip, the molecular orientation can be modified by bringing the tip into contact with the adatom [238]. Figures 5.16a–d show dI/dV spectra of Cu(111) for four different orientations of C₆₀ as shown by the corresponding inverted images (Fig. 5.16e–h). We note that the **a** configuration leads to the most intense LUMO+1 peak. At the same time, only the dI/dV of the **a** oriented tip shows a pronounced NDR below the LUMO+1, while the dI/dV of the **p** tip shows a weak NDR and **h:h** and **h** oriented molecular tips possess dI/dV s with zero conductance regions. Hence the change of the molecular orientation by controlled tip–adatom contacts allows for a tuning of the NDR behavior of the tunnel junction.

This confirms the findings of section 5.5, as we observe the same trend as before, and

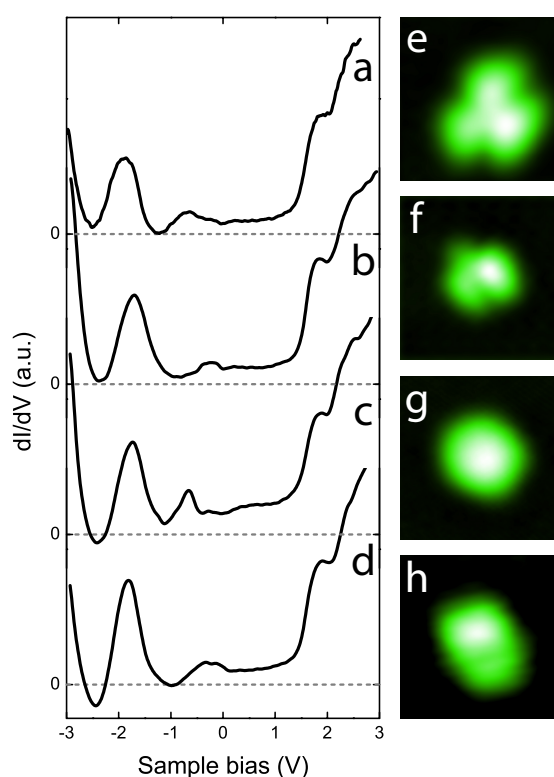


Figure 5.16: Orientation of C_{60} at the tip apex. a–d) dI/dV above Cu(111) acquired with a C_{60} adsorbed in different orientations at the tip. Feedback opened: 1 V, 0.1 nA. e–h) corresponding inverted STM topographs (-2.0 V, 0.1 nA, $19 \times 19 \text{ \AA}^2$). The orientation of the molecule at the tip apex is imaged by an atom adsorbed on the substrate: **h** (a,e), tilted **h:h** (b,f), **p** (c,g), **a** (d,h).

underlines the importance of the orientation for the observation of an NDR. Charge transfer and binding seem to play a minor role, as the metal–molecule interface for a C_{60} adsorbed on the tip differs considerably from the interface between C_{60} and the flat Cu(111) surface.

A final experimental finding for the spectroscopy by means of a C_{60} -tip is presented in Fig. 5.17: the NDR is highly sensitive to the surface electronic structure, the same tip only showing an NDR for spectra acquired above Cu(111), while the spectra above an individual adatom, cobalt islands or another C_{60} molecule do not yield an NDR. This might explain why only one out of three copper covered tips showed an NDR for C_{60} on cobalt, since the microscopic structure of the STM tip, which is unknown, influences its DOS.

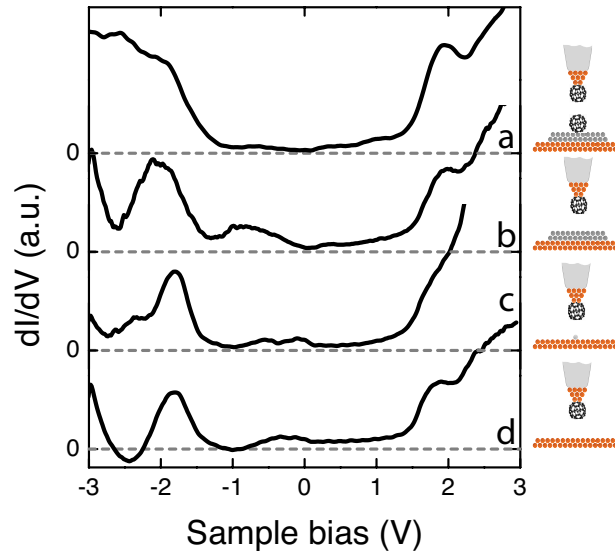


Figure 5.17: dI/dV spectra above different surfaces by means of an **a** oriented C_{60} -tip: C_{60} on cobalt island [a], Co island [b], Au adatom on Cu(111) [c], Cu(111) [d]. Feedback opened at 1 V and 0.1 nA. The schemes on the right show the corresponding experimental setup.

5.6.2 NDR produced by a Shockley surface state

As shown above, the electronic structure of Cu(111) allows for the detection of an NDR with the C_{60} -tip. Therefore we extend the simulations of section 5.4.3 to a more realistic case that employs a realistic electronic structure of the tip and the sample. The C_{60} DOS is represented by a series of Gaussian peaks fitted to an experimental spectrum of C_{60} , which does not show an NDR (see Fig. 5.18a), while the surface DOS was modeled with a constant background density of states and a step function at -0.45 V of comparable amplitude, which represents the Shockley surface state (Fig. 5.18a).¹² The resulting dI/dV spectrum shows a pronounced NDR below the LUMO+1 as was observed in the experiment (Fig. 5.18c). Therefore we can unambiguously identify the origin of the NDR to be the Shockley surface state. The projected bulk band gap of Cu(111) is responsible for the weak background DOS and favors the NDR. If an increased background density of states for low energies is included (Fig. 5.18b) to account for tunneling into bulk states below -1 V [*cf.* Fig. 2.3 (page 17)], this reduces the NDR (Fig. 5.18d). It is worth mentioning that only an occupied surface states can yield an NDR.

¹²The use of a step function for the surface state is justified, as the linewidth of the surface state is small compared to the peak width of the MOs.

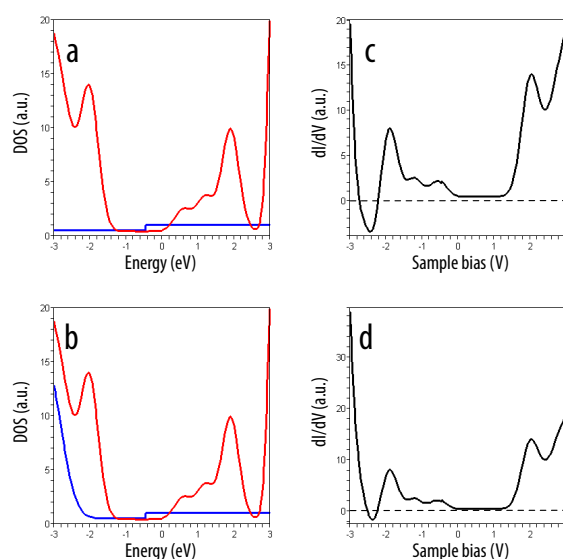


Figure 5.18: Simulated dI/dV of Cu(111) with a C_{60} -tip. blue: Cu(111) DOS; red: C_{60} DOS; black: simulated dI/dV . a) fitted C_{60} DOS and model Cu(111) DOS. c) simulated dI/dV spectrum with NDR corresponding to (a). b) Cu(111) DOS including surface state and bulk states. d) dI/dV spectrum corresponding to (b) shows a reduced NDR. The surface DOS was modeled with a constant background density of states of 0.5 and a step function of an amplitude of 0.5 at -0.45 V for (a); for (c) an additional Gaussian peak at -3.2 V of amplitude 14 and width 0.8 eV was added to account for bulk states below -1 eV. The C_{60} DOS was composed out of a background of 0.4 and six Gaussian peaks G1 to G6 (G1: $V_1 = -3.2$ eV, $w_1 = 1.1$ eV, $A_1 = 27$; G2: -2 eV, 0.48 eV, 7; G3: 0.58 eV, 0.48 eV, 1.2; G4: 1.2 eV, 0.48 eV, 1.9; G5: 1.9 eV, 0.48 eV, 5.7; G6: 3.1 eV, 0.29 eV, 9.0).

Unoccupied surface states like on Pt(111) do not provide a decrease in the DOS with increasing bias and will not, even in the presence of a pronounced occupied peak in the counter electrode DOS, cause an NDR.

Summary and conclusions

In this chapter, we investigated monolayers of C_{60} adsorbed on cobalt islands and on Cu(111), focusing on the occurrence of an NDR in the bias-dependent conductance. To the best of our knowledge, these results constitute the first experimental observation of an NDR for C_{60} on a metal surface. We showed that the NDR results from a bias-dependent mismatch of the MOs of C_{60} with electronic states of the tip, to say from a local orbital matching. By

means of a simple, WKB-based simulation we could pinpoint the determining factors for the NDR:

- the coeval existence of an occupied peak close to E_F at one electrode and an unoccupied peak at the other electrode
- the product of the tip and sample peak amplitude being superior to the product of the tip and sample background
- several peaks at one electrode being well separated

We showed in the following that, for the case of C_{60} , the LDOS amplitude of the LUMO+1 is the decisive factor for the NDR to occur. Therefore the NDR could be tuned through the orientation of C_{60} on the surface or the tip, since the molecular orientation alters the peak amplitude. Furthermore we showed that, for the C_{60} -tip in the inverted STM experiment, NDR is produced by the Shockley surface states on Cu(111).

We expect an NDR to occur in similar systems, which provide huge peak-to-valley ratios with sharp peaks in the DOS, since then small structures in the tip DOS can be sufficient to produce an LOM-based NDR. C_{60} seems to be a suitable candidate due to its 3D structure, which decreases the background DOS and provides high-intensity peaks. For instance, combining a C_{60} -tip with surfaces that provide occupied structures in the vicinity of E_F could yield an NDR. Potential candidates are: Au(111), or Ag(111), due to the occupied surface states of these (111) surfaces; Pb multilayers grown on Si(111), since they provide, depending on the number of layers, occupied quantum-well states close to E_F [251]; single adatoms, which possess an occupied d resonance close to E_F .

Conclusion and perspectives

Nanoscaled objects like metal islands, single atoms and molecules are key ingredients for molecular electronics and spintronics. In this thesis, cobalt nanoislands, transition-metal adatoms and individual molecules were explored by means of scanning tunneling microscopy and spectroscopy. Using STM techniques, electronic and spin-polarized properties of nanoscaled systems could be linked to structural properties, such as the adsorption site in the case of molecules, or the stacking and size in the case of metallic islands. Comparing results obtained for adatoms and molecules on the two (111) surfaces copper and cobalt islands allowed for an analysis of the influence of the substrate.

After a brief introduction of the STM techniques used and some details regarding the sample preparation, the second chapter introduced the electronic and structural properties of the (111) surfaces employed, namely Cu(111) and cobalt nanoislands grown on Cu(111). Ferromagnetic cobalt islands on Cu(111) with sizes between 5 and 30 nm were investigated, these islands being of particular interest as they can act as magnetic hosts for adatoms or molecules. By means of STS and DFT calculations, we established a direct relation between the decrease of the island size and the interatomic distances and the shift of the *d*-like resonances of the island LDOS to lower energies. These results present a first experimental validation for the concept of "mesoscopic relaxation" [34, 35]. They also indicate that surface states can be a sensitive probe for the structure at an atomic scale.

In the third chapter, we presented a study on individual adatoms on cobalt islands comparing the results to the adsorption on Cu(111). This study is embedded in the context of spintronics. Similar to adatoms on copper, which localize the Shockley surface states leading to a bound state, the adatoms on the magnetic cobalt islands present a common signature in STS. KKR calculations unveiled the complex nature of this signature, which is composed of surface-induced states of majority and minority spin character as well as of atomic *d* resonances. These different contributions locally alter the spin-polarization. While the pristine island is governed by minority

d states and provides strong negative polarization, the adatom LDOS shows positive polarization in vacuum aside the energies where atomic resonances fall. This is due to the localization of the dispersive majority surface state at the atoms site, *i.e.* a majority bound state, which dominates over a wide range of energy. A single atom can therefore act as a element-specific, bias-dependent spin filter, this opening up perspectives for future spintronic devices.

Our results underline the major influence of the tip structure on the SP contrast when doing SP-STM experiments. Turning the STM setup – in a gedankenexperiment – upside-down and taking the adatom on cobalt as a model of an atomic SP-STM tip, its polarization is governed by majority states near E_F , the clean cobalt island, a model for a blunt tip, being however dominated by minority resonances. Future studies could aim on expanding this study to various adatoms and magnetic surfaces, or to more complex structures like dimers, trimers or small pyramids constructed by atom manipulation, to gain experimental insight into the role played by the STM tip in spin-polarized measurements. The here presented study should also improve our comprehension of planar magnetic tunnel junctions, where surface roughness or impurities are known to reduce or even inverse the polarization compared to an ideal surface.

In chapter 4 we extended the study of individual atoms to cobalt atoms surrounded by an organic ligand, *i.e.* we studied single Cobalt-Phthalocyanine molecules adsorbed on Cu(111) and on cobalt islands. By means of a co-deposition of CoPc and Co atoms on Cu(111) and "manipulated atom imaging", we could resolve the adsorption site of the molecule with atomic resolution. Furthermore, the bias-dependent conductance channels of CoPc were unveiled by means of constant-height dI/dV mapping, this technic not being employed for the study of single molecules before, and identified by combining the experimental results with DFT calculations. In the second part of the chapter, we could demonstrate for the first time, how SP-STS can be used to visualize the spin-polarization of individual molecules, here shown for CoPc adsorbed on ferromagnetic cobalt islands. DFT calculations revealed the nature of the spin-polarized molecular states probed in the experiment and described the origin of the ferromagnetic coupling between the molecule and the substrate. An individual molecule showed a spin-filter-like character, which is strongly influenced by the organic ligand, even though the SP signal was centered on the core of the molecule. First, the ferromagnetic interaction, which is predicted between CoPc and the surface, is partly carried by the organic ligands, and second, the ligands govern the adsorption geometry of CoPc.

Even though the adsorption of CoPc on the two (111) surfaces is similar, differences in the electronic conductance appear due to the more complex electronic structure of the cobalt

substrate compared to copper. On copper, the molecule becomes nonmagnetic due to a charge transfer upon adsorption. On cobalt in contrast, CoPc partially preserves an unpaired spin, even though the magnetic moment is slightly reduced. This allows for the detection of an SP contrast on the molecule. With respect to the spin-polarized STS study of CoPc on cobalt islands presented in chapter 4, further studies will aim at detecting SP signals not only on cobalt but also on the organic ligands. This will be possible by means of the improved intramolecular resolution of the constant-height dI/dV maps compared to the constant-current dI/dV maps, as shown for CoPc on Cu(111) in chapter 1. An alternative path consists in an exchange of CoPc with H₂Pc to eliminate the dominant cobalt d state and detect surface induced states over the molecule, which should be spin-polarized for molecules on the ferromagnetic cobalt islands.

Another way to extend the presented studies of CoPc consists in exploring new organometallic molecules. In this context, we deposited monolayer islands of Ferrocene (FeCp₂) onto Cu(111) [see Fig. 5.19a]. This molecule is a so-called sandwich complex made out of two cyclopentadienyl (Cp) radicals bound on opposite sides to an iron atom. Upon adsorption a direct contact between the central iron atom and the substrate is inhibited due to the underlying Cp ring, which seems to strongly reduce the molecule–substrate interaction compared to CoPc, since an interface state [61,252], originating from the Shockley surface state of Cu(111), appears, this being a sign of weak or zero charge transfer. An element-dependent adsorption of single atoms on this layer is also evidenced (see Fig. 5.19b–e). Further experiments and Molecular Dynamics simulations provided by Mauro Boero¹³ are in progress, since this system presents a model playground for studying the relation between chemistry, structure and electronic states at the nanoscale by means of STM/STS. A deposition onto magnetic surfaces focusing on the magnetic interaction between cobalt and the FeCp₂ or the adatom complexes will complete this study.

Finally, in the last chapter, we exchanged the organometallic molecules with the pure-carbon molecule C₆₀. The deposition of C₆₀ onto the Co/Cu(111) system leads to ordered monolayers of different orientation for Cu(111) and cobalt. Depending on the orientation, current-voltage characteristics acquired above C₆₀ possess a particularity, namely a negative differential resistance (NDR), which is a device characteristic widely used in electronics. This study constitutes the first experimental observation of an NDR for C₆₀ directly adsorbed on a

¹³Institut de Physique et Chimie des Matériaux de Strasbourg

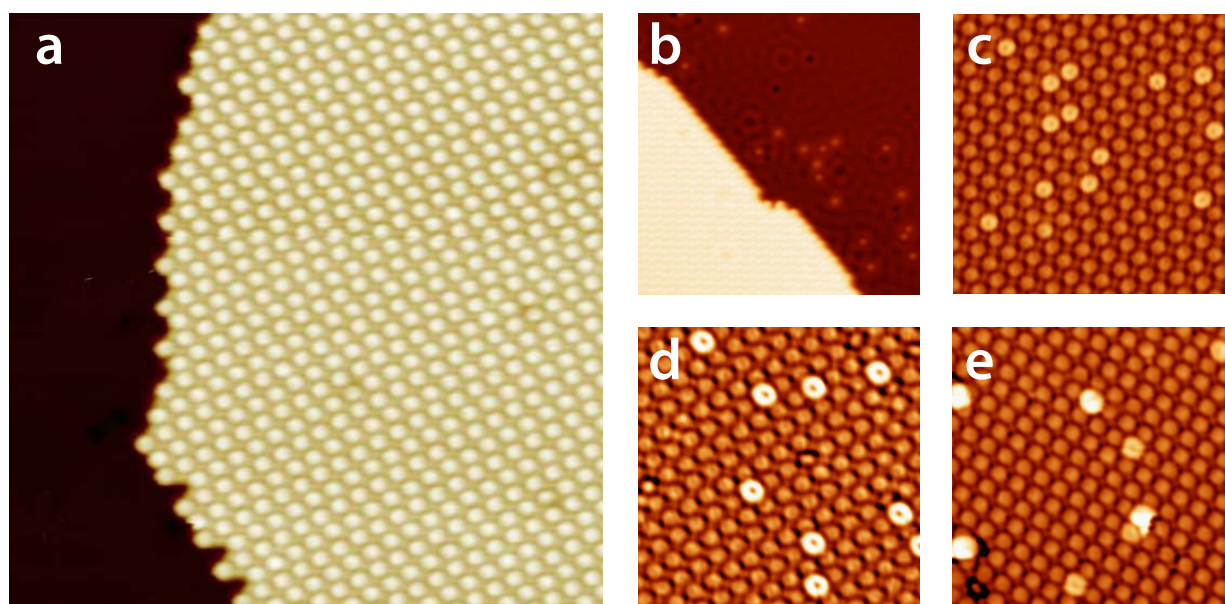


Figure 5.19: Ferrocene layer with and without adatoms. a) Topograph of FeCp_2 monolayer on $\text{Cu}(111)$. d–e) Selective atom capturing on a FeCp_2 monolayer. Topographs of a FeCp_2 monolayer after deposition of Fe (b), Cu (c), Co (d), or Au atoms (e), respectively. Gap conditions: 5 pA and -50 mV; image size: 25×25 (a), 33×33 (b), 12×12 (c), 11×12 (d), and 12×12 nm² (e), respectively. Iron atoms do not stick to the molecular layer (b), while Cu adsorbs without a sign of destruction (c). Co forms higher, donut-like complexes on the molecular layer, depressions occur in the layer (d). Au deposition leads to atoms and complexes, depressions are also observed (e).

metal substrate. It originates from a bias-dependent match and mismatch of molecular orbitals with electronic states of the tip apex atoms (local orbital matching), as could be unveiled by combining the experimental results with numerical simulations. Attaching a C_{60} to the tip opens up the possibility to engineer the NDR: In dI/dV spectroscopy above $\text{Cu}(111)$, the " C_{60} -tip" exhibits the same spectrum as C_{60} adsorbed on the substrate, but at opposite biases due to the inverted junction geometry. The observed NDR is assigned to an orbital matching mechanism of the LUMO+1 with the Shockley surface states of $\text{Cu}(111)$ and is tuned through the orientation of C_{60} relative to the tip. Based on these findings we expect an NDR for systems that provide important peak-to-valley ratios with sharp peaks in the DOS, since then small structures in the tip DOS are sufficient for a local-orbital-matching mechanism. Similar to copper, $\text{Au}(111)$ and $\text{Ag}(111)$ could produce an NDR when combined with a C_{60} -tip, since they also provide occupied surface states. But also Pb multilayers grown on $\text{Si}(111)$, which posses quantum-well states

close to E_F [251], or single adatoms with occupied d resonance close to E_F are candidates for an NDR when probed with a C_{60} -tip.

Fifty years after Feynman's speech at the annual meeting of the American Physical Society in 1959 [1], many of his ideas have become reality; we can carry a whole library in our pocket, our computers fit into a briefcase and surgeons operate by means of tiniest robots from inside of the body, *Google* provides image recognition on the cell phone and atoms can be manipulated through the Internet.¹⁴ On the other hand, some of the raised questions still remain open: we haven't gone far in a physicist's approach of chemical engineering, to say an atom-by-atom construction of complicated molecules. Even though STM enables atom manipulations on the surface, including the construction of more or less complicated atomic structures [53], only few examples of tip-induced chemical reactions are reported [253–256]. And these tip-assisted reactions, e.g. current-induced polymerizations [254], a step-by-step synthesis of biphenyl out of iodobenzene [253], dehydrogenation [256], or hydrogen tautomerization reactions [255], resemble more a classical chemical reactions at a single-molecule level than the construction of a molecule *atom-by-atom* as foreseen by Feynman.

Regardless the enormous progress made in recent years, a second not yet achieved goal is an electronic based on devices made out of a couple of atoms, something we call *molecular electronics* nowadays. It is still under discussion, if either spin crossover compounds, single-molecular magnets or single-chain magnets are the most appropriate candidates to achieve this goal (see Ref. [257] for an overview) and open questions are to answer until carbon-based electronics will take over. One of the most urgent ones is the limited control of the organic–inorganic contact. As this contact is essential for the functionality of the molecule, its stability, the controlling and the integration into circuits, scientists long for a better understanding of the processes involved when creating the contact and the resulting properties. With this in mind, this thesis presented an STM-based approach for the investigation of the molecule–metal contact, trying to gain some insight into the interplay of structure, chemistry and electronics at an atomic, to say molecular scale.

¹⁴As demonstrated by Don Eigler during a lecture at Cornell University in 2005

Bibliography

- [1] R. Feynman gave this speech at the annual meeting of the American Physical Society on 29th of December in 1959. Online: <http://www.zyvex.com/nanotech/feynman.html>.
- [2] J. A. A. J. Perenboom, P. Wyder, and F. Meier. Electronic properties of small metallic particles. *Physics Reports*, 78(2):173 – 292, 1981.
- [3] R. Kern and P. Müller. Elastic relaxation of coherent epitaxial deposits. *Surface Science*, 392(1-3):103 – 133, 1997.
- [4] A. L. Vázquez de Parga, F. J. García-Vidal, and R. Miranda. Detecting electronic states at stacking faults in magnetic thin films by tunneling spectroscopy. *Physical Review Letters*, 85(20):4365–4368, Nov 2000.
- [5] L. Diekhöner, M. A. Schneider, A. N. Baranov, V. S. Stepanyuk, P. Bruno, and K. Kern. Surface states of cobalt nanoislands on Cu(111). *Physical Review Letters*, 90(23):236801, Jun 2003.
- [6] O. Pietzsch, A. Kubetzka, M. Bode, and R. Wiesendanger. Spin-polarized scanning tunneling spectroscopy of nanoscale cobalt islands on Cu(111). *Physical Review Letters*, 92(5):057202, Feb 2004.
- [7] O. Pietzsch, S. Okatov, A. Kubetzka, M. Bode, S. Heinze, A. Lichtenstein, and R. Wiesendanger. Spin-resolved electronic structure of nanoscale cobalt islands on Cu(111). *Physical Review Letters*, 96(23):237203, 2006.
- [8] Y. Yayon, V. W. Brar, L. Senapati, S. C. Erwin, and M. F. Crommie. Observing spin polarization of individual magnetic adatoms. *Physical Review Letters*, 99(6):067202, 2007.
- [9] M. V. Rastei, B. Heinrich, L. Limot, P. A. Ignatiev, V. S. Stepanyuk, P. Bruno, and J. P. Bucher. Size-dependent surface states of strained cobalt nanoislands on Cu(111). *Physical Review Letters*, 99(24):246102, 2007.
- [10] Evgeny Y. Tsybal, Oleg N. Mryasov, and Patrick R. LeClair. Spin-dependent tunnelling in magnetic tunnel junctions. *Journal of Physics: Condensed Matter*, 15(4):R109, 2003.
- [11] B. W. Heinrich, C. Iacovita, M. V. Rastei, L. Limot, J. P. Bucher, P. A. Ignatiev, V. S. Stepanyuk, and P. Bruno. Spin structure of an atomic protrusion: Probing single atoms on cobalt

- nanoislands. *Physical Review B*, 79(11):113401–113404, March 2009.
- [12] Joseph A. Stroscio and Robert J. Celotta. Controlling the dynamics of a single atom in lateral atom manipulation. *Science*, 306(5694):242, 2004.
- [13] M. Grobis, A. Wachowiak, R. Yamachika, and M. F. Crommie. Tuning negative differential resistance in a molecular film. *Applied Physics Letters*, 86(20):204102, 2005.
- [14] Lan Chen, Zhenpeng Hu, Aidi Zhao, Bing Wang, Yi Luo, Jinlong Yang, and J. G. Hou. Mechanism for negative differential resistance in molecular electronic devices: Local orbital symmetry matching. *Physical Review Letters*, 99(14):146803, Oct 2007.
- [15] K. J. Franke, G. Schulze, N. Henningsen, I. Fernández-Torrente, J. I. Pascual, S. Zarwell, K. Rück-Braun, M. Cobian, and N. Lorente. Reducing the molecule-substrate coupling in C₆₀-based nanostructures by molecular interactions. *Physical Review Letters*, 100(3):036807, Jan 2008.
- [16] X. W. Tu, G. Mikaelian, and W. Ho. Controlling single-molecule negative differential resistance in a double-barrier tunnel junction. *Physical Review Letters*, 100(12):126807, Mar 2008.
- [17] X. Q. Shi, Woei Wu Pai, X. D. Xiao, J. I. Cerdá, R. Q. Zhang, C. Minot, and M. A. Van Hove. Significant negative differential resistance predicted in scanning tunneling spectroscopy for a C₆₀ monolayer on a metal surface. *Physical Review B*, 80(7):075403, Aug 2009.
- [18] R. Lloyd Carroll and Christopher B. Gorman. The genesis of molecular electronics. *Angewandte Chemie International Edition*, 41(23):4378–4400, 2002.
- [19] C. Iacovita. *Spin-dependent tunneling into single cobalt-phthalocyanine molecules*. PhD thesis, Université de Strasbourg, 2009.
- [20] Joel A. Appelbaum and W. F. Brinkman. Theory of many-body effects in tunneling. *Physical Review*, 186(2):464–470, Oct 1969.
- [21] Vladimir A. Ukraintsev. Data evaluation technique for electron-tunneling spectroscopy. *Physical Review B*, 53(16):11176–11185, Apr 1996.
- [22] H. Karacuban, M. Lange, J. Schaffert, O. Weingart, Th. Wagner, and R. Möller. Substrate-induced symmetry reduction of CuPc on Cu(111): An LT-STM study. *Surface Science*, 603:L39, 2009.
- [23] M. Böhringer, W.-D. Schneider, K. Glöckler, E. Umbach, and R. Berndt. Adsorption site determination of PTCDA on Ag(110) by manipulation of adatoms. *Surface Science*, 419:L95, 1998.
- [24] J. A. Stroscio and D. M. Eigler. Atomic and Molecular Manipulation with the Scanning Tunneling Microscope. *Science*, 254(5036):1319–1326, 1991.
- [25] J. Tersoff and D. R. Hamann. Theory of the scanning tunneling microscope. *Physical Review B*, 31(2):805–813, Jan 1985.

-
- [26] J. Kröger, L. Limot, H. Jensen, R. Berndt, S. Crampin, and E. Pehlke. Surface state electron dynamics of clean and adsorbate-covered metal surfaces studied with the scanning tunnelling microscope. *Progress in Surface Science*, 80(1-2):26 – 48, 2005.
- [27] M. Ziegler, N. Néel, A. Sperl, J. Kröger, and R. Berndt. Local density of states from constant-current tunneling spectra. *Physical Review B*, 80(12):125402, 2009.
- [28] J. A. Stroscio and R. M. Feenstra. *Scanning Tunneling Microscopy*, volume 27. Academic, New York, 1993.
- [29] Roland Wiesendanger. Spin mapping at the nanoscale and atomic scale. *Reviews of Modern Physics*, 81:1495, 2009.
- [30] D. Wortmann, S. Heinze, Ph. Kurz, G. Bihlmayer, and S. Blügel. Resolving complex atomic-scale spin structures by spin-polarized scanning tunneling microscopy. *Physical Review Letters*, 86(18):4132–4135, Apr 2001.
- [31] L. Limot, J. Kröger, R. Berndt, A. Garcia-Lekue, and W. A. Hofer. Atom transfer and single-atom contacts. *Physical Review Letters*, 94(12):126102, Apr 2005.
- [32] William Shockley. On the surface states associated with a periodic potential. *Physical Review*, 56(4):317–323, Aug 1939.
- [33] C. Iacovita, M. V. Rastei, B. W. Heinrich, T. Brumme, J. Kortus, L. Limot, and J. P. Bucher. Visualizing the spin of individual cobalt-phthalocyanine molecules. *Physical Review Letters*, 101(11):116602, 2008.
- [34] V. S. Stepanyuk, D. I. Bazhanov, A. N. Baranov, W. Hergert, P. H. Dederichs, and J. Kirschner. Strain relief and island shape evolution in heteroepitaxial metal growth. *Physical Review B*, 62(23):15398–15401, Dec 2000.
- [35] O. V. Lysenko, V. S. Stepanyuk, W. Hergert, and J. Kirschner. Mesoscopic relaxation in homoepitaxial metal growth. *Physical Review Letters*, 89(12):126102, Aug 2002.
- [36] M. C. Desjonquères and D. Spanjaard. *Concepts in Surface Physics*. Springer, 2 edition, 1995.
- [37] F. Duan and J. Guojun. *Introduction to Condensed Matter Physics*, volume 1. World Scientific, 2005.
- [38] P. M. Echenique and J. B. Pendry. The existence and detection of Rydberg states at surfaces. *Journal of Physics C: Solid State Physics*, 11:2065, 1978.
- [39] S. D. Kevan. Evidence for a new broadening mechanism in angle-resolved photoemission from Cu(111). *Physical Review Letters*, 50(7):526–529, Feb 1983.
- [40] N. V. Smith. Phase analysis of image states and surface states associated with nearly-free-electron band gaps. *Physical Review B*, 32(6):3549–3555, Sep 1985.
- [41] F. Reinert, G. Nicolay, S. Schmidt, D. Ehm, and S. Hüfner. Direct measurements of the I-gap surface states on the (111) face of noble metals by photoelectron spectroscopy. *Physical Review*

- B*, 63(11):115415, Mar 2001.
- [42] S. L. Hulbert, P. D. Johnson, N. G. Stoffel, W. A. Royer, and N. V. Smith. Crystal-induced and image-potential-induced empty surface states on Cu(111) and Cu(001). *Physical Review B*, 31(10):6815–6817, May 1985.
- [43] K. Giesen, F. Hage, F. J. Himpsel, H. J. Riess, and W. Steinmann. Two-photon photoemission via image-potential states. *Physical Review Letters*, 55(3):300–303, Jul 1985.
- [44] M. F. Crommie, C. P. Lutz, and D. M. Eigler. Imaging standing waves in a two-dimensional electron gas. *Nature*, 363:524–527, Jun 1993.
- [45] J. Kliewer, R. Berndt, E. V. Chulkov, V. M. Silkin, P. M. Echenique, and S. Crampin. Dimensionality Effects in the Lifetime of Surface States. *Science*, 288(5470):1399–1402, 2000.
- [46] W Steinmann. Spectroscopy of image-potential states by 2-photon photoemission. *Applied Physics A: Materials Science & Processing*, 49(4):365–377, OCT 1989.
- [47] L. C. Davis, M. P. Everson, R. C. Jaklevic, and Weidian Shen. Theory of the local density of surface states on a metal: Comparison with scanning tunneling spectroscopy of a Au(111) surface. *Physical Review B*, 43(5):3821–3830, Feb 1991.
- [48] Y. Hasegawa and Ph. Avouris. Direct observation of standing wave formation at surface steps using scanning tunneling spectroscopy. *Physical Review Letters*, 71(7):1071–1074, Aug 1993.
- [49] Jascha Repp, Francesca Moresco, Gerhard Meyer, Karl-Heinz Rieder, Per Hyldgaard, and Mats Persson. Substrate mediated long-range oscillatory interaction between adatoms: Cu /Cu(111). *Physical Review Letters*, 85(14):2981–2984, Oct 2000.
- [50] D. M. Newns. Self-consistent model of hydrogen chemisorption. *Physical Review*, 178(3):1123–1135, Feb 1969.
- [51] F. E. Olsson, M. Persson, A. G. Borisov, J.-P. Gauyacq, J. Lagoute, and S. Fölsch. Localization of the Cu(111) surface state by single Cu adatoms. *Physical Review Letters*, 93(20):206803, Nov 2004.
- [52] L. Limot, E. Pehlke, J. Kröger, and R. Berndt. Surface-state localization at adatoms. *Physical Review Letters*, 94(3):036805, Jan 2005.
- [53] M. F. Crommie, C. P. Lutz, and D. M. Eigler. Confinement of electrons to quantum corrals on a metal surface. *Science*, 262(5131):218–220, 1993.
- [54] E. J. Heller, M. F. Crommie, C. P. Lutz, and D. M. Eigler. Scattering and absorption of surface electron waves in quantum corrals. *Nature*, 369:464–466, Jun 1994.
- [55] M. F. Crommie, C. P. Lutz, D. M. Eigler, and E. J. Heller. Quantum corrals. *Physica D: Nonlinear Phenomena*, 83(1-3):98 – 108, 1995. Quantum Complexity in Mesoscopic Systems.
- [56] Saw-Wai Hla, Kai-Felix Braun, and Karl-Heinz Rieder. Single-atom manipulation mechanisms during a quantum corral construction. *Physical Review B*, 67(20):201402, May 2003.

-
- [57] Y. Pennec, W. Auwärter, A. Schiffrin, A. Weber-Bargioni, A. Riemann, and J. V. Barth. Supramolecular gratings for tuneable confinement of electrons on metal surfaces. *Nature Nanotechnology*, 2:99 – 103, 2007.
- [58] J.P. Gauyacq, A.G. Borisov, and M. Bauer. Excited states in the alkali/noble metal surface systems: A model system for the study of charge transfer dynamics at surfaces. *Progress in Surface Science*, 82(4-6):244 – 292, 2007. Dynamics of Electron Transfer Processes at Surfaces.
- [59] S. D. Kevan, editor. *Angle-Resolved Photoemission*. Elsevier, Amsterdam, 1992.
- [60] E. Bertel. Electronic surface states and the hydrogen dissociation barrier. *Physica Status Solidi A*, 1997!., 235, 1997.
- [61] Jascha Repp, Gerhard Meyer, and Karl-Heinz Rieder. Snell's law for surface electrons: Refraction of an electron gas imaged in real space. *Physical Review Letters*, 92(3):036803, Jan 2004.
- [62] D. B. Dougherty, P. Maksymovych, J. Lee, and J. T. Yates. Local spectroscopy of image-potential-derived states: From single molecules to monolayers of benzene on Cu(111). *Physical Review Letters*, 97(23):236806, Dec 2006.
- [63] Nicoleta Nicoara, Elisa Román, José M. Gómez-Rodríguez, José A. Martín-Gago, and Javier Méndez. Scanning tunneling and photoemission spectroscopies at the PTCDA/Au(111) interface. *Organic Electronics*, 7(5):287 – 294, 2006.
- [64] A. Scheybal, K. Müller, R. Bertschinger, M. Wahl, A. Bendounan, P. Aebi, and T. A. Jung. Modification of the Cu(110) Shockley surface state by an adsorbed pentacene monolayer. *Physical Review B*, 79(11):115406, Mar 2009.
- [65] J. de la Figuera, J. E. Prieto, C. Ocal, and R. Miranda. Scanning tunneling microscopy study of the growth of cobalt on Cu(111). *Physical Review B*, 47(19):13043–13046, May 1993.
- [66] J. de la Figuera, J. Prieto, G. Kostka, S. Müller, C. Ocal, R. Miranda, and K. Heinz. Crystallography and morphology of the early stages of the growth of Co/Cu(111) by LEED and STM. *Surface Science*, 349:L139–L145, mar 1996.
- [67] M. Ø. Pedersen, A. Bönicke, E. Lægsgaard, I. Stensgaard, A. Ruban, J. K. Nørskov, and F. Besenbacher. Growth of Co on Cu(111): subsurface growth of trilayer Co islands. *Surface Science*, 387:86–101, October 1997.
- [68] K. Heinz, S. Müller, and L. Hammer. Crystallography of ultrathin iron, cobalt and nickel films epitaxially grown on copper. *Journal of Physics: Condensed Matter*, 11:9437, 1999.
- [69] J. E. Prieto, J. de la Figuera, and R. Miranda. Surface energetics in a heteroepitaxial model system: Co/Cu(111). *Physical Review B*, 62(3):2126–2133, Jul 2000.
- [70] N. N. Negulyaev, V. S. Stepanyuk, P. Bruno, L. Diekhöner, P. Wahl, and K. Kern. Bilayer growth of nanoscale Co islands on Cu(111). *Physical Review B (Condensed Matter and Materials Physics)*, 77(12):125437, 2008.

- [71] U. Gradmann and J. Müller. *Zeitschrift für Angewandte Physik*, 30:87, 1970.
- [72] Michael Hohage, Michael Bott, Markus Morgenstern, Zhenyu Zhang, Thomas Michely, and George Comsa. Atomic processes in low temperature pt-dendrite growth on pt(111). *Physical Review Letters*, 76(13):2366–2369, Mar 1996.
- [73] I. Chado, C. Goyhenex, H. Bulou, and J. P. Bucher. Cluster critical size effect during growth on a heterogeneous surface. *Physical Review B*, 69(8):085413, Feb 2004.
- [74] A. Rabe, N. Memmel, A. Steltenpohl, and Th. Fauster. Room-temperature instability of Co/Cu(111). *Physical Review Letters*, 73(20):2728–2731, Nov 1994.
- [75] G. Bozzolo, A. L. Vázquez de Parga, D. Farías, and R. Miranda. Modeling of Co/Cu island formation on a Cu(111) surface. *Surface Review and Letters*, 11:591–597, 2004.
- [76] V. Rosato, M. Guillope, and B. Legrand. Thermodynamical and structural properties of f.c.c. transition metals using a simple tight-binding model. *Philosophical Magazine A*, 59:321 – 336, 1989.
- [77] K. Wildberger, V. S. Stepanyuk, P. Lang, R. Zeller, and P. H. Dederichs. Magnetic nanostructures: 4 *d* clusters on Ag(001). *Physical Review Letters*, 75(3):509–512, Jul 1995.
- [78] R. Zeller, P. H. Dederichs, B. Újfalussy, L. Szunyogh, and P. Weinberger. Theory and convergence properties of the screened Korringa-Kohn-Rostoker method. *Physical Review B*, 52(12):8807–8812, Sep 1995.
- [79] J. Zabloudil, R. Hammerling, L. Szunyogh, and P. Weinberger. *Electron Scattering in Solid Matter*, volume 147 of *Springer Series in Solid-State Sciences*. Springer-Verlag, Berlin, 2005.
- [80] H. Oka, P. A. Ignatiev, S. Wedekind, G. Rodary, L. Niebergall, V. S. Stepanyuk, D. Sander, and J. Kirschner. Spin-dependent quantum interference within a single magnetic nanostructure. *Science*, 327(5967):843–846, 2010.
- [81] L. Niebergall, V. S. Stepanyuk, J. Berakdar, and P. Bruno. Controlling the spin polarization of nanostructures on magnetic substrates. *Physical Review Letters*, 96(12):127204, Mar 2006.
- [82] B. W. Heinrich, C. Iacovita, M. V. Rastei, L. Limot, P. A. Ignatiev, V. S. Stepanyuk, and J. P. Bucher. A spin-selective approach for surface states at Co nanoislands. *Eur. Phys. J. B*, 75(1):49–56, may 2010.
- [83] R. Smoluchowski. Anisotropy of the electronic work function of metals. *Physical Review*, 60(9):661–674, Nov 1941.
- [84] O. Mironets, H. L. Meyerheim, C. Tusche, V. S. Stepanyuk, E. Soyka, P. Zschack, H. Hong, N. Jeutter, R. Felici, and J. Kirschner. Direct evidence for mesoscopic relaxations in cobalt nanoislands on Cu(001). *Physical Review Letters*, 100(9):096103, 2008.
- [85] M. V. Rastei, J. P. Bucher, P. A. Ignatiev, V. S. Stepanyuk, and P. Bruno. Surface electronic states in Co nanoclusters on Au(111): Scanning tunneling spectroscopy measurements and ab

- initio calculations. *Physical Review B (Condensed Matter and Materials Physics)*, 75(4):045436, 2007.
- [86] F. Meier, K. von Bergmann, P. Ferriani, J. Wiebe, M. Bode, K. Hashimoto, S. Heinze, and R. Wiesendanger. Spin-dependent electronic and magnetic properties of Co nanostructures on Pt(111) studied by spin-resolved scanning tunneling spectroscopy. *Physical Review B (Condensed Matter and Materials Physics)*, 74(19):195411, 2006.
- [87] S. N. Okuno, T. Kishi, and K. Tanaka. Spin-polarized tunneling spectroscopy of Co(0001) surface states. *Physical Review Letters*, 88(6):066803, Jan 2002.
- [88] J. Friedel. *The Physics of Metals: Electrons*, volume 1. Cambridge University Press, London, 1969. edited by J.M. Ziman.
- [89] V. Madhavan, W. Chen, T. Jamneala, M. F. Crommie, and Ned S. Wingreen. Local spectroscopy of a Kondo impurity: Co on Au(111). *Physical Review B*, 64(16):165412, Oct 2001.
- [90] E. Dupont-Ferrier, P. Mallet, L. Magaud, and J. Y. Veuillen. Bound states at impurities in a two-dimensional metal. *EPL (Europhysics Letters)*, 72(3):430–436, 2005.
- [91] F. E. Olsson, S. Paavilainen, M. Persson, J. Repp, and G. Meyer. Multiple charge states of Ag atoms on ultrathin NaCl films. *Physical Review Letters*, 98(17):176803, 2007.
- [92] N. Néel, J. Kröger, R. Berndt, and E. Pehlke. Spectroscopy of an atom between two electrodes. *Physical Review B (Condensed Matter and Materials Physics)*, 78(23):233402, 2008.
- [93] K. Schouteden, P. Lievens, and C. Van Haesendonck. Low-temperature STM/STS investigation of nanostructures created by an STM tip on Au(111) surfaces. *Applied Physics A: Materials Science & Processing*, 96(2):409–413, 2009.
- [94] Cyrus F. Hirjibehedin, Christopher P. Lutz, and Andreas J. Heinrich. Spin Coupling in Engineered Atomic Structures. *Science*, 312(5776):1021–1024, 2006.
- [95] K. von Bergmann, M. Bode, A. Kubetzka, M. Heide, S. Blügel, and R. Wiesendanger. Spin-polarized electron scattering at single oxygen adsorbates on a magnetic surface. *Physical Review Letters*, 92(4):046801, Jan 2004.
- [96] Focko Meier, Lihui Zhou, Jens Wiebe, and Roland Wiesendanger. Revealing magnetic interactions from single-atom magnetization curves. *Science*, 320(5872):82–86, 2008.
- [97] Lihui Zhou, Jens Wiebe, Samir Lounis, Elena Vedmedenko, Focko Meier, Stefan Blügel, Peter H. Dederichs, and Roland Wiesendanger. Strength and directionality of surface Ruderman-Kittel-Kasuya-Yosida interaction mapped on the atomic scale. *Nature Physics*, 6:187–191, 2010.
- [98] T. Jamneala, V. Madhavan, and M. F. Crommie. Kondo response of a single antiferromagnetic chromium trimer. *Physical Review Letters*, 87(25):256804, Nov 2001.
- [99] Jiutao Li, Wolf-Dieter Schneider, Richard Berndt, and Bernard Delley. Kondo scattering observed at a single magnetic impurity. *Physical Review Letters*, 80(13):2893–2896, Mar 1998.

- [100] V. Madhavan, W. Chen, T. Jamneala, M. F. Crommie, and N. S. Wingreen. Tunneling into a single magnetic atom: Spectroscopic evidence of the Kondo resonance. *Science*, 280(5363):567–569, 1998.
- [101] T. Jamneala, V. Madhavan, W. Chen, and M. F. Crommie. Scanning tunneling spectroscopy of transition-metal impurities at the surface of gold. *Physical Review B*, 61(15):9990–9993, Apr 2000.
- [102] Nikolaus Knorr, M. Alexander Schneider, Lars Diekhöner, Peter Wahl, and Klaus Kern. Kondo effect of single Co adatoms on Cu surfaces. *Physical Review Letters*, 88(9):096804, Feb 2002.
- [103] J. Merino and O. Gunnarsson. Simple model for scanning tunneling spectroscopy of noble metal surfaces with adsorbed Kondo impurities. *Physical Review B*, 69(11):115404, Mar 2004.
- [104] N. Néel, J. Kröger, L. Limot, K. Palotas, W. A. Hofer, and R. Berndt. Conductance and Kondo effect in a controlled single-atom contact. *Physical Review Letters*, 98(1):016801, 2007.
- [105] P. Wahl, P. Simon, L. Diekhöner, V. S. Stepanyuk, P. Bruno, M. A. Schneider, and K. Kern. Exchange interaction between single magnetic adatoms. *Physical Review Letters*, 98(5):056601, 2007.
- [106] Markus Ternes, Andreas J Heinrich, and Wolf-Dieter Schneider. Spectroscopic manifestations of the kondo effect on single adatoms. *Journal of Physics: Condensed Matter*, 21(5):053001 (19pp), 2009.
- [107] H. C. Manoharan, C. P. Lutz, and D. M. Eigler. Quantum mirages formed by coherent projection of electronic structure. *Nature*, 403:512–515, 2000.
- [108] P. Gambardella, S. Rusponi, M. Veronese, S. S. Dhesi, C. Grazioli, A. Dallmeyer, I. Cabria, R. Zeller, P. H. Dederichs, K. Kern, C. Carbone, and H. Brune. Giant magnetic anisotropy of single cobalt atoms and nanoparticles. *Science*, 300(5622):1130–1133, 2003.
- [109] M. A. Ruderman and C. Kittel. Indirect exchange coupling of nuclear magnetic moments by conduction electrons. *Physical Review*, 96(1):99, Oct 1954.
- [110] Tadao Kasuya. A theory of metallic ferro- and antiferromagnetism on Zener’s model. *Progress of Theoretical Physics*, 16(1):45–57, 1956.
- [111] Kei Yosida. Magnetic properties of Cu-Mn alloys. *Physical Review*, 106(5):893–898, Jun 1957.
- [112] B. Lazarovits, L. Szunyogh, and P. Weinberger. Spin-polarized surface states close to adatoms on Cu(111). *Physical Review B (Condensed Matter and Materials Physics)*, 73(4):045430, 2006.
- [113] J. W. Gadzuk. Resonance-tunneling spectroscopy of atoms adsorbed on metal surfaces: Theory. *Physical Review B*, 1(5):2110–2129, Mar 1970.
- [114] Robert Gomer and Lynn W. Swanson. Theory of field desorption. *The Journal of Chemical Physics*, 38(7):1613–1629, 1963.
- [115] Alan J. Bennett and L. M. Falicov. Theory of the electronic configuration of a metallic surface-

- adsorbate system. *Physical Review*, 151(2):512–518, Nov 1966.
- [116] Barry Simon. The bound state of weakly coupled Schrödinger operators in one and two dimensions. *Ann. Physics*, 97(2):279–288, 1976.
- [117] E. Zaremba, I. Nagy, and P. M. Echenique. Nonlinear screening in two-dimensional electron gases. *Physical Review Letters*, 90(4):046801, Jan 2003.
- [118] J. Kliewer, R. Berndt, and S. Crampin. Controlled modification of individual adsorbate electronic structure. *Physical Review Letters*, 85(23):4936–4939, Dec 2000.
- [119] P. W. Anderson. Localized magnetic states in metals. *Physical Review*, 124(1):41–53, Oct 1961.
- [120] Eleftherios N. Economou. *Green's functions in quantum physics*, volume 7 of *Springer series in solid state sciences*. Springer, Berlin, 1983.
- [121] Samir Lounis, Phivos Mavropoulos, Peter H. Dederichs, and Stefan Blügel. Surface-state scattering by adatoms on noble metals: Ab initio calculations using the Korringa-Kohn-Rostoker Green function method. *Physical Review B (Condensed Matter and Materials Physics)*, 73(19):195421, 2006.
- [122] Werner A. Hofer, Krisztián Palotás, Stefano Rusponi, Tristan Cren, and Harald Brune. Role of hydrogen in giant spin polarization observed on magnetic nanostructures. *Physical Review Letters*, 100(2):026806, 2008.
- [123] P. X. Xu, V. M. Karpan, K. Xia, M. Zwierzycki, I. Marushchenko, and P. J. Kelly. Influence of roughness and disorder on tunneling magnetoresistance. *Physical Review B (Condensed Matter and Materials Physics)*, 73(18):180402, 2006.
- [124] J. Enkovaara, D. Wortmann, and S. Blügel. Spin-polarized tunneling between an antiferromagnet and a ferromagnet: First-principles calculations and transport theory. *Physical Review B*, 76(5):054437, Aug 2007.
- [125] Benjamin W. Heinrich, Cristian Iacovita, Thomas Brumme, Deung-Jang Choi, Laurent Limot, Mircea V. Rastei, Werner A. Hofer, Jens Kortus, and Jean-Pierre Bucher. Direct observation of the tunneling channels of a chemisorbed molecule. *The Journal of Physical Chemistry Letters*, 1:1517–1523, 2010.
- [126] A. Braun and J. Tcherniac. Über die Produkte der Einwirkung von Acetanhydrid auf Phthalamid. *Berichte der deutschen chemischen Gesellschaft*, 40:2709, 1907.
- [127] Henri de Diesbach and Edmond von der Weid. Quelques sels complexes des o-dinitriles avec le cuivre et la pyridine. *Helvetica Chimica Acta*, 10:886, 1927.
- [128] J. Monteath Robertson and Ida Woodward. An X-ray study of the phthalocyanines. Part III. Quantitative structure determination of nickel phthalocyanine. *Journal of the Chemical Society*, page 219, 1937.

- [129] J.K. Gimzewski, E. Stoll, and R.R. Schlittler. Scanning tunneling microscopy of individual molecules of copper phthalocyanine adsorbed on polycrystalline silver surfaces. *Surface Science*, 181(1-2):267 – 277, 1987.
- [130] P. H. Lippel, R. J. Wilson, M. D. Miller, Ch. Wöll, and S. Chiang. High-resolution imaging of copper-phthalocyanine by scanning-tunneling microscopy. *Physical Review Letters*, 62(2):171–174, Jan 1989.
- [131] C. Ludwig, R. Strohmaier, J. Petersen, B. Gompf, and W. Eisenmenger. Epitaxy and scanning tunneling microscopy image contrast of copper-phthalocyanine on graphite and MoS₂. *Journal of Vacuum Science and Technology B*, 12(3):1963–1966, 1994.
- [132] Matthias Böhringer, Richard Berndt, and Wolf-Dieter Schneider. Transition from three-dimensional to two-dimensional faceting of Ag(110) induced by Cu-phthalocyanine. *Physical Review B*, 55(3):1384–1387, Jan 1997.
- [133] K. W. Hipps, Xing Lu, X. D. Wang, and Ursula Mazur. Metal d-orbital occupation-dependent images in the scanning tunneling microscopy of metal phthalocyanines. *Journal of Physical Chemistry*, 100(27):11207, 1996.
- [134] Xing Lu, K. W. Hipps, X. D. Wang, and Ursula Mazur. Scanning tunneling microscopy of metal phthalocyanines: d7 and d9 cases. *Journal of the American Chemical Society*, 118:7197, 1996.
- [135] L. Scudiero, K. W. Hipps, and Dan E. Barlow. A self-organized two-dimensional bimolecular structure. *Journal of Physical Chemistry B*, 107:2903–2909, 2003.
- [136] Koji Suto, Soichiro Yoshimoto, and Kingo Itaya. Two-dimensional self-organization of phthalocyanine and porphyrin: Dependence on the crystallographic orientation of Au. *Journal of the American Chemical Society*, 125:14976, 2003.
- [137] J. Kröger, H. Jensen, N. Néel, and R. Berndt. Self-organization of cobalt-phthalocyanine on a vicinal gold surface revealed by scanning tunneling microscopy. *Surface Science*, 601:4180, 2007.
- [138] A. B. P. Lever (Editor) C. C. Leznoff (Editor). *Phthalocyanines, Properties and Applications*. Wiley, 1998.
- [139] B. Crone, A. Dodabalapur, Y.-Y. Lin, R. W. Filas, Z. Bao, A. LaDuca, R. Sarpeshkar, H. E. Katz, and W. Li. Large-scale complementary integrated circuits based on organic transistors. *Nature*, 403:521, 2001.
- [140] J. Blochwitz, M. Pfeiffer, T. Fritz, and K. Leo. Low voltage organic light emitting diodes featuring doped phthalocyanine as hole transport material. *Applied Physics Letters*, 73(6):729–731, 1998.
- [141] Andreas Hirth, Ulrike Michelsen, and Dieter Wöhrle. Photodynamische Tumorthherapie. *Chemie in unserer Zeit*, 33(2):84, 1999.

-
- [142] A. Scheybal, T. Ramsvik, R. Bertschinger, M. Putero, F. Nolting, and T. A. Jung. Induced magnetic ordering in a molecular monolayer. *Chemical Physics Letters*, 411:214–220, 2005.
- [143] H. Wende, M. Bernien, J. Luo, C. Sorg, N. Ponpandian, J. Kurde, J. Miguel, M. Piantek, X. Xu, Ph. Eckhold, W. Kuch, K. Baberschke, P. M. Panchmatia, B. Sanyal, P. M. Oppeneer, and O. Eriksson. Substrate-induced magnetic ordering and switching of iron porphyrin molecules. *Nature Materials*, 6:516, 2007.
- [144] J. A. A. W. Elemans, R. van Hameren, R. J. M. Nolte, and A. E. Rowan. Molecular materials by self-assembly of porphyrins, phthalocyanines, and perylenes. *Advanced Materials*, 18(10):1251, 2006.
- [145] L. Gao, W. Ji, Y. B. Hu, Z. H. Cheng, Z. T. Deng, Q. Liu, N. Jiang, X. Lin, W. Guo, S. X. Du, W. A. Hofer, X. C. Xie, and H.-J. Gao. Site-specific Kondo effect at ambient temperatures in iron-based molecules. *Physical Review Letters*, 99(10):106402, 2007.
- [146] G. V. Nazin, X. H. Qiu, and W. Ho. Visualization and spectroscopy of a metal-molecule-metal bridge. *Science*, 302(5642):77, 2003.
- [147] Violeta Iancu, Aparna Deshpande, and Saw-Wai Hla. Manipulation of the Kondo effect via two-dimensional molecular assembly. *Physical Review Letters*, 97(26):266603, 2006.
- [148] X. H. Qiu, G. V. Nazin, and W. Ho. Mechanisms of reversible conformational transitions in a single molecule. *Physical Review Letters*, 93(19):196806, Nov 2004.
- [149] Violeta Iancu, Aparna Deshpande, and Saw-Wai Hla. Manipulating Kondo temperature via single molecule switching. *Nano Letters*, 6(4):820, 2006.
- [150] Y. Wang, J. Kröger, R. Berndt, and W. A. Hofer. Pushing and pulling a Sn ion through an adsorbed phthalocyanine molecule. *Journal of the American Chemical Society*, 131:3639, 2009.
- [151] Willi Auwärter, Florian Klappenberger, Alexander Weber-Bargioni, Agustin Schiffrin, Thomas Strunskus, Christof Wöll, Yan Penec, Andreas Riemann, and Johannes V. Barth. Conformational adaptation and selective adatom capturing of tetrapyrrolyl-porphyrin molecules on a copper (111) surface. *Journal of the American Chemical Society*, 129(36):11279, 2007.
- [152] Christoph Stadler, Sören Hansen, Ingo Kröger, Christian Kumpf, and Eberhard Umbach. Tuning intermolecular interaction in long-range-ordered submonolayer organic films. *Nature Physics*, 5:153, 2009.
- [153] Y. Wang, X. Ge, C. Manzano, J. Kröger, R. Berndt, W. A. Hofer, H. Tang, and J. Cerda. Supramolecular patterns controlled by electron interference and direct intermolecular interactions. *Journal of the American Chemical Society*, 131:10400, 2009.
- [154] Jascha Repp, Gerhard Meyer, Sladjana M. Stojković, André Gourdon, and Christian Joachim. Molecules on insulating films: Scanning-tunneling microscopy imaging of individual molecular orbitals. *Physical Review Letters*, 94(2):026803, 2005.

- [155] Gerhard Meyer, Sven Zöphel, and Karl-Heinz Rieder. Scanning tunneling microscopy manipulation of native substrate atoms: A new way to obtain registry information on foreign adsorbates. *Physical Review Letters*, 77(10):2113, 1996.
- [156] Kai-Felix Braun and Saw-Wai Hla. Probing the conformation of physisorbed molecules at the atomic scale using STM manipulation. *Nano Letters*, 5(1):73–76, 2005.
- [157] P. Sautet and M.-L. Bocquet. Shape of molecular adsorbates in STM images: A theoretical study of benzene on Pt(111). *Physical Review B*, 53(8):4910, Feb 1996.
- [158] Wende Xiao, Xinliang Feng, Pascal Ruffieux, Oliver Gröning, Klaus Müllen, and Roman Fasel. Self-assembly of chiral molecular honeycomb networks on Au(111). *Journal of the American Chemical Society*, 130:8910, 2008.
- [159] Roman Fasel, Manfred Parschau, and Karl-Heinz Ernst. Chirality transfer from single molecules into self-assembled monolayers. *Angewandte Chemie International Edition*, 42(42):5178, 2009.
- [160] Franck Vidal, Erik Delvigne, Sebastian Stepanow, Nian Lin, Johannes V. Barth, and Klaus Kern. Chiral phase transition in two-dimensional supramolecular assemblies of prochiral molecules. *Journal of the American Chemical Society*, 127(28):10101–10106, 2005.
- [161] Shih-Hsin Chang, Stefan Kuck, Jens Brede, Leonid Lichtenstein, Germar Hoffmann, and Roland Wiesendanger. Symmetry reduction of metal phthalocyanines on metals. *Physical Review B*, 78(23):233409, 2008.
- [162] PWSCF is part of the QUANTUM-ESPRESSO package distributed by S. Baroni, A. Dal Corso, S. de Gironcoli, P. Giannozzi, C. Cavazzoni, G. Ballabio, S. Scandolo, G. Chiarotti, P. Focher, A. Pasquarello, K. Laasonen, A. Trave, R. Car, N. Marzari, A. Kokalj, <http://www.pwscf.org/>.
- [163] M.-L. Bocquet, H. Lesnard, and N. Lorente. Inelastic spectroscopy identification of STM-induced benzene dehydrogenation. *Physical Review Letters*, 96(9):096101, 2006.
- [164] H. Lesnard, N. Lorente, and M.-L. Bocquet. Theoretical study of benzene and pyridine STM-induced reactions on copper surfaces. *Journal of Physics: Condensed Matter*, 20(22):224012, 2008.
- [165] Jérôme Lagoute, Kiyoshi Kanisawa, and Stefan Fölsch. Manipulation and adsorption-site mapping of single pentacene molecules on Cu(111). *Physical Review B*, 70(24):245415, Dec 2004.
- [166] Jérôme Lagoute and Stefan Fölsch. Interaction of single pentacene molecules with monatomic Cu/Cu(111) quantum wires. *Journal of Vacuum Science and Technology B*, 23(4):1726, 2005.
- [167] N. Atodiresei, V. Caciuc, P. Lazić, and S. Blügel. Chemical versus Van der Waals interaction: The role of the heteroatom in the flat absorption of aromatic molecules C_6H_6 , C_5NH_5 , and $C_4N_2H_4$ on the Cu(110) Surface. *Physical Review Letters*, 102(13):136809, 2009.
- [168] S. Fölsch, P. Hyldgaard, R. Koch, and K. H. Ploog. Quantum confinement in monatomic Cu chains on Cu(111). *Physical Review Letters*, 92(5):056803, Feb 2004.

-
- [169] Jérôme Lagoute, Xi Liu, and Stefan Fölsch. Electronic properties of straight, kinked, and branched Cu/Cu(111) quantum wires: A low-temperature scanning tunneling microscopy and spectroscopy study. *Physical Review B*, 74(12):125410, 2006.
- [170] Krisztian Palotas and Werner A Hofer. Multiple scattering in a vacuum barrier obtained from real-space wavefunctions. *Journal of Physics: Condensed Matter*, 17(17):2705, 2005.
- [171] W. A. Hofer and A. Garcia-Lekue. Differential tunneling spectroscopy simulations: Imaging surface states. *Physical Review B*, 71(8):085401, 2005.
- [172] Jochen Heyd, Gustavo E. Scuseria, and Matthias Ernzerhof. Hybrid functionals based on a screened Coulomb potential. *Journal of Chemical Physics*, 118(18):8207, 2003.
- [173] G. Kresse and J. Hafner. Ab initio molecular dynamics for liquid metals. *Physical Review B*, 47(1):558, Jan 1993.
- [174] G. Kresse and D. Joubert. From ultrasoft pseudopotentials to the projector augmented-wave method. *Physical Review B*, 59(3):1758, Jan 1999.
- [175] W. A. Hofer and A. J. Fisher. Signature of a chemical bond in the conductance between two metal surfaces. *Physical Review Letters*, 91(3):036803, Jul 2003.
- [176] L. Limot, J. Kröger, R. Berndt, A. Garcia-Lekue, and W. A. Hofer. Atom transfer and single-atom contacts. *Physical Review Letters*, 94(12):126102, 2005.
- [177] Aidi Zhao, Qunxiang Li, Lan Chen, Hongjun Xiang, Weihua Wang, Shuan Pan, Bing Wang, Xudong Xiao, Jinlong Yang, J. G. Hou, and Qingshi Zhu. Controlling the kondo effect of an adsorbed magnetic ion through its chemical bonding. *Science*, 309(5740):1542, 2005.
- [178] M. Takada and H Tada. Scanning tunneling microscopy and spectroscopy of phthalocyanine molecules on metal surfaces. *Japanese Journal of Applied Physics*, 44:5332, 2005.
- [179] D. E. Barlow, L. Scudiero, and K. W. Hipps. Scanning tunneling microscopy study of the structure and orbital mediated tunneling spectra of Co(II) phthalocyanine and Co(II) tetraphenylporphyrin on Au(111): mixed composition films. *Langmuir*, 20:4413, 2004.
- [180] A. F. Takacs, F. Witt, S. Schmaus, T. Balashov, M. Bowen, E. Beaurepaire, and W. Wulfhekel. Electron transport through single phthalocyanine molecules studied using scanning tunneling microscopy. *Physical Review B*, 78(23):233404, 2008.
- [181] Buchner, Florian and Warnick, Karl-Georg and Wölfle, Thorsten and Görling, Andreas and Steinrück, Hans-Peter and Hieringer, Wolfgang and Marbach, Hubertus. Chemical fingerprints of large organic molecules in scanning tunneling microscopy: Imaging adsorbate-substrate coupling of metalloporphyrins. *The Journal of Physical Chemistry C*, 113(37):16450–16457, 2009.
- [182] W. A. Hofer and A. Garcia-Lekue. Differential tunneling spectroscopy simulations: Imaging surface states. *Physical Review B*, 71(8):085401, 2005.
- [183] Alexandre R. Rocha, Víctor M. García-suárez, Steve W. Bailey, Colin J. Lambert, Jaime Ferrer,

- and Stefano Sanvito. Towards molecular spintronics. *Nature Materials*, 4:335–339, 2005.
- [184] Lapo Bogani and Wolfgang Wernsdorfer. Molecular spintronics using single-molecule magnets. *Nature Materials*, 7:179–186, 2008.
- [185] Kazuhito Tsukagoshi, Bruce W. Alphenaar, and Hiroki Ago. Coherent transport of electron spin in a ferromagnetically contacted carbon nanotube. *Nature*, 401:572–574, 1999.
- [186] J. R. Petta, S. K. Slater, and D. C. Ralph. Spin-dependent transport in molecular tunnel junctions. *Physical Review Letters*, 93(13):136601, Sep 2004.
- [187] Guillemín Rodary, Sebastian Wedekind, Dirk Sander, and Jürgen Kirschner. Magnetic hysteresis loop of single Co nano-islands. *Japanese Journal of Applied Physics*, 47(12):9013–9015, 2008.
- [188] N. Néel, J. Kröger, L. Limot, and R. Berndt. Conductance of oriented C₆₀ molecules. *Nano Letters*, 8(5):1291–1295, 2008.
- [189] J. Kröger, N. Néel, and L. Limot. Contact to single atoms and molecules with the tip of a scanning tunnelling microscope. *Journal of Physics: Condensed Matter*, 20:223001, 2008.
- [190] Eiji Osawa. Superaromaticity. *Kagaku*, 25:854–863, 1970.
- [191] Donald B. Boyd and Zdenek Slanina. Introduction and foreword to the special issue commemorating the thirtieth anniversary of Eiji Osawa's C₆₀ paper. *Journal of Molecular Graphics and Modelling*, 19(2):181–184, 2001.
- [192] H. W. Kroto, J. R. Heath, S. C. O'Brien, R. F. Curl, and R. E. Smalley. C₆₀: Buckminsterfullerene. *Nature*, 318:162–163, 1985.
- [193] W. Krätschmer, Lowell D. Lamb, K. Fostiropoulos, and Donald R. Huffman. Solid C₆₀: a new form of carbon. *Nature*, 347:354–358, 1990.
- [194] Hongkun Park, Jiwoong Park, Andrew K. L. Lim, Erik H. Anderson, A. Paul Alivisatos, and Paul L. McEuen. Nanomechanical oscillations in a single-C₆₀ transistor. *Nature*, 407:57–60, 2000.
- [195] C. Joachim and J. K. Gimzewski. An electromechanical amplifier using a single molecule. *Chemical Physics Letters*, 265(3-5):353 – 357, 1997.
- [196] N. Néel, J. Kröger, L. Limot, T. Frederiksen, M. Brandbyge, and R. Berndt. Controlled contact to a C₆₀ molecule. *Physical Review Letters*, 98(6):065502, Feb 2007.
- [197] R. Yamachika, M. Grobis, A. Wachowiak, and M. F. Crommie. Controlled atomic doping of a single C₆₀ molecule. *Science*, 304(5668):281–284, 2004.
- [198] G. Schulze, K. J. Franke, A. Gagliardi, G. Romano, C. S. Lin, A. L. Rosa, T. A. Niehaus, Th. Frauenheim, A. Di Carlo, A. Pecchia, and J. I. Pascual. Resonant electron heating and molecular phonon cooling in single C₆₀ junctions. *Physical Review Letters*, 100(13):136801, Apr 2008.
- [199] J. L. Wragg, J. E. Chamberlain, H. W. White, W. Krätschmer, and Donald R. Huffman. Scanning tunnelling microscopy of solid C₆₀/C₇₀. *Nature*, 348:623–624, 1990.

-
- [200] Y. Z. Li, J. C. Patrin, M. Chander, J. H. Weaver, L. P. F. Chibante, and R. E. Smalley. Ordered overlayers of C_{60} on GaAs(110) studied with scanning tunneling microscopy. *Science*, 252(5005):547–548, 1991.
- [201] Tomihiro Hashizume, K. Motai, X. D. Wang, H. Shinohara, Y. Saito, Y. Maruyama, K. Ohno, Y. Kawazoe, Y. Nishina, H. W. Pickering, Y. Kuk, and T. Sakurai. Intramolecular structures of C_{60} molecules adsorbed on the Cu(111)-(1 × 1) surface. *Physical Review Letters*, 71(18):2959–2962, Nov 1993.
- [202] ISI Web of Knowledge found 137 articles for the topic " C_{60} and STM". For some selected examples see Refs. [13, 15, 196, 198, 204], and references therein.
- [203] Changgan Zeng, Haiqian Wang, Bing Wang, Jinlong Yang, and J. G. Hou. Negative differential-resistance device involving two C_{60} molecules. *Applied Physics Letters*, 77(22):3595–3597, 2000.
- [204] Nilay A. Pradhan, Ning Liu, and Wilson Ho. Vibronic spectroscopy of single C_{60} molecules and monolayers with the STM. *The Journal of Physical Chemistry B*, 109(17):8513–8518, 2005.
- [205] Leo Esaki. New phenomenon in narrow germanium $p-n$ junctions. *Physical Review*, 109(2):603 – 604, Jan 1958.
- [206] Ivar Giaever. Electron tunneling between two superconductors. *Physical Review Letters*, 5(10):464–466, Nov 1960.
- [207] L. Esaki and P. J. Stiles. New type of negative resistance in barrier tunneling. *Physical Review Letters*, 16(24):1108–1111, Jun 1966.
- [208] R. Tsu and L. Esaki. Tunneling in a finite superlattice. *Applied Physics Letters*, 22(11):562–564, 1973.
- [209] L. L. Chang, L. Esaki, and R. Tsu. Resonant tunneling in semiconductor double barriers. *Applied Physics Letters*, 24(12):593–595, 1974.
- [210] Leo Esaki. Long journey into tunneling. *Review of Modern Physics*, 46(2):237–244, Apr 1974.
- [211] S. Sze. *Physics of Semiconductor Devices*. Wiley, New York, 1981.
- [212] L.L. Chang, E.E. Mendez, and C. Tejedor, editors. *Resonant Tunneling in Semiconductors*. Plenum, New York, 1991.
- [213] J. Chen, M. A. Reed, A. M. Rawlett, and J. M. Tour. Large On-Off Ratios and Negative Differential Resistance in a Molecular Electronic Device. *Science*, 286(5444):1550–1552, 1999.
- [214] J. Chen, W. Wang, M. A. Reed, A. M. Rawlett, D. W. Price, and J. M. Tour. Room-temperature negative differential resistance in nanoscale molecular junctions. *Applied Physics Letters*, 77(8):1224–1226, 2000.
- [215] Ronald A. Wassel, Grace M. Credo, Ryan R. Fuieler, Daniel L. Feldheim, and Christopher B. Gorman. Attenuating negative differential resistance in an electroactive self-assembled monolayer-based junction. *Journal of the American Chemical Society*, 126(1):295–300, 2004.

- [216] Adi Salomon, Rina Arad-Yellin, Abraham Shanzer, Amir Karton, and David Cahen. Stable room-temperature molecular negative differential resistance based on molecule-electrode interface chemistry. *Journal of the American Chemical Society*, 126(37):11648–11657, 2004.
- [217] Z. H. Lu, R. S. Khangura, M. W.C. Dharma-wardana, Marek Z. Zgierski, and Douglas Ritchie. Molecular electronics, negative differential resistance, and resonant tunneling in a poled molecular layer on Al/LiF electrodes having a sharp density of states. *Applied Physics Letters*, 85(2):323–325, 2004.
- [218] Takuji Komura, Takafumi Yao, and Masamichi Yoshimura. Atomic and electronic structures of rebonded *B*-type steps on the *Si*(001) – 2×1 surface. *Physical Review B*, 56(7):3579–3582, Aug 1997.
- [219] Christopher B. Gorman, Richard L. Carroll, and Ryan R. Fuieler. Negative differential resistance in patterned electroactive self-assembled monolayers. *Langmuir*, 17(22):6923–6930, 2001.
- [220] Yongqiang Xue, Supriyo Datta, Seunghun Hong, R. Reifenger, Jason I. Henderson, and Clifford P. Kubiak. Negative differential resistance in the scanning-tunneling spectroscopy of organic molecules. *Physical Review B*, 59(12):R7852–R7855, Mar 1999.
- [221] Fu-Ren F. Fan, Jiping Yang, Lintao Cai, David W. Price Jr., Shawn M. Dirk, Dmitry V. Kosynkin, Yuxing Yao, Adam M. Rawlett, James M. Tour, and Allen J. Bard. Charge transport through self-assembled monolayers of compounds of interest in molecular electronics. *Journal of the American Chemical Society*, 124(19):5550–5560, 2002.
- [222] Bing Wang, Kedong Wang, Wei Lu, Haiqian Wang, Zhenyu Li, Jinlong Yang, and J. G. Hou. Effects of discrete energy levels on single-electron tunneling in coupled metal particles. *Applied Physics Letters*, 82(21):3767–3769, 2003.
- [223] G. Buchs, P. Ruffieux, P. Gröning, and O. Gröning. Defect-induced negative differential resistance in single-walled carbon nanotubes. *Applied Physics Letters*, 93(7):073115, 2008.
- [224] Nathan P. Guisinger, Mark E. Greene, Rajiv Basu, Andrew S. Baluch, and Mark C. Hersam. Room temperature negative differential resistance through individual organic molecules on silicon surfaces. *Nano Letters*, 4(1):55–59, 2004.
- [225] T. Yakabe, Z. C. Dong, and H. Nejoh. Observation of negative differential resistance on Ag/Si(100) using STM. *Applied Surface Science*, 121-122:187–190, 1997. Iketani-6.
- [226] J. Gaudio, L. J. Lauhon, and W. Ho. Vibrationally mediated negative differential resistance in a single molecule. *Physical Review Letters*, 85(9):1918–1921, Aug 2000.
- [227] Jennifer Gaudio and Wilson Ho. Steric turnoff of vibrationally mediated negative differential resistance in a single molecule. *Angewandte Chemie International Edition*, 40(21):4080–4082, 2001.
- [228] Isabel Fernandez Torrente, Katharina J. Franke, and Jose Ignacio Pascual. Spectroscopy of C₆₀

- single molecules: the role of screening on energy level alignment. *Journal of Physics: Condensed Matter*, 20(18):184001 (11pp), 2008.
- [229] Anirban Bandyopadhyay and Y. Wakayama. Origin of negative differential resistance in molecular junctions of Rose Bengal. *Applied Physics Letters*, 90(2):023512, 2007.
- [230] Jin He and Stuart M. Lindsay. On the mechanism of negative differential resistance in ferrocenylundecanethiol self-assembled monolayers. *Journal of the American Chemical Society*, 127(34):11932–11933, 2005.
- [231] Woo Youn Kim, S. K. Kwon, and Kwang S. Kim. Negative differential resistance of carbon nanotube electrodes with asymmetric coupling phenomena. *Physical Review B*, 76(3):033415, Jul 2007.
- [232] In-Whan Lyo and Phaedon Avouris. Negative Differential Resistance on the Atomic Scale: Implications for Atomic Scale Devices. *Science*, 245(4924):1369–1371, 1989.
- [233] P. Bedrossian, D. M. Chen, K. Mortensen, and J. A. Golovchenko. Demonstration of the tunnel-diode effect on an atomic scale. *Nature*, 342(2):258–260, 1989.
- [234] C. Wagner, R. Franke, and T. Fritz. Evaluation of $I(V)$ curves in scanning tunneling spectroscopy of organic nanolayers. *Physical Review B*, 75(23):235432, Jun 2007.
- [235] C. J. Chen. *Introduction to Scanning Tunneling Microscopy*. Oxford University Press, Oxford, 1993.
- [236] Guillaume Schull, Thomas Frederiksen, Mads Brandbyge, and Richard Berndt. Passing current through touching molecules. *Physical Review Letters*, 103(20):206803, Nov 2009.
- [237] M. Sicot, O. Kurnosikov, O. A. O. Adam, H. J. M. Swagten, and B. Koopmans. Stm-induced desorption of hydrogen from co nanoislands. *Physical Review B*, 77(3):035417, Jan 2008.
- [238] N. Néel, L. Limot, J. Kröger, and R. Berndt. Rotation of C_{60} in a single-molecule contact. *Physical Review B*, 77(12):125431, Mar 2008.
- [239] G. Schull and R. Berndt. Orientationally ordered (7×7) superstructure of C_{60} on Au(111). *Physical Review Letters*, 99(22):226105, Nov 2007.
- [240] Eric I. Altman and Richard J. Colton. Determination of the orientation of C_{60} adsorbed on Au(111) and Ag(111). *Physical Review B*, 48(24):18244–18249, Dec 1993.
- [241] C. Silien, N. A. Pradhan, W. Ho, and P. A. Thiry. Influence of adsorbate-substrate interaction on the local electronic structure of C_{60} studied by low-temperature stm. *Physical Review B*, 69(11):115434, Mar 2004.
- [242] Woei Wu Pai, Ching-Ling Hsu, M. C. Lin, K. C. Lin, and T. B. Tang. Structural relaxation of adlayers in the presence of adsorbate-induced reconstruction: $C_{60}/Cu(111)$. *Physical Review B*, 69(12):125405, Mar 2004.
- [243] Woei Wu Pai, H. T. Jeng, C.-M. Cheng, C.-H. Lin, Xudong Xiao, Aidi Zhao, Xieqiu Zhang,

- Geng Xu, X. Q. Shi, M. A. Van Hove, C.-S. Hsue, and K.-D. Tsuei. Optimal electron doping of a C_{60} monolayer on Cu(111) via interface reconstruction. *Physical Review Letters*, 104(3):036103, Jan 2010.
- [244] M. Grobis, X. Lu, and M. F. Crommie. Local electronic properties of a molecular monolayer: C_{60} on Ag(001). *Physical Review B*, 66(16):161408, Oct 2002.
- [245] Xinghua Lu, M. Grobis, K. H. Khoo, Steven G. Louie, and M. F. Crommie. Spatially mapping the spectral density of a single C_{60} molecule. *Physical Review Letters*, 90(9):096802, Mar 2003.
- [246] M. Passoni, F. Donati, A. Li Bassi, C. S. Casari, and C. E. Bottani. Recovery of local density of states using scanning tunneling spectroscopy. *Physical Review B*, 79(4):045404, Jan 2009.
- [247] Katharina J. Franke, Gunnar Schulze, and Jose Ignacio Pascual. Excitation of Jahn-Teller active modes during electron transport through single C_{60} molecules on metal surfaces. *The Journal of Physical Chemistry Letters*, 1(2):500–504, 2010.
- [248] J. Resh, D. Sarkar, J. Kulik, J. Brueck, A. Xgnatiev, and N.J. Halas. Scanning tunneling microscopy and spectroscopy with fullerene coated tips. *Surface Science Letters*, 316:L1061–L1067, 1994.
- [249] K. F. Kelly, Dipankar Sarkar, Stefano Prato, J. S. Resh, G. D. Hale, and N. J. Halas. Direct observation of fullerene-adsorbed tips by scanning tunneling microscopy. *Journal of Vacuum Science & Technology B: Microelectronics and Nanometer Structures*, 14(2):593–596, 1996.
- [250] Ali Yazdani, D. M. Eigler, and N. D. Lang. Off-Resonance Conduction Through Atomic Wires. *Science*, 272(5270):1921–1924, 1996.
- [251] Ying-Shuang Fu, Shuai-Hua Ji, Xi Chen, Xu-Cun Ma, Rui Wu, Chen-Chen Wang, Wen-Hui Duan, Xiao-Hui Qiu, Bo Sun, Ping Zhang, Jin-Feng Jia, and Qi-Kun Xue. Manipulating the kondo resonance through quantum size effects. *Physical Review Letters*, 99(25):256601, Dec 2007.
- [252] C. H. Schwalb, S. Sachs, M. Marks, A. Schöll, F. Reinert, E. Umbach, and U. Höfer. Electron lifetime in a Shockley-type metal-organic interface state. *Physical Review Letters*, 101(14):146801, Sep 2008.
- [253] Saw-Wai Hla, Ludwig Bartels, Gerhard Meyer, and Karl-Heinz Rieder. Inducing all steps of a chemical reaction with the scanning tunneling microscope tip: Towards single molecule engineering. *Physical Review Letter*, 85(13):2777–2780, Sep 2000.
- [254] Y. Okawa and M. Aono. Linear chain polymerization initiated by a scanning tunneling microscope tip at designated positions. *Journal of Chemical Physics*, 115(5):2317, 2001.
- [255] Peter Liljeroth, Jascha Repp, and Gerhard Meyer. Current-induced hydrogen tautomerization and conductance switching of naphthalocyanine molecules. *Science*, 317(5842):1203–1206, 2007.

- [256] Satoshi Katano, Yousoo Kim, Masafumi Hori, Michael Trenary, and Maki Kawai. Reversible control of hydrogenation of a single molecule. *Science*, 316(5833):1883–1886, 2007.
- [257] Sally Brooker and Jonathan A. Kitchen. Nano-magnetic materials: spin crossover compounds vs. single molecule magnets vs. single chain magnets. *Dalton Transactions*, 36:7317–7560, 2009.

List of Figures

1.1	Scheme of the STM tunnel junction	4
1.2	Manipulated atom images of Cu(111)	5
1.3	Constant-height versus constant-current images	7
1.4	Principle of spin-polarized STM	9
1.5	Homebuilt evaporators	11
2.1	Phase variation upon reflection as a function of energy for the L gap in Cu(111)	15
2.2	Shockley surface state of Cu(111)	16
2.3	Differential conductance over Cu(111)	17
2.4	Standing wave pattern of the Shockley surface state on Cu(111)	18
2.5	Two-monolayer-high cobalt nanoislands of different size and stacking on Cu(111)	19
2.6	Calculated diffusion barriers for the adatom diffusion along the island edges and corners	20
2.7	dI/dV spectra acquired over Cu(111), faulted and unfaulted cobalt islands . .	21
2.8	Spectral Density Maps and spin-polarized LDOS of cobalt islands	22
2.9	dI/dV and dI/dV asymmetry maps of the same Co island	23
2.10	Spin-polarized dI/dV spectra acquired above two Co nanoislands on Cu(111) .	24
2.11	dI/dV on unfaulted nanoislands of increasing size	26
2.12	The position of P1 versus the island size	27
2.13	Study of the relation between peak position and tip position above the island .	28
2.14	Relation between size, interatomic bond length and peak position	29
2.15	Spin-polarized dI/dV map of cobalt nanoislands	33
3.1	Spin-polarized dI/dV by means of an external magnetic field	36

3.2	SP dI/dV spectra over two Co islands with opposite spin orientation and over Fe and Cr adatoms	37
3.3	Constant-current STM image of a faulted cobalt nanoisland after the transfer of a Cu atom from the tip apex to its center	38
3.4	dI/dV over a Co nanoisland and over various adatoms	40
3.5	Copper adatoms on Cu(111)	41
3.6	dI/dV spectra over the (111) surface of copper and over Ni, Co and Cu adatoms	42
3.7	Energy-level diagram for the interaction of an adatom level with an electronic band of a metal substrate	43
3.8	Adatom DOS	45
3.9	Setup for the LDOS calculation above the atoms and islands	46
3.10	Calculated spin-polarized LDOS of transition-metal adatoms residing on faulted cobalt nanoislands	47
3.11	Calculated spin-polarization above clean cobalt nanoislands and individual atoms	49
4.1	Chemical structure of CoPc	54
4.2	Isosurface plots of CoPc in vacuum	55
4.3	Topographic images of isolated CoPc molecules residing on Cu(111)	57
4.4	Determination of the adsorption site of CoPc on Cu(111)	58
4.5	Adsorption optimization of CoPc on Cu(111) by DFT	59
4.6	Constant-height dI/dV spectra of CoPc on Cu(111)	63
4.7	Constant-height dI/dV maps over CoPc	64
4.8	Calculated pDOS of the CoPc/Cu(111) system	66
4.9	Isosurface plots at selected energies	68
4.10	Calculated dI/dV maps over an isolated CoPc	69
4.11	CoPc molecules on cobalt nanoislands grown on Cu(111)	71
4.12	Adsorption optimization by DFT	72
4.13	pDOS over CoPc and the cobalt surface and Isosurface plot of the magnetization density	73
4.14	Spin-polarized dI/dV above cobalt nanoislands and CoPc	74
4.15	Spin-polarized tunneling conductance maps for CoPc	75
4.16	Localization of the SP signal at the central Co	77

5.1	C_{60} structure and a LUMO+1 isosurface plot in different orientations	80
5.2	Tunneling barrier dependent NDR	82
5.3	Height dependence of barrier-dependent NDR	83
5.4	Topographic image of C_{60} molecules adsorbed around and on top of cobalt nanoislands	85
5.5	dI/dV over C_{60} on cobalt islands on Cu(111)	86
5.6	Differential conductance at a constant height over C_{60} on cobalt islands	87
5.7	Height-dependent current-voltage characteristics	89
5.8	Simulated dI/dV spectra for one localized state at each electrode	90
5.9	NDR as a function of the energy interval between two sample states.	92
5.10	NDR as a function of the energetic position of the tip state.	94
5.11	Conductance of C_{60} adsorbed on Co islands as calculated by DFT	95
5.12	Different orientations of C_{60} on Cu(111)	97
5.13	Intersection of the LUMO+1 with a spheric $4s$ tip state	98
5.14	Differential conductance of h adsorbed C_{60}	99
5.15	C_{60} -terminated tip	100
5.16	Orientation of C_{60} at the tip apex.	103
5.17	dI/dV spectra above different surfaces by means of a C_{60} -tip	104
5.18	Simulated dI/dV of Cu(111) with a C_{60} -tip	105
5.19	Ferrocene layer with and without adatoms.	110

Symbols, acronyms and abbreviations

A_s	sample state amplitude
A_t	tip state amplitude
β	transfer integral
B_s	background LDOS of the sample
β	transfer integral
$\Delta(E)$	imaginary part of the self energy; instrumental broadening
ΔE_T	thermal broadening
ΔE_M	broadening due to bias modulation
Δx_s	distance between sample states
Γ	inverse lifetime of the surface state
\hbar	reduced Planck constant
$\Lambda(E)$	real part of the self energy
\mathcal{H}	Hamiltonian
μ_B	Bohr magneton
\vec{B}	magnetic field
\vec{M}_s	sample magnetization
\vec{m}_s	difference of the spin-up and spin-down DOS of the sample
\vec{M}_t	tip magnetization
\vec{m}_t	difference of the spin-up and spin-down DOS of the tip
ϕ	phase accumulation
ϕ_B	phase shift for electron reflection at the surface barrier
ϕ_C	phase shift for electron reflection at the crystal barrier
Φ	work function
Φ_s	sample work function
Φ_t	tip work function
ρ_s	sample density of states
ρ_s^\uparrow	spin-up DOS of the sample

ρ_s^\uparrow	spin-up DOS of the sample
ρ_t	tip density of states
ρ_t^\downarrow	spin-down DOS of the tip
ρ_t^\uparrow	spin-up DOS of the tip
$\tilde{\epsilon}_{\mathbf{k}}$	submatrice containing the eigenenergies of the surface states
$\tilde{V}_{a\mathbf{k}}$	coupling matrix elements between the adsorbate level and the surface states
$\uparrow\downarrow$	cobalt islands and CoPc, respectively, defined as antiparallel with respect to the tip magnetization
$\uparrow\uparrow$	cobalt islands and CoPc, respectively, defined as parallel with respect to the tip magnetization
$\epsilon_{\mathbf{q}}$	submatrice containing the eigenenergies of the Bloch bulk states
\vec{k}	wave vector
dI/dV	differential conductance; <i>sometimes</i> : synonymous for $dI/dV(V)$ spectroscopy)
E_F	Fermi energy
G_0	conductance quantum
I	tunneling current
k_B	Boltzmann constant
M	macroscopic mismatch
m_e	electron mass
n_a	projected density of states at the adatom site
n_\downarrow	minority LDOS
n_\uparrow	majority LDOS
n_s	sum of spin-up and spin-down DOS of the sample
n_t	sum of spin-up and spin-down DOS of the tip
P	polarization
r	bond length
rms	root mean square
T	transmission probability <i>or</i> temperature
V	bias; volts
$V_{a\mathbf{q}}$	coupling matrix elements between the adsorbate level and the bulk states
V_m	bias modulation
V_s	sample state energy
V_t	tip state energy
w_s	sample peak width
w_t	tip peak width
z	distance; tip-sample distance; interlayer distance

<i>cf.</i>	confer; <i>engl.</i> compare
<i>e.g.</i>	exempli gratia; <i>engl.</i> for example
<i>etc.</i>	et cetera; <i>engl.</i> and so on
<i>i.e.</i>	id est; <i>engl.</i> that is
a	adsorption on an apex atom
h:h	adsorption on a hexagon-hexagon bond
h:p	adsorption on a hexagon-pentagon bond
h	adsorption on a hexagonal ring
p	adsorption on a pentagonal ring
C_{60}	Buckminsterfullerene (IUPAC name $(C_{60-I_h})[5,6]$ fullerene)
CoPc	Cobalt-Phthalocyanine
Cp	cyclopentadienyl
FeCp ₂	Ferrocene
H ₂ Pc	Phthalocyanine
MPc	metallophthalocyanine
2DEG	two dimensional electron gas
3D	three dimensional
adatom	adsorbed atom
AO	atomic orbital
ARPES	angle-resolved photoemission spectroscopy
C_{60} -tip	STM tip with a C_{60} adsorbed at the tip apex
DFT	density functional theory
DOS	density of states
fcc	face-centered cubic
FWHM	full peak width at half maximum
hcp	hexagonal close-packed
HOMO	highest occupied molecular orbital
HOMO-1	second highest occupied molecular orbital
HOMO-2	third highest occupied molecular orbital
KKR	Korringa-Kohn-Rostoker
KKRY	Ruderman-Kittel-Kasuya-Yoshida
LDA	local density approximation
LDOS	local density of states
LOB	local orbital matching
LUMO	lowest unoccupied molecular orbital
LUMO+1	second lowest unoccupied molecular orbital

LUMO+2	third lowest unoccupied molecular orbital
min.	minute
ML	monolayer
MO	molecular orbital
MTJ	magnetic tunnel junction
n.n.	nearest neighbor
NDR	negative differential conductance
pDOS	partial density of states
Ry	Rydberg
SAM	self assembled monolayers
SP	spin-polarized
SP-STM	spin-polarized scanning tunneling microscopy
SP-STs	spin-polarized scanning tunneling spectroscopy
STM	scanning tunneling microscopy
STs	scanning tunneling spectroscopy
WKB	Wentzel-Kramer-Brillouin

Curriculum Vitae

personal

- Born on June 1st, 1981.
- German citizen.

education

- Ph.D. studies at the Institut de Physique et Chimie des Matériaux de Strasbourg, Nov. 2006 - to date.
- Diplom in Chemistry, University of Leipzig. Title of the diploma thesis: *Grenzflächeneigenschaften und thermische Stabilität eines Fe/SrTiO₃(100)-Kontakts*. Sept. 2006.

teaching

- Assistant for practical courses in Mechanics, 2010.
- Tutorials on Mechanics, 2009 – 2010.
- Assistant for practical courses in Physical Chemistry, 2005 – 2006
- Tutorials on Physical Chemistry, 2003 – 2005.

miscellaneous

- Languages: German, English, French
- Scholarship of the VCI (association of the German Chemical Industries), 2001 – 2003

List of publications

10. Surface state localization within a planar molecule. B. W. HEINRICH, D.-J. CHOI, L. LIMOT, M. V. RASTEI, S. BLÜGEL, AND J. P. BUCHER. in preparation.
9. Tunneling into vertical organometallic wires. B. W. HEINRICH, L. LIMOT, D.-J. CHOI, M. V. RASTEI, M. BOERO, AND J. P. BUCHER. in preparation.
8. Selective atom-capturing by a Ferrocene layer on Cu(111). B. W. HEINRICH, M. V. RASTEI, C. IACOVITA, L. LIMOT, M. BOERO, AND J. P. BUCHER. in preparation.
7. Engineering a negative differential resistance in a single barrier junction. B. W. HEINRICH, L. LIMOT, D.-J. CHOI, M. V. RASTEI, W. A. HOFER, AND J. P. BUCHER. in preparation.
6. Direct observation of the tunneling channels of a chemisorbed molecule. B. W. HEINRICH, C. IACOVITA, T. BRUMME, D.-J. CHOI, L. LIMOT, M. V. RASTEI, W. A. HOFER, J. KORTUS, AND J. P. BUCHER. *The Journal of Physical Chemistry Letters*, 1:1517–1523, April 2010.
5. A spin-selective approach for surface states at Co nanoislands. B. W. HEINRICH, C. IACOVITA, M. V. RASTEI, L. LIMOT, P. A. IGNATIEV, V. S. STEPANYUK, AND J. P. BUCHER. *The European Physical Journal B - Condensed Matter and Complex Systems*, 75:49–56, May 2010.
4. Spin structure of an atomic protrusion: Probing single atoms on cobalt nanoislands. B. W. HEINRICH, C. IACOVITA, M. V. RASTEI, L. LIMOT, J. P. BUCHER, P. A. IGNATIEV, V. S. STEPANYUK, AND P. BRUNO. *Physical Review B*, 79(11):113401–113404, March 2009.
3. Visualizing the spin of individual cobalt-phthalocyanine molecules. C. IACOVITA, M. V. RASTEI, B. W. HEINRICH, T. BRUMME, J. KORTUS, L. LIMOT, AND J. P. BUCHER. *Physical Review Letters*, 101(11):116602, 2008.
2. Size-dependent surface states of strained cobalt nanoislands on Cu(111). M. V. RASTEI, B. HEINRICH, L. LIMOT, P. A. IGNATIEV, V. S. STEPANYUK, P. BRUNO, AND J. P. BUCHER. *Physical Review Letters*, 99(24):246102, 2007.

1. Investigations of FeO films on SrTiO₃(100). B. HEINRICH, A. DEMUND, AND R. SZARGAN. *Physica Status Solidi (c)*, 4:1836 – 1843, 2007.

List of presentations

Oral presentations

- **ACSIN 10** Spin structure of an atomic protrusion: Probing single atoms on cobalt nanoislands; B. W. HEINRICH, C. IACOVITA, M. V. RASTEI, L. LIMOT, J. P. BUCHER, P. A. IGNATIEV, V. S. STEPANYUK, P. BRUNO; 10th International Conference on Atomically Controlled Surfaces, Interfaces and Nanostructures, Granada; September 21st – 25th 2009
- **DPG 2009** Visualizing the spin polarization of individual molecules; BENJAMIN W. HEINRICH, MIRCEA V. RASTEI, CRISTIAN IACOVITA, THOMAS BRUMME, JENS KORTUS, LAURENT LIMOT, AND JEAN-PIERRE BUCHER; 73. Jahrestagung der Deutschen Physikalischen Gesellschaft, Dresden; March 22nd – 27th 2009
- **ECOSS 25** Interplay between strain and spin-polarized states at the nanoscale; B. W. HEINRICH, L. LIMOT, M. V. RASTEI, P. IGNATIEV, V. STEPANYUK, P. BRUNO, AND J. P. BUCHER; 25th European Conference on Surface Science, Liverpool; July 27th to August 1st 2008
- **DPG 2008** Size-dependent Surface States on Strained Cobalt Nanoislands on Cu(111); B. W. HEINRICH, M. V. RASTEI, L. LIMOT, P. A. IGNATIEV, V. S. STEPANYUK, P. BRUNO, AND J. P. BUCHER; 72. Jahrestagung der Deutschen Physikalischen Gesellschaft, Berlin; February 25th – 29th 2008
- **MAGNETIC FIELDS FOR SCIENCE** Thermally activated processes in the Fe/SrTiO₃(100)-system; B. HEINRICH, A. DEMUND, AND R. SZARGAN; International Summer School MAGNETIC FIELDS FOR SCIENCE, Cargese; August 27th to September 8th 2007
- **AOFA 14** Investigations of FeO films on SrTiO₃(100); B. HEINRICH, A. DEMUND, AND R. SZARGAN; 14. Arbeitstagung Angewandte Oberflächenanalytik, Kaiserslautern; September 17th – 20th 2006

Poster presentations

- **ACSIN 10** CoPc chemisorbed on Cu(111): Impact of bonding on transport; B. W. HEINRICH, L. LIMOT, C. IACOVITA, M. V. RASTEI, J.P. BUCHER, W. HOFER, T. BRUMME, AND J. KORTUS; 10th International Conference on Atomically Controlled Surfaces, Interfaces and Nanostructures, Granada; September 21st – 25th 2009
- **IPCMS - ICS** Influence of Atomic Protrusions on a Nanolead Spin Structure; B. W. HEINRICH, C. IACOVITA, M. V. RASTEI, L. LIMOT, J. P. BUCHER, P. A. IGNATIEV, V. S. STEPANYUK, P. BRUNO; Journées scientifiques IPCMS - ICS, Strasbourg; May 4th – 6th 2009
- **DPG 2009** Influence of Atomic Protrusions on a Nanolead Spin Structure; B. W. HEINRICH, C. IACOVITA, M. V. RASTEI, L. LIMOT, J. P. BUCHER, P. A. IGNATIEV, V. S. STEPANYUK, P. BRUNO; 73. Jahrestagung der Deutschen Physikalischen Gesellschaft, Dresden; March 22nd – 27th 2009
- **Nanomaterials and Quantum Metamaterials** Spin-polarized tunneling into single Co-Phthalocyanine molecules; B. W. HEINRICH, C. IACOVITA, M. V. RASTEI, T. BRUMME, J. KORTUS, L. LIMOT, AND J. P. BUCHER; Second French-Korean Physics school on Nanomaterials and Quantum Metamaterials, Seoul; February 9th – 13th 2009
- **JMC11** Polarisation de spin d'atomes individuels; B. W. HEINRICH, C. IACOVITA, M. V. RASTEI, L. LIMOT, J. P. BUCHER, P. A. IGNATIEV, V. S. STEPANYUK, P. BRUNO; 11^{ème} Journées de la Matière Condensée, Strasbourg; August 25th – 29th 2008
- **Nanomaterials for magnetism and spintronics** Size-dependent Surface States on Strained Cobalt Nanoislands on Cu(111); B. W. HEINRICH, M. V. RASTEI, L. LIMOT, P. A. IGNATIEV, V. S. STEPANYUK, P. BRUNO, AND J. P. BUCHER; First French-Korean Physics school on Nanomaterials for magnetism and spintronics, Strasbourg; February 18th – 22nd 2008

- **Bunsentagung 2006** XPS-Untersuchungen thermisch aktivierter Prozesse an ultradünnen Fe-Schichten auf SrTiO₃(100); B. HEINRICH, A. DEMUND, R. SZARGAN; 105. Bunsentagung, Erlangen; May 25th – 27th 2006